Wave-Group Propagation and Hydrodynamics in the Inner Surf and Swash Zones

Enrique M. Padilla de la Torre

Imperial College London

Civil and Environmental Engineering
Imperial College London

Thesis submitted for the degree of Doctor of Philosophy

A mis padres y a mis hermanos, porque habéis cargado con el dolor de la distancia.

A Mari Carmen, porque gracias a ti nunca me sentí solo.

A mi mentor, José M. Alsina, porque creíste en mí cuando nadie más lo hizo.

Declaration of originality

All the work presented in this thesis is that of the author. Any work or contributions made by others is referenced appropriately.

Copyright declaration

Acknowledgements

Mi gratitud para con mi supervisor, José M. Alsina, es inmensa. Me diste una oportunidad y creíste en mí cuando nadie más lo hizo. De ti he aprendido mucho, tanto técnica como personalmente, y para mí y para muchos en el laboratorio, eres una referencia de cómo ser un excelente profesional y una buena persona. Me has dedicado más tiempo del que tenías y has sabido guiarme excepcionalmente bien, sabiendo darme total libertad y estando siempre tan cerca como yo necesitara. Eres un excelente docente, un excelente profesional y el mejor supervisor que hubiera podido pedir.

To my officemates over the years, Demetris, Dani, Yannis, Marc, Alex and Liliane, thank you for all your support, advices and stimulating conversations. I must also thank the rest of the people in the lab for all the help, encouragement and memories you have given me. I am also indebted to Rebecca and Fionnuala for making the process as smooth as possible. Likewise, all my experimental tasks could not have been achieved without the assistance of Paul, Dave and Rob.

Finally, I am forever grateful to Imperial College London, in particular José M. Alsina and Chris Swan, because they gave me a life-changing opportunity.

Abstract

This thesis concerns a fundamental study of grouping waves propagating over a dissipative beach slope (1:100) and the dynamics of the associated long waves. This thesis represents an important contribution to the understanding of the group modulation influence on high and low frequency motions during shoreward propagation. Two new experimental sets of bichromatic wave-groups are presented, where an effective wave generation up to second order is successfully achieved.

The *IBIMS-ICL* data set explores the propagation of identical wave groups. The modulation is controlled by the group frequency, f_g, which affects the energy transfer to high and low frequency components. The growth of the high frequency (hf) wave skewness increases when f_g decreases. This is explained by nonlinear coupling between the primary frequencies, which results in a larger growth of hf components as f_g decreases, causing the hf waves to break earlier. The breaking locations are very well described by the wave-height to effective-depth ratio (γ). Due to the grouping structure, γ increases with f_g. Therefore, a modified Iribarren number is proposed leading to an improvement in reproducing the measured γ-values. Within the surf zone, the behaviour of the incident long wave also depends on the group modulation. For low f_g conditions, the lf wave decays only slightly by transferring energy back to the hf wave components. However, for high f_g wave conditions, strong dissipation of low frequency (lf) components occurs, which is explained in terms of lf wave breaking.

The *DIFFREP-ICL* data set investigates the generation and dynamics of longer waves than the wave-group structure induced by differences in the number of wave groups (Rp) within a repetition period. Consequently, an important energy content is measured at the repetition frequency f_r. The cross-shore amplitude evolution at f_r is partly explained by nonlinear energy transfers from the primary frequencies, and partly by a breakpoint forcing. When Rp increases, the energy transfer to f_r reduces. When $Rp \geq 3$, the amplitude of f_r suddenly grows at the breakpoint displaying a node-antinode pattern within the surf zone. The observed dominance of the breakpoint forcing over the energy transfers is justified by the combination of *steep-slope* regime and *steep-wave* conditions. A new methodology is proposed to identify the amplitude and phase cross-shore evolution of the radiated and reflected components. When energy dissipation of the higher lf components occurs, the swash is dominated by wave motions occurring at f_r.

Contents

List of figures

List of tables

List of key symbols and abbreviations

β	Normalized bed slope parameter
χ	Normalized surf zone width
Δx_b	Breakpoint excursion
η	Water surface elevation
γ	Spilling breaker
ξ	Surf similarity parameter or Iribarren Number
$\xi_{surfbeat}$	Surf beat similarity parameter
$f_1,\ f_2$	Primary frequencies with $f_1 > f_2$
$f_g,\ f_r$	Group frequency and repetition frequency
f_p	Mean frequency of the primary frequencies
Rp	Repetition
$Sk,\ As$	Horizontal and vertical wave asymmetry, respectively
$x,\ X$	Spatial domain: origin at the shoreline and wave paddle
$x_{ob},\ x_{mb},\ x_{ib}$	Outer, mean and inner breakpoint (x domain)
x_{ShWL}	Shallow water limit (x domain)
ATS, RTG, RTRW	Instruments: Acoustic-Type Sensor, Resistance-Type Gauge and Resistance-Type Run-up Wire
HF, LF	High frequency and low frequency
IFLW	Incident Free Long Wave
ILW	Incident Long Wave
OFLW	Outgoing Free Long Wave
RF	Reflected long wave

RI	Radiated Ingoing long wave
RO	Radiated Outgoing long wave
TO	Total Outgoing long wave

1 Introduction

1.1 Motivation of the research

The groupiness of high frequency (hf) waves, short gravity waves of period $\mathcal{O}(10\,s)$, and the presence of associated low frequency (lf) motions, $\mathcal{O}(100\,s)$, are characteristic features of random wave conditions propagating to the coastline. Lf waves (also called *long waves* because of their wavelength) may not be distinguished by an inexperienced observer unless a proper measurement of the water surface elevation is performed. In some conditions, such as high energetic storms or gentle beach slopes, the hf energy is almost completely dissipated by wave breaking of the short waves and the lf waves (when they are not breaking) may be discerned as the mass of water that drives the shoreline.

Long waves in nearshore areas are of fundamental importance due to their impact on the coastal morphology and their influence on the design and management of coastal structures. Since hf components eventually break during propagation to shallow water, the relative importance of long wave components increases and may be dominant in some surf/swash processes. For instance, the suspended sediment transport in the inner surf zone is mainly controlled by lf motions on dissipative beaches (Aagaard & Greenwood, 2008, Alsina et al., 2018, Bertin et al., 2018). On the other hand, harbours and large-vessel mooring systems may experience resonance in the infragravity band which means restrictions in their operations (Bowers, 1977). These are just a couple of examples where high and low frequency motions in shallow

water define complex patterns affecting human activities in the coast. Tackling the consequences of these interactions is where the research of the scientists becomes necessary and their knowledge, crucial. The research carried out within this thesis aims to extend the understanding of long wave motions in coastal areas.

1.2 Research context

First evidences about lf motions were reported by Munk (1949) outside the surf zone. To explain their origin, he proposed a mechanism, named *surf beat*, based on the variability of the balance of mass transport by the incident grouped waves into the surf zone. Using a cross-correlation of the hf envelope with the lf motions, Tucker (1950) highlighted a lag approximately equal to the time required for the swell to propagate into the surf zone and for the associated long wave to propagate to the shoreline and back as a reflected free long wave. Since then, the identification of remarkable levels of lf energy in field data obtained in the nearshore (inside and outside the surf and swash zone) has been widely reported in the literature (e.g, Elgar & Guza (1985), Elgar et al. (1992), Herbers et al. (1995), Ruessink (1998b), De Bakker et al. (2014), Moura & Baldock (2017), among many others).

These lf motions are widely assumed to be generated by grouped waves following two main mechanisms. One is due to the difference interactions between primary waves resulting in group-bound long waves in antiphase with the envelope of the wave groups (Biésel, 1952, Longuet-Higgins & Stewart, 1962). The second mechanism considers the generation of both shoreward and seaward propagating long waves by the oscillation of the breakpoint due to the wave-group structure (Symonds et al., 1982). That is, the moving breakpoint acts as a wave-maker radiating long waves at the wave group frequency seaward and shoreward. However, the effects of this moving-breakpoint mechanism seem negligible in certain dissipative conditions called *mild-slope* regimes (List, 1992, Janssen et al., 2003, Van Dongeren et al., 2007).

These mechanisms previously mentioned operate in real sea states where any degree of groupiness is always present. However, not much work has been done over dissipative conditions, with some exceptions, such as Ruessink et al. (1998a), Ruggiero et al. (2004) or De Bakker et al. (2013). In order to focus on the groupiness, some authors, such as Baldock et al. (2000) or Alsina et al. (2016), have used

representative bichromatic wave conditions to reproduce wave groupiness under controlled conditions. Bichromatic waves represent a wave modulation induced by two frequency components. They preserve the physical processes associated to random wave groups and simplify the number of nonlinear interactions among the frequency components. Therefore, the high-resolution experimental work with bichromatic waves propagating over a 1:100 beach slope proposed in this thesis represents a novel contribution to this research field.

This thesis aims to answer fundamental questions related to the influence of the group modulation on high and low frequency wave dynamics. Some of these fundamental questions are described below:

- How do the energy budgets associated to hf and lf evolve during the wave group propagation on a mild beach slope? Does the energy transfer from hf wave groups to lf motions influence the hf waves properties? If this is the case, does it explain the different evolution of the primary components (f_1 and f_2) during shoreward propagation that has been previously reported in the literature, for example, by Baldock et al. (2000) and Alsina et al. (2016)? What is the energy transfer pattern between hf and lf components after breaking on highly dissipative conditions when the hf forcing is reduced?

  In this context, higher order spectra is a promising approach to quantify the energy exchanges between triads of frequency components (De Bakker et al., 2015).

- Wave groups imply the existence of a local water depression or associated long wave. Those long waves propagating in the surf zone means a local water depth reduction. Is this depth reduction significant enough to induce early breaking? In that case, a limiting wave-height to water-depth ratio (γ-parameter) should be confirmed along the surf zone. Could the groupiness effect be then added to the existing empirical formulations to compute γ in order to improve the breaking description? Alsina et al. (2016) reported an earlier breaking of wave groups with larger group period but the physical mechanism was not explained.

- Based on previous works, no relevant radiation of free long waves is expected by the moving breakpoint on gentle beach slopes at the group frequency. However, preliminary results suggest the existence of long wave motions with longer

periods than the wave-group period and linked to the signal periodicity. For certain cases, these longer features become relevant at the shoreline and may dominate the run-up excursions. What is the generation mechanism of long waves of such long periods? Could the moving breakpoint be a relevant mechanism? If this is the case, does this mechanism become relevant for the lowest frequency components?

- Do long waves break close to the shoreline limiting the lf induced run-up as several authors have suggested (Van Dongeren et al., 2007, De Bakker et al., 2014)? What are the conditions for long wave breaking and how does it affect to coastal inundation?

1.3 Aims of the work and research strategy

The main objective of this thesis is to assess experimentally the influence of grouping waves and the associated long waves in the inner surf and swash zone hydrodynamics on dissipative conditions (typically mild slopes).

To reach this main goal, this work pursues to answer the following research questions:

i How can the limitations of a first-order wave generation be practically overcome in order to properly address the experimental study of propagating long waves?

ii What is the influence of the Group Modulation on the short wave breaking?

iii What is the influence of the Group Modulation on the long wave propagation?

iv What is the generation mechanism and dynamics of long waves longer than the wave group period?

The approach to answer these questions is to extend existing experimental works to mild beach profiles and small ratios of beach slope to long-wave angular frequency. These are highly dissipative conditions where hf energy is dissipated by depth-induced breaking and long wave energy is dominant close to the shoreline although long wave breaking might be expected. A mild-slope regime is observed at the wave group frequency, where the nonlinear energy transfers from the primary

waves to the subharmonic components becomes dominant, whereas the lf wave generation due to breakpoint forcing becomes negligible. However, this might not be the case for subharmonics of the group frequency as seen in preliminary experiments. Outcomes from this thesis means a novel perspective on nearshore hydrodynamics since not much work has been done over dissipative conditions.

This research is based on experimental results. Accordingly, the following tasks have been set:

- Implementation of an efficient experimental set-up that maximize the spatial resolution and minimize the length of the experiment.
- Development of a qualitative technique to identify spurious long waves at a certain frequency based on the analysis of its cross-shore amplitude undulating pattern. In this context, a correction of the first-order wave-generation is implemented in order to minimize the presence of spurious long waves.
- Adaptation and improvement of existing wave separation procedures.
- Implementation of a data preprocessing. Before any data analysis is carried out, the measured signals must satisfy some quality standards, which means format issues, noise suppression and measuring errors correction.
- Development of a wave-tracking methodology based on cross-correlation functions in order to accurately: (i) locate single breaking events tracking the short waves forming the wave groups, (ii) measure the celerity of both high and low frequency components during wave-group propagation and (iii) assess the merging of the remaining bores after short wave breaking.
- Computation of the nonlinear energy transfers due to triad wave-wave interactions using high order spectral techniques.
- Development of a new methodology to compute the breakpoint radiated long waves and the reflected long wave at the shoreline.

A highly dissipative profile (1:100 slope) has been built at the Wave Evolution Flume (Imperial College London), whose main characteristics and the deployed equipment are described in Chapter 3. The repeatability nature of the experiments

yields a dense mesh of measuring locations. The key feature of the measured data sets is the high spatial resolution, compared to previous experiments focused on grouping waves. Imposing this high resolution for the experimental data is a requirement for some of the data analysis techniques implemented in this thesis. On one hand, it promotes numerical stability, e.g, methods for wave separation that become especially unstable below a certain level of resolution. On the other hand, this quasi-continuous signal in the spatial domain allows having a high accuracy in the wave tracking of individual waves. Consequently, the description of different physical processes, e.g., the wave-group transformation during wave-group propagation, or the measure of some magnitudes, e.g., the short waves celerities during shoaling, are properly quantified.

1.4 Thesis layout

This thesis is divided into eight main chapters:

Chapter 2 aims to be an introductory chapter of general concepts and a critical discussion of long wave dynamic concepts relevant to the work presented in chapters 3 to 7. Chapter 2 starts with an introduction of wave groups as the first-order water surface elevation due to the linear superposition of two primary components. Then, this solution is expanded to second-order where the sum and difference terms arise due to nonlinear interactions of the primary components. Subsequently, a general view of the triad wave-wave interaction in terms of energy exchanges between components during the shoreward wave group propagation is provided. In this context, the differences between energy transfers to high and low frequency components are mentioned. The computation of these energy transfers is explained in terms of the phase coupling between the involved components in the triad. Therefore, some notions about bispectral analysis are introduced. Finally, the wave energy dissipation within the surf zone and the implications of a moving breakpoint on the radiation of long waves are discussed.

Chapter 3 provides a description of the experimental facilities, deployed instrumentation and measured data sets (*IBIMS-ICL* and *DIFFREP-ICL*). The description of these data sets includes the design of the wave conditions, measuring operations and overview of the wave cases composing each data set. Some post-processing

aspects to suppress noise and eliminate measuring errors are also included.

Chapter 4 briefly introduces the limitations of wave paddles operating with first-order wave generation theory to properly control the energy at generated high and low frequencies. As a result, a noticeable amount of energy in the way of unwanted free waves (known as spurious waves) is generated, being dramatically relevant at the lf components. In order to tackle this problem, a correction to the generation input is implemented to suppress the spurious energy at certain frequencies. Furthermore, a qualitative analysis is proposed in order to identify these unwanted waves before correction, and validation of the spurious suppression.

Chapter 5 describes the influence of the wave group modulation on high frequency (hf) wave components. The immediate consequence studied in this chapter is the influence of the wave group period on the depth-induced wave breaking of the individual short waves forming the groups. By tracking the individual wave crests, a proper description and identification of the individual breaking events within the wave-group structure is presented. Furthermore, a physical explanation of the substantial nonlinear transformations during wave group shoaling and eventual breaking is given by the analysis of the nonlinear energy transfers to hf wave components.

Chapter 6 describes the influence of the wave group modulation on the dynamics of low frequency (lf) wave components in mild beach slope conditions. To do so, different bichromatic wave conditions with the same energy content but different group frequency are analysed. At the group frequency, the lf amplitude growth and its relative phase with the wave-group structure during wave-group shoaling is studied. Moreover, the specific energy exchanges between the primary wave components and the main lf wave components are discussed using bispectral analysis. Finally, the lf energy dissipation in the inner surf zone is presented with special attention to wave conditions where full dissipation is observed and explained in terms of long wave breaking.

Chapter 7 concerns the long wave generation at the group frequency and subharmonics of the group frequency when different bichromatic wave-group structures are imposed. The cross-shore evolution of the energy at lf wave components is investigated, and the relative importance between nonlinear energy transfers from the primary frequencies and the breakpoint forcing is discussed for certain combinations of wave steepness and beach slope. When the breakpoint forcing is dominant, a new

methodology is proposed to identify the amplitude and phase cross-shore evolution of the radiated components from the breakpoint and reflected components from the shoreline.

Chapter 8 summarises the answers to those research questions posed in chapter 1 and provides suggestions for further work.

2
Background

2.1 Wave groups

Examination of the sea surface profile records indicates that wave heights are not uniform showing a tendency of forming wave groups, i.e., high waves often seem to be grouped together. In the most simplistic situation, wave grouping can be obtained by the linear superposition of two frequency components (i.e., bichromatic waves). When 2 wave trains propagate in the same direction with slightly different wave frequency ($f_1 \neq f_2$), the relative phase difference between those wave trains in space and time creates a sequence of constructive and destructive interferences. The linear superposition of η_{f_1} and η_{f_2} (Figure 2.1-*a*) gives rise to the resultant first-order wave field $\eta^{(I)}$ (Figure 2.1-*b*):

$$\eta^{(I)} = \eta_{f_1} + \eta_{f_2} = a_1 \cos(2\pi f_1 t - k_1 x) + a_2 \cos(2\pi f_2 t - k_2 x), \tag{2.1}$$

where the pair $[a_1, a_2]$ is the wave amplitude of both wave trains and $[k_1, k_2]$ are the wave-numbers associated to the primary frequencies $[f_1, f_2]$. As illustrated in Figure 2.1-*b*, the resultant wave field shows a succession of short waves, whose frequency f_p is the mean frequency of the primary frequencies ($f_p = (f_1 + f_2)/2$). Another effect of the phase difference is the modulation of the short waves as seen in Figure 2.1-*b*. This modulation, whose frequency is $f_g = |f_1 - f_2|$, develops a particular structure of the short waves commonly known as *wave group*.

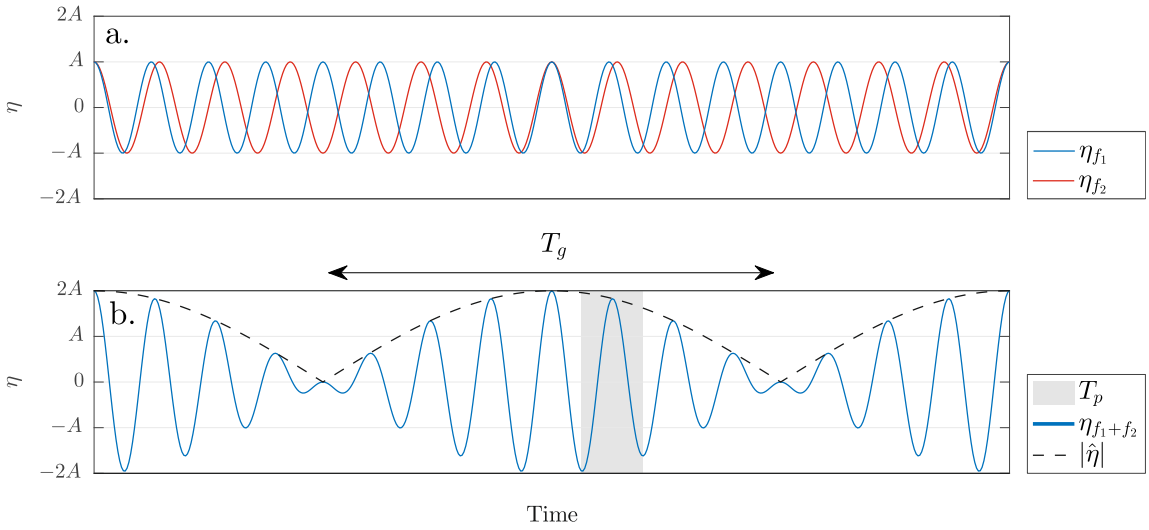

Figure 2.1: Linear sum of the wave trains η_{f_1} and η_{f_2} (a). The resulting wave field $\eta_{f_1+f_2}$ (b) is a modulated sequence of short waves whose frequency is f_p (mean frequency of the primary frequencies) and whose modulation oscillates with a frequency f_g (difference frequency of the primary frequencies). The wave field performed in plot b is commonly known as wave group.

Note that when $a_1 = a_2 = A$, the wave field $\eta^{(I)}$ from Equation (2.1) can be rewritten in terms of the mean primary waves (f_p) and its group modulation (f_g) as:

$$\eta^{(I)} = \underbrace{2A\,\cos(2\pi t \overbrace{\left[\frac{f_1 - f_2}{2}\right]}^{f_g/2} - x\left[\frac{k_1 - k_2}{2}\right])}_{\hat{\eta}}\,\cos(2\pi t \overbrace{\left[\frac{f_1 + f_2}{2}\right]}^{f_p} - x\left[\frac{k_1 + k_2}{2}\right]), \quad (2.2)$$

where $|\hat{\eta}|$ is the short wave envelope (See Figure 2.1-b). The transformation from Equation (2.1) to (2.2) is done using simple trigonometry and may be found in Svendsen (2006).

2.1.1 Phase velocity during shoreward propagation

The primary wave trains (η_{f_1} and η_{f_2}) propagate as free waves with a phase velocity that satisfies the Dispersion Equation:

$$\omega_j^2 = g\,k_j\,\tanh(k_j\,h), \quad (2.3)$$

where the subscript j indicates the wave component, ω is the angular frequency ($\omega_j = 2\pi f_j$), g is the gravitational acceleration and h is the water depth. Therefore,

the shoreward celerity of any free component is

$$c_j = \frac{\omega_j}{k_j} = \frac{g}{\omega} \tanh(k_j\, h). \tag{2.4}$$

From Equation 2.2, the short waves forming the groups (f_p-waves) propagates with the phase velocity

$$c_p = \frac{(\omega_1 + \omega_2)}{k_1 + k_2}. \tag{2.5}$$

In deep water, the Dispersion Equation is $\omega^2 = g\,k$. Therefore, Equation (2.5) in deep water may be rewritten as

$$c_p = \frac{g}{\frac{\omega_1+\omega_2}{2} - \frac{(\omega_1-\omega_2)^2}{2(\omega_1+\omega_2)}} \approx \frac{g}{\frac{\omega_1+\omega_2}{2}} = \frac{g}{\omega_p}, \tag{2.6}$$

where $\frac{(\omega_1-\omega_2)^2}{2(\omega_1+\omega_2)} \ll \frac{\omega_1+\omega_2}{2}$ and consequently, the linear theory phase velocity at f_p is a good approximation of the phase velocity of the short waves forming the groups (f_p-waves).

Likewise, the wave-group structure represented by the hf wave envelope ($|\hat{\eta}|$) propagates with the phase velocity

$$c_{gp} = \frac{\omega_1 - \omega_2}{k_1 - k_2}. \tag{2.7}$$

Note that, Equation (2.7) may be simplified in deep water as

$$c_{gp} = \frac{g}{\omega_1 + \omega_2} = \frac{1}{2}\frac{g}{\omega_p} = \frac{c_p}{2}. \tag{2.8}$$

In this case, Equation (2.8) is identical to the linear theory group velocity of the primary waves at the mean primary wave frequency (f_p) in deep water. Therefore, the velocity of the wave-group structure is widely accepted as

$$c_{gp} = \frac{c_p}{2}\left(1 + \frac{2\,k_p\,h}{\sinh(2\,k_p\,h)}\right), \tag{2.9}$$

where k_p is the wave-number associated to f_p, satisfying the Dispersion Equation.

In realistic sea states, the groupiness of ocean surface waves is a common physical process as a result of linear superposition of the dominant wave components of the Energy Spectrum. Janssen et al. (2003) showed, using the cross correlation functions

as described in Appendix B, that c_{gp} is still a good estimation of the phase velocity of wave groupiness in random sea states.

2.1.2 Second-order water surface elevation

Apart from the linear superposition of the primary wave trains, the bichromatic wave train (η_{f_1} and η_{f_2}) undergoes nonlinear wave-wave interactions that give rise to second-order wave components. Biésel (1952) and Longuet-Higgins & Stewart (1962), separately, evaluated these interactions using the perturbation approach outlined by Stokes (1847) and produced the second-order solution for the water surface elevation in intermediated water depth in the way:

$$\eta^{(II)} = \eta^{(I)} + \eta_{2f_1} + \eta_{2f_2} + \eta_{f_1+f_2} + \eta_{f_1-f_2} \tag{2.10}$$

where $\eta^{(I)}$ is the first-order solution that performs the wave-group shape (Equation (2.1)); η_{2f_1} and η_{2f_2} are self-interaction terms that define the second-order stokes solution; and $\eta_{f_1+f_2}$ and $\eta_{f_1-f_2}$ are the cross-interaction terms. Note that, $\eta_{f_1-f_2}$ is the only lf wave component, whose period matches the wave-group period, whereas η_{2f_1}, η_{2f_2} and $\eta_{f_1+f_2}$ are wave components belonging to the hf domain. The explicit expression for the second order water surface elevation is presented in Appendix A.

2.2 Long wave generation mechanisms

2.2.1 Long waves induced by variations of the radiation stress

The wave component $\eta_{f_1-f_2}$ formulated by Biésel (1952) and Longuet-Higgins & Stewart (1962) has traditionally concentrated major attention because it was the first lf wave generation mechanism proposed that explains the usual existence of lf wave components associated to shoreward propagating waves. Biésel (1952) solution describes a grouped wave train in a finite water depth in which $\eta_{f_1-f_2}$ results in a group-bound long wave in antiphase with the envelope of the primary waves. Subsequently, Longuet-Higgins & Stewart (1962) presented $\eta_{f_1-f_2}$ as a depression due to the difference interactions among pairs of a set of primary waves of closely neighbouring frequencies. Longuet-Higgins & Stewart (1962, 1964) found theoretically that wave groups propagating over a flat bed force a second-order long wave,

bounded to the incident group and in antiphase with the swell envelope as Biésel (1952) previously had found. The theoretical expression for the lf wave component $\eta_{f_1-f_2}$ (Equation A.7 in Appendix A), henceforth known as the group-bound Ingoing Long Wave (ILW), have been validated against experimental data (Kostense (1985), Baldock et al. (2000), Alsina et al. (2016), among others).

Physically, the higher waves within the wave group transport more momentum than small short waves. Consequently, the group-bound ILW is a water depression beneath the higher short waves that may be considered as the equilibrium response of the system to variations of the radiation stresses at the time and length scales of the short wave groups. In this context, (Longuet-Higgins & Stewart, 1962) reformulated the group-bound ILW in terms of the short wave energy as:

$$ILW(x,t) = -\frac{S_{xx}}{\rho\,(g\,h - c_g^2)} + const, \tag{2.11}$$

where S_{xx} is the wave radiation stress and ρ is the water density. At first sight, Equation 2.11 presents a singularity when $kh \ll 1$ (shallow water), where $c_g \approx \sqrt{gh}$. Physically, the ILW approaches resonance and its amplitude grows dramatically. However, Equation 2.11 may be approximated to second-order as

$$ILW(x,t) \cong -\frac{S_{xx}}{\rho\,g\,h\,(kh)^2} \cong -\frac{S_{xx}}{\rho\,\omega^2\,h^2} \tag{2.12}$$

with the constant of integration being at our disposal and using the higher-order expansion $c_g^2 = gh[1 - (kh)^2 + \mathcal{O}(kh)^4]$. Equation 2.12 is a nearly resonant steady state equilibrium solution in which the wave group envelope is perfectly in antiphase with the ILW so that the stress gradient and the ILW are in quadrature resulting in a zero cycle-averaged energy transfer. Longuet-Higgins & Stewart (1962) noted that the application of the near resonant solution of Equation 2.12 over a sloping bed is limited by the fact that the resonance needs time to build up. Consequently, Equation 2.12 is physically inconsistent in order to describe the ILW evolution over a sloping bottom, unless the bottom slope is sufficiently gentle, so that a dynamical equilibrium may be achieved. For this being the case and assuming conservation of the short-wave energy, $S_{xx} \sim h^{-1/2}$ when $kh \ll 1$ and, therefore the ILW amplitude evolves as $A^{ILW} \sim h^{-5/2}$.

2.2.2 Breakpoint generated long waves

The breaking of individual waves forming the group defines a very well known spatial distribution where the larger short waves break in deeper water and the smallest ones travel further into shallower water depths. This time-varying breakpoint implies variations of the radiation stress in the time and space domain, and therefore, a dynamic forcing acting at the surf zone. The breakpoint mechanism formulated by Symonds et al. (1982) explains the radiation of shoreward and seaward long waves at the wave group frequency as a consequence of variations in the radiation stresses induced by a moving breakpoint. This generation mechanism can be understood with the analogy of a wave-maker acting at the surf zone generating long waves at the frequency of the breakpoint oscillations (group frequency).

As a result of the long waves radiated from the moving breakpoint, a very interesting cross-shore pattern develops inside and outside the surf zone: Inside the surf zone, if the shoreward radiated long waves reflect at the shoreline, the two waves travelling in opposite directions create a quasi-standing wave pattern where the cross-shore lf amplitude performs an undulating pattern. Outside the surf zone, the reflected wave at the shoreline and the seaward radiated long wave from the breakpoint combine and the resulting lf amplitude depends on their relative phase ($\Delta\Phi$). When $\Delta\Phi = 0$ rad the total outgoing long wave is the largest, performing the maximum response of the system. Alternatively, When $\Delta\Phi = \pi$ rad the total outgoing long wave is the smallest, performing the minimal response of the system. Symonds et al. (1982) found that the normalized surf zone width

$$\chi = \frac{\omega^2 x_{mb}}{g\, S}, \tag{2.13}$$

where ω is the angular frequency of the brekpoint oscillation, x_{mb} is the mean breakpoint location measured from the shore and S is the beach slope, accounts reasonably well for $\Delta\Phi$ in relative steep slopes. Results from Baldock et al. (2000), Baldock & Huntley (2002), Moura & Baldock (2018) and Contardo et al. (2018), among others, widely support that maximum response is expected at $\chi \approx 1.2$, whereas minimal response at $\chi \approx 3.7$ (Symonds et al. (1982)). However, other studies, such as Kostense (1985) (experimentally), Schäffer (1993) (analytically) or Madsen et al. (1997) (numerically), support qualitatively but not quantitatively the results from

Symonds et al. (1982). Alternatively, Baldock et al. (2000) analysed experimentally the response intensity and the location of the node-antinodes compared to the mean breakpoint location. They concluded that a maximum response is likely to occur when the mean breakpoint location coincides approximatelly with a node, whereas the minimum response occurs when the mean breakpoint is close to an antinode.

Interestingly, the breakpoint generated long wave mechanism has been traditionally investigated at the group frequency, where the breaking forcing (oscillating at f_g according to the group modulation) is higher. However, considerably less attention has received the subharmonics of the group frequency, despite long waves at those lower frequencies may be potentially radiated based on the same physical process. Baldock et al. (2000) suggested that this possibility is not negligible by studying wave groups imposed to repeat periodically in time (Moura & Baldock, 2018).

2.3 Nonlinear energy exchanges during wave-group shoaling

During wave-group shoaling, wave-wave interactions may imply energy exchanges between the wave components when their interaction is resonant (or nearly resonant) (Phillips, 1960). In shallow water, the wave-wave interaction may be reduced to the interaction of 3 freely propagating components. In this case, the resonant condition requires for the triad of frequency components to satisfy:

$$f_1 + f_2 = f_3, \tag{2.14}$$

$$\vec{k_1} + \vec{k_2} = \vec{k_3}, \tag{2.15}$$

where the frequency (f) and wavenumber vector ($\vec{k}$) satisfies the Dispersion Equation for each wave component within the triad. Note that the resonant condition (Equations 2.14 and 2.15) cannot be fulfilled by any 3 wave components freely propagating in deep water (Holthuijsen, 2010). Actually, the resonant condition imposes the bound interaction between wave components to satisfy the Dispersion Equation, which only occurs where the waves are non-dispersive (shallow water). Consequently, resonant triad-wave interaction does not occur in deep water where energy transfer will require a quartet of wave modes (Phillips, 1960). However, in intermediate and

shallow water, propagating waves over reducing water depths progressively approach the resonant condition in nearly shallow water. In this case, near-resonance occurs and there is a rising energy exchange between the involved wave components.

2.3.1 Energy transfers to lf wave components

During wave group shoaling, the ILW grows and the phase difference between the wave-group structure and the ILW is no longer π rad. Numerous authors have observed the ILW to lag behind the wave-group structure in the field (Masselink, 1995), and this behaviour has also been reproduced numerically (List, 1992), observed in experimental data (Battjes et al., 2004, De Bakker et al., 2013) and explained theoretically (Janssen et al., 2003). The dynamical significance of this phase lag is that it implies the possibility of a net energy transfer to the ILW, as required for observed amplitude growth rates exceeding Green's law, where $A \sim h^{-1/4}$ (typical growth of free waves). Therefore, this phase lag is fundamental in the process of energy transfer from the primary waves to the ILW.

Battjes et al. (2004) found that the ILW evolution during wave-group shoaling is a function of the normalized bed slope parameter

$$\beta_b = \frac{S}{\omega}\sqrt{\frac{g}{h}}, \tag{2.16}$$

where S is the beach slope, ω is the angular frequency of the ILW and h is usually taken as the water depth at the mean breaking location. For low values of β_b (Battjes et al. (2004) suggest $\beta_b < 0.1$), a mild-slope regime exists in which the ILW amplitude growth during the wave-group shoaling is large and close to the shallow-water equilibrium solution $\sim h^{-5/2}$ (Longuet-Higgins & Stewart, 1962). Conversely, when $\beta_b > 0.45$, a steep-slope regime is defined and the ILW amplitude growth is weak due to a minimal energy transfer. In these conditions, the ILW amplitude grows almost according to Green's Law ($\sim h^{-1/4}$).

Aware of these limiting theoretical ILW amplitude growth rates ($h^{-1/4} < A^{ILW} < h^{-5/2}$), Van Dongeren et al. (2007) showed numerically and experimentally that a function of the local depth in the form: $A^{ILW} \sim h^{-\alpha}$ may be a good descriptor of the ILW amplitude growth. α-values were observed by Van Dongeren et al. (2007) to increase from nearly $\alpha = 0.25$ for $\beta_b > 1$ to nearly $\alpha = 2.5$ for β_b approaching

zero, in agreement with Battjes et al. (2004).

Although the group frequency f_g is the first subharmonic of the primary frequencies, further lf wave components may arise specially in gently sloping beaches where the ILW is relatively important (De Bakker et al., 2016). In these conditions, the ILW may interact with itself transferring energy to its superharmonic $2f_g$ and inducing changes in the long wave shape becoming more asymmetric (Van Dongeren et al., 2007). Alternatively, the ILW may also transfer energy to its subharmonics as introduced by Baldock et al. (2000) when the bichromatic wave groups were imposed to repeat periodically in time. For instance, a wave group repeated every two groups develops an energetic repetition frequency $f_r = f_g/2$.

Interestingly, this progressive energy transfer to lf wave components during wave group shoaling, mainly represented by the ILW growth, has important consequences in nearshore areas. For instance, numerical models (Deigaard et al., 1999) and field data (Aagaard & Greenwood, 2008) confirm that the high sediment concentration induced by the larger short waves of the groups tends to move seaward due to the phase lag of the ILW behind the group. In this context, Alsina et al. (2016) reported the position of the breaker bar to be influenced by the wave group frequency, where the distance between the breaker bar and the shoreline increases as wave group period increases. Furthermore, not just the nearshore morphology, but the behaviour of the ILW importantly affects the inland dunes under storm conditions (De Vries et al., 2008).

2.3.2 Relative importance of nonlinear energy transfers to lf wave components and the breakpoint forcing

The scenario where the nonlinear energy transfer to ILWs and breakpoint mechanisms are comparable defines a complicated cross-shore pattern that has been numerically studied by Schäffer & Jonsson (1991) and Schäffer (1993). In this context, Battjes et al. (2004) concluded that the breaking forcing is expected to be dominant when the ILW amplitude growth is weak, which typically occurs in steep slopes with $\beta_b > 0.45$. On the contrary, when $\beta_b < 0.1$, any long wave radiated due to a breaking forcing should be masked by the dominant ILW amplitude growth, which typically occurs in mild beach slopes. This has been widely confirmed by List (1992), Van Dongeren et al. (2003) or De Bakker et al. (2016), among others, and by Janssen et al. (2003)

and Van Dongeren et al. (2007) who could not identify a dominant breaking forcing in experiments performed over relatively mild slopes. Baldock & Huntley (2002), Baldock (2012) and Contardo & Symonds (2013) suggested that the breaking forcing may be enhanced during storm conditions, when the short wave steepness increases and consequently hf wave breaking occurs before shallow water conditions. In this context, Baldock (2012) proposed a surf beat similarity parameter

$$\xi_{surfbeat} = \beta_b \sqrt{\frac{H_{OS}}{L_{OS}}}, \tag{2.17}$$

where β_b is the normalized bed slope and H_{OS}/L_{OS} is the short waves steepness in deep water, in order to quantify the long wave generation due to radiation stress gradients (Longuet-Higgins & Stewart, 1962) or breakpoint forcing leading to long wave radiation (Symonds et al., 1982). Large $\xi_{surfbeat}$ values implies steep wave conditions (high H_{OS}/L_{OS}) propagating on a steep-slope regime (high β_b). In these conditions, the breakpoint generated surf beat is dominant in agreement with Contardo & Symonds (2013).

2.3.3 Energy transfers to hf wave components

Besides the ILW growth during wave-group shoaling, an homologous energy transfer from primary wave components to higher frequencies arises. Through triad wave-wave interactions, the dominant frequency components (those with the highest energy content, that are near the spectral peak) transfer energy to higher frequencies by the sum interactions. Assuming f_1 and f_2 being the primary energetic components, the nonlinear energy transfer typically occurs as $\{f_1, f_2\} \rightarrow f_1 + f_2$ and the self interactions as $\{f_1, f_1\} \rightarrow 2f_1$ and $\{f_2, f_2\} \rightarrow 2f_2$. As a result of these hf energy transfers, the wave field undergoes a transformation of the wave shape. These changes are easily observable in short waves, whose symmetrical sinusoidal wave-shape in deep water is progressively lost in reducing water depths, with the sharpening of the crest and the flattering of the troughs (Guza & Thornton, 1982, Elgar & Guza, 1985). Furthermore, the vertical asymmetry increases, which is translated into pitched-forward short waves that may eventually break.

The transformations undergone by the water surface elevation due to nonlinear energy transfers to hf wave components may be quantified in terms of lack of hori-

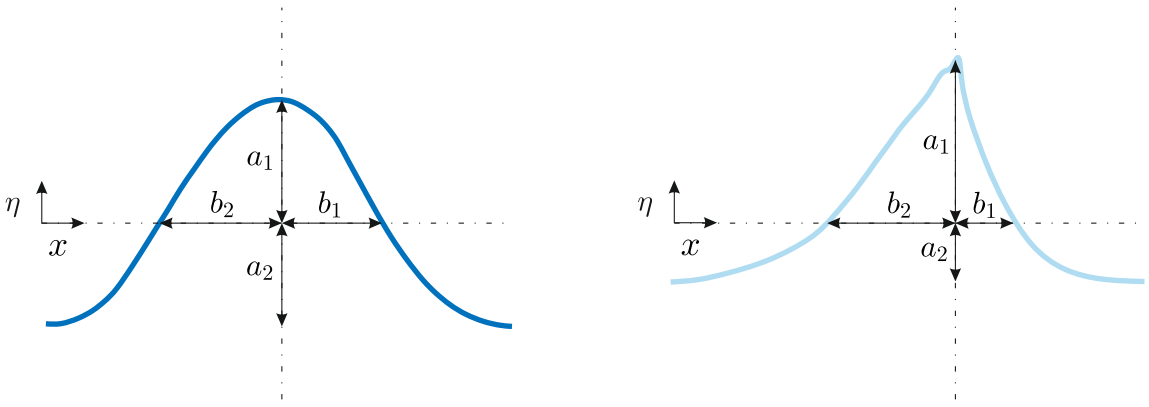

Figure 2.2: Sketch of a nonlinear transformation of a propagating wave from a nearly symmetrical wave shape (left), where $Sk \approx 0$ and $As \approx 0$, to a more skewed pitched forward wave (right), where $Sk > 0$ and $As < 0$. Adapted from Babanin (2011).

zontal and vertical symmetry, wave skewness (Sk) and asymmetry (As), respectively (see Figure 2.2). These geometric parameters can be defined locally for a single wave as:

$$Sk = \frac{a_1}{a_2} - 1, \tag{2.18}$$

$$As = \frac{b_1}{b_2} - 1, \tag{2.19}$$

where a_1 and a_2 are respectively the crest height and trough depth, whereas b_1 and b_2 are the horizontal distances from the breaker crests to the zero-upcrossing and -downcrossing, respectively. During wave propagation, Sk and AS are, therefore expected to grow in absolute value. When $Sk > 0$, the wave performs a crest height greater than the trough depth, whereas $As < 0$ corresponds to a pitched forward wave in the direction of propagation (see Figure 2.2).

Moreover, Sk and As can be also defined globally for a time series. In this case, the skewness and asymmetry can be estimated by bispectrum analysis (Elgar & Guza, 1985). Given a record of surface elevations η, the integral of the real and imaginary parts of the bispectrum B (explained below) defines the skewness and asymmetry respectively (Hasselmann et al., 1963, Elgar & Guza, 1985), i.e.,

$$Sk = \left[\int_{-\infty}^{+\infty}\int_{-\infty}^{+\infty} \Re\left\{B(f_i, f_j)\right\} df_i df_j\right] / E[\eta^2(t)]^{3/2}, \tag{2.20}$$

and

$$As = \left[\int_{-\infty}^{+\infty}\int_{-\infty}^{+\infty} \Im\left\{B(f_i, f_j)\right\} df_i df_j\right] / E[\eta^2(t)]^{3/2}, \tag{2.21}$$

where the normalizing factor $E[\eta^2(t)]^{3/2} = \sigma_\eta^3$.

Within the higher-order spectra, the bispectrum (B) decomposes the third-order moment of a signal and analyses the interaction between frequency components in a triad-type $[f_i, f_j, f_i + f_j]$, accounting for their phases coupling. The digital bispectrum, applied for discretely sampled data, is:

$$B(f_i, f_j) = E[A^*_{f_i}\, A^*_{f_j}\, A_{f_i+f_j}], \tag{2.22}$$

where A refers to the complex Fourier coefficients belonging to each frequency component. At first glance, Equation 2.22 returns zero unless the frequencies forming the triad $[f_i,\ f_j,\ f_i + f_j]$ are all energetic wave components with a high degree of frequency coherence (Kim & Powers, 1978). When this phase coherence occurs, a nonlinear wave-wave interaction is taking place.

Note that in the existing literature about higher-order spectra, there is another definition for Equation 2.22 (both commented in Collis et al. (1998)) depending on which of the coefficients the complex conjugation ($*$) is affecting to. The difference between the two definitions is a factor of -1.

2.3.4 Cross-shore energy balance

During wave propagation, the energy content associated to any frequency may either increase-decrease due to near resonant nonlinear energy exchanges among components. As a results, there is a net transfer of energy associated to a frequency f. In particular, the energy exchange due to nonlinear triad wave-wave interactions can be studied to the second order on the basis of high order spectral energy balance (Hasselmann et al., 1963, Elgar & Guza, 1985, Herbers et al., 2000, De Bakker et al., 2015, among others). In these studies, the transport of energy associated with a frequency f is presented as the following balance:

$$\frac{\partial F_f(x)}{\partial x} = S_{nl,f}(x) + S_{ds,f}(x). \tag{2.23}$$

where F_f is the cross-shore gradient of the energy flux spectrum, $S_{nl,f}$ is the nonlinear source term that accounts for the triad wave-wave interactions and $S_{ds,f}$ is a dissipation term that includes energy losses such as viscous dissipation.

The cross-shore integration of Equation (2.23) results in,

$$E_f(x) = \frac{1}{\rho\, g\, c_{g,f}(x)} \left(\rho\, g\, c_{g,f}(x_0) E_f(x_0) + \int_{x_0}^{x} (S_{nl,f}(x) + S_{ds,f}(x)) dx \right), \tag{2.24}$$

which assumes the linear approach that the spectral energy E travels with the wave group celerity c_g. Using the relationship between the spectral energy content and the wave height ($E = H^2/8$), the latter expression turns into:

$$H_f^2(x) = H_f^2(x_0) \frac{c_{g,f}(x_0)}{c_{g,f}(x)} + \left(\frac{8}{\rho\, g\, c_{g,f}(x)} \right) \int_{x_0}^{x} S_{nl,f}(x) dx + H_{ds,f}^2(x), \tag{2.25}$$

where the wave height grows due to shoaling (first term in the right-hand side) and nonlinear energy gains (second term). Conversely, $H_{ds,f}$ represents the height loss associated with the aforementioned sink term $S_{ds,f}$ where any dissipative processes may be included.

The nonlinear source term $S_{nl,f}$

The resonance condition, defined by Equations (2.14) and (2.15), accounts for the phase coupling between the wave components in the triad. Therefore, the amount of energy transfer between resonant components depends on their relative phases, which is quantified through bispectral analysis (Hasselmann et al., 1963, Collis et al., 1998). Herbers & Burton (1997), using the Boussinesq hypotheses, formulated a simple relation between the net nonlinear energy transfer ($S_{nl,f}$) to and from a frequency f and the bispectrum (B), which is

$$S_{nl,f} = 3\pi \frac{\rho\, g\, f}{h} \Im \left\{ \sum_{f'=0}^{f} B(f', f - f') - 2 \sum_{f'=0}^{f} B(f', f) \right\}, \tag{2.26}$$

where h is the water depth and $\Im$ indicates the imaginary part.

The nonlinear energy exchanges are computed using the bispectrum definition given by Equation (2.22) in order to be consistent with the signs criterium used by Herbers et al. (2000) and De Bakker et al. (2015), among others, to describe which

frequency components receive and transfer energy within the triad. Assuming a resonant triad $[f_1, f_2, f_1+f_2]$, if $\Im\{B(f_1, f_2)\} > 0$, f_1 and f_2 export energy to f_1+f_2. On the contrary, if $\Im\{B(f_1, f_2)\} < 0$, f_1 and f_2 receive energy from $f_1 + f_2$. When $\Im\{B(f_1, f_2)\} = 0$, the energy transfer vanishes.

Equation 2.26 is based on the Boussinesq approach, which yields reliable results during both shoaling and breaking short wave conditions (Herbers & Burton, 1997). The sum terms in Equation (2.26) includes all possible triad interactions that a certain frequency component f may experience. A graphical explanation of these sum terms is given by the symmetrical plane $f_i f_j$ in Figure 2.3. For instance, the yellow solid line performs the trajectory of all possible triad interactions involving f_2. Within this yellow line, the vertical and horizontal segments are associated to the term $\sum_{f'=0}^{f} B(f', f)$ in Equation 2.26, whereas the diagonal segment is associated to the term $\sum_{f'=0}^{f} B(f', f - f')$ (Equation 2.26). Consequently, the net energy exchange undergone by f_2, as defined by Equation (2.26), may be seen as proportional to the integration of the imaginary part of the bispectrum along the shaded area in Figure 2.3, turning over the sign for either $f_i = f_2$ or $f_j = f_2$ (the vertical and horizontal segments). Note that in Figure 2.3, at the point $[f_2, f_2]$, $\Im\{B(f_2, f_2)\} > 0$, which means that $2f_2$ gains energy from the self interaction of f_2 ($\{f_2, f_2\} \rightarrow 2f_2$).

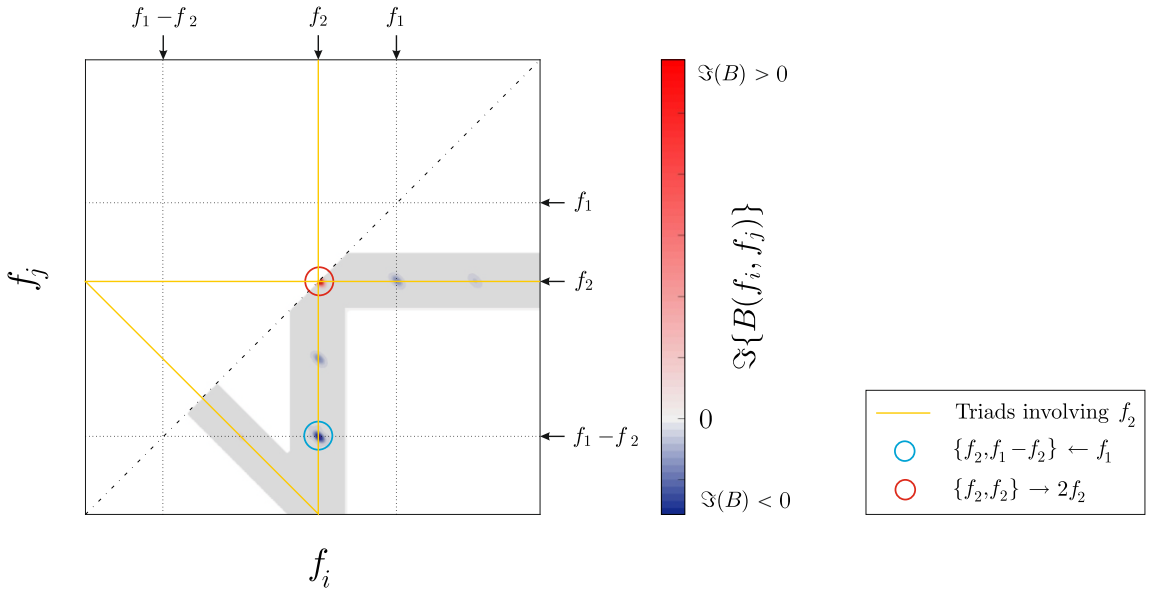

Figure 2.3: Sketch of the symmetrical plane $f_i f_j$, where the dashed line represents the trajectory of all possible triad interactions involving f_2. The red circle highlights the net transfer $\{f_2, f_2\} \rightarrow 2f_2$, whereas the blue circle highlights the net transfer $\{f_2, f_1 - f_2\} \leftarrow f_1$. Adapted from De Bakker et al. (2015).

Likewise, at the point $[f_2,\ f_1 - f_2]$, $\Im\{B(f_2, f_1 - f_2)\} < 0$, which means that the pair $[f_2,\ f_1 - f_2]$ gains energy from f_1 ($\{f_2, f_1 - f_2\} \leftarrow f_1$).

When computing the term $S_{nl,f}$, if any lf component is involved in the resonant triad, the reflection of the long wave at the shoreline may interfere in the relative phase of the triad, and therefore, in the correct computation of $S_{nl,f}$. However, Henderson et al. (2006) showed that the interference of reflected long wave is negligible and Equation 2.26 is still a good approximation.

The dissipation term $S_{ds,f}$

In general, the term $H^2_{ds,f}$ in Equation 2.25 is a closure term since the incident wave height H_f is a measured quantity and the nonlinear energy exchange $S_{nl,f}$ may be estimated using Equation 2.26. Jonsson (1967) formulated an estimation of the sink term $S_{ds,f}$ as the time-averaged rate of energy dissipation due to bed friction :

$$S_{ds,f} = \frac{2}{3\pi}\rho\, f_e\, (A\omega)^3, \tag{2.27}$$

where A and ω are the amplitude and angular frequency, respectively, and f_e is the energy dissipation factor set around 0.05 in glass-made wave flumes, where smooth laminar conditions ($Re < 3 \cdot 10^5$) applies.

2.4 Wave breaking

During wave propagation, the water surface elevation experiences substantial transformations due to the combination of nonlinear energy exchanges between frequency components or wave shoaling, among others. Because of these transformations, waves become unstable at some point and the wave breaking becomes the most efficient and significant sink of energy. Consequently, the wave height decreases importantly as confirmed by Liu & Babanin (2004) who reported local wave-height loses of more than 50%. Comparing scales, the wave energy slowly accumulated due to wind action (field data) during wave shoaling is suddenly released in a tiny fraction of the propagation length. Thus, the wave breaking is a highly nonlinear process where an intense exchange of momentum, heat and gases through the interface air-water locally occurs (Babanin, 2011).

A propagating wave that progressively becomes more skewed during shoaling may be described by stokes wave theory assuming an in-phase superposition of hf wave components. However, the point where the wave becomes unstable and break as a consequence of the skewness growth cannot be estimated using any wave theory, unless a certain empirical criterion, e.g., skewness limitation, is introduced. Actually, this reasoning highlights the usual approach to study wave breaking as in Dean & Dalrymple (2004) or Svendsen (2006). For the last decades, empirical evidences has configured our understanding of the wave breaking either classifying the kind of break pattern (Battjes, 1974), or defining empirical breaking criteria to describe the maximum possible wave height during the surf zone (Battjes & Janssen (1978), Svendsen (1984), Dally et al. (1985), among many others).

2.4.1 Short wave breaking on dissipative sloping beds

Empirically, Battjes (1974) observed that wave breaking characteristics are very well correlated to the surf similarity parameter (or Iribarren Number)

$$\xi = \frac{S}{\sqrt{H_0/L_0}}, \tag{2.28}$$

which is a ratio between the beach slope S and the square root of the deep water wave steepness $\sqrt{H_0/L_0}$.

When $\xi \leq 0.1$, a spilling break-type is assumed where crests spill down the wave face. In these conditions, the wave breaking is widely accepted to be induced by the water depth and, consequently, the ratio between the wave height and the water depth within the surf zone is constant (γ). Alternatively, if this spilling-type breaker is accepted, the wave breaking (wave heights and locations) may be estimated based on γ as a breaking parameter descriptor. Empirically, Bowen et al. (1968) showed a clear trend of γ as a function of ξ. Later on, this dependence was confirmed by Goda (1970), Weggel (1973) and Battjes (1974), among others, where the observed γ-parameter are in the range 0.7 to 1.2. In general, the γ growth with increasing ξ is a widely reported characteristic. Subsequent investigations have tried to provide general empirical formulations to compute γ. For instance, Battjes & Stive (1985)

proposed perhaps the most widely used expression

$$\gamma = 0.5 + 0.4 \tanh\left(33 \frac{H_0}{L_0}\right), \tag{2.29}$$

where γ-parameter is assumed to weakly depend on the beach slope, but on the deep water wave steepness only (H_0/L_0).

For the last decades, subsequent works tended to a refinement of this γ-parameter trying to include physical processes not initially considered or just improving the description under certain conditions. For instance, Ruessink et al. (2003) formulated a new functional form of γ, where a local dependence on the product of the local wave-number and water-depth ($k\,h$) was reported improving importantly the predictions based on Battjes & Stive (1985) formulation. However, to the best of the author's knowledge, no specific attention has received the influence of the group modulation on general formulations of the γ-parameter.

2.5 Lf motions close to the shoreline

Due to short wave breaking, the wave energy close to the shoreline may be dominated by lf wave motions, especially on dissipative beaches, where the hf wave energy is importantly reduced (Ruessink et al., 1998a). In this case, the mass of water is mainly driven by lf motions whose energy content may change within the inner surf due to energy dissipation (friction breaking) or nonlinear energy exchanges with higher frequency components. As a result, the remaining lf energy importantly affect the swash dynamics.

2.5.1 Reflection and dissipation of lf waves within the inner surf and swash zones

Close to the wave breaking location, when the short waves are in shallow water, bound lf waves can also be progressively "released" from the wave group structure since these non-dispersive conditions correspond to those where the forced long wave satisfies the free wave dispersion relationship (Elgar et al., 1992, Herbers et al., 1995, Baldock & Huntley, 2002, Baldock, 2012). Conversely, if the short waves are not shallow water waves at the breakpoint, the ILW may reduce in amplitude along with

the reduction in the primary wave forcing after breaking (Baldock & Huntley, 2002, Battjes et al., 2004, Lara et al., 2011, Baldock, 2012). A number of experimental and field data sets suggest that ILWs undergo strong nearshore dissipation after wave group breaking (Baldock et al., 2000, Battjes et al., 2004, Henderson et al., 2006, Baldock, 2012).

When ILWs reach the shoreline, their remaining energy is partly reflected and partly dissipated at the shoreline. The interaction between the incident and refleted wave creates a characteristic cross-shore pattern of node-antinodes, which is clearly seen in Baldock et al. (2000). Guza & Thornton (1985) were one of the first to observe a frequency dependence on the amount of energy reflected. Lower frequencies (longer waves) were observed to dissipate less energy at the shoreline developing an undulating pattern, whereas more dissipation is observed at higher frequencies (shorter waves) performing a progressive wave pattern. Subsequent field and experimental data, such as Elgar et al. (1994), Henderson et al. (2001), Battjes et al. (2004) and many others, have confirmed this frequency dependence. Battjes et al. (2004) defined a normalized bed slope parameter (similar to Equation 2.16):

$$\beta_H = \frac{S}{\omega}\sqrt{\frac{g}{H}}, \tag{2.30}$$

where H is the lf wave height, to determine the conditions where reflection prevails. Large reflection is expected under steep-slope regime ($\beta_H > 1$), whereas more dissipation occurs under a mild-slope regime ($\beta_H < 1$). The suitability for β_H to control the lf wave reflection has been experimentally validated by Van Dongeren et al. (2007), where lf wave reflection showed similarities with the reflection of short waves. In this case the scatter presented by Van Dongeren et al. (2007) was very well described by empirical relationship found by Battjes (1974) for short waves, $R = 0.2\pi\beta_H^2$ (traditionally $R = 0.1\xi^2$ in terms of the surf similarity parameter). Note that, a realistic computation of the lf wave reflection requires measurements at the shoreline, which are not always available as for Elgar et al. (1994) or De Bakker et al. (2014) where importantly higher reflection rates where measured.

Nearshore lf energy wave dissipation has been observed and partially explained by nonlinear interactions that transfer energy from the lf waves back to hf components, whereas frictional losses are seen to be secondary (Henderson et al., 2006, Thomson et al., 2006, Van Dongeren et al., 2007, De Bakker et al., 2014). Recently, a numerical

investigation (De Bakker et al., 2016) has shown that this situation is characteristic of steep sloping beach conditions where lf waves interact with the hf components transferring energy to hf components. Alternatively, an important dissipation of lf energy is attributed to long wave breaking (Battjes et al., 2004, Van Dongeren et al., 2007, De Bakker et al., 2014). Van Dongeren et al. (2007) reported that self-self interaction of the long waves result in the later enhancement and steepening of the lf wave front causing the lf wave front to become unstable and breaking.

After short wave breaking, the short waves reorganize their remain energy as bores propagating toward the shore. Differences in their celerities has been previously reported (Huntley & Bowen, 1975a,b, Sénéchal et al., 2001a,b) and eventually leads to a focusing or merge of the bores. This process is called *bore merging* and is typical from mild beach slopes, where the surf zone is large enough to allow the bore confluence. The differences in the celerity of the bores are typically explained in terms of amplitude dispersion (Sénéchal et al., 2001a, Brocchini & Baldock, 2008), where larger bores propagate faster than smaller bores and consequently, the former ones catch up with the latter ones. However, this explanation is recently assumed to be incomplete by Van Dongeren et al. (2007) and Tissier et al. (2015), who found that existing lf wave components may also induce differences in the propagation of individual bores due to the modulation of the water depth. In these conditions, the bore merging leads to an increase in the lf wave period within the surf zone (Sénéchal et al., 2001a), and a steepening of the long-wave front due to converging bores (Van Dongeren et al., 2007), which is linked to a potential energy transfer from the short waves (bores) to the lf wave components. Van Dongeren et al. (2007) reported that in certain circumstances, the steepening of the long-wave front may increase because of the bore focusing and induce an eventual ILW breaking.

2.5.2 Lf dominated swash dynamics

The time-varying shoreline defines the swash. In dissipative beach conditions, where hf waves become saturated and their energy is dissipated by wave breaking, the swash is governed by the reflections of the incident lf waves (Ruessink et al., 1998a, Sénéchal et al., 2011). In these cases, the swash performs long scale oscillations in good agreement with the remaining incident lf wave energy at the shoreline (Moura & Baldock, 2017). Likewise, the run-up or swash excursion also depends on the

remaining incident lf wave energy, among some other aspects, such as turbulent motions, bed friction or interactions between succesive swash events, that will not be discussed in this work. For instance, in a dissipative beach, a large lf energy dissipation during the inner surf zone, as the one observed by Van Dongeren et al. (2007), is likely to induce a shorter swash excursion than more energetic lf waves approaching the shoreline. Miche (1951) affirmed that wave energy dissipations within the surf zone justify a maximum run-up threshold regardless additional inputs of incident wave energy. In this context, a saturated surf zone dissipates any extra energy and no additional run-up occurs. This saturated scenario is typically seen on natural beaches at the swell frequencies, whereas the surf zone remains relatively unsaturated for lower frequencies (Guza & Thornton, 1982). However, relatively recent works (Ruessink et al., 1998a, Ruggiero et al., 2004, Stockdon et al., 2006, Sénéchal et al., 2011, Guedes et al., 2013) support that this statement is, in principle, extensible to lf waves, showing run-up energy saturation at lf domain during highly dissipative energetic storms. As a result, a roll off to lower frequencies of the run-up signal may be observed.

2.6 Summary

Dissipative coast lines might be dominated by lf motions as the hf waves becomes saturated and dissipate their energy by wave breaking. However the dynamics of lf motions have traditionally received less attention comparatively to steep-slope regimes. This represents a challenge, from a scientific point of view with interest in lf motions, since existing literature indicates that dissipative environments present more energetic lf motions with larger influence on the hydrodynamics and morphology. In this context, this thesis aims to contribute for a better understanding of long waves and their effects in mild sloping beds through the experimental study of shoreward propagating wave groups.

The bichromatic wave groups illustrate the simplest example of group modulation, whose effects over superharmonics and subharmonics of the primary waves during shoreward propagation are not completely understood. Assuming that transformations involving lf wave components are a priori independent from hf wave transformations, then the wave modulation should not be expected to have an impact in

the short wave breaking. However, this argument may not be fully correct according to reported evidences, such as the seaward migration of the breaking onset for longer wave groups. In this context, the nonlinear energy transfers to hf wave components should explain the influence of the group modulation over the short wave breaking. Likewise, the behaviour of the lf wave components during shoreward propagation should confirm a dominant energy transfer from the primary to lf components during wave-group shoaling, whereas the opposite transfer within the surf zone. Under certain circumstances, long wave breaking might potentially justify important lf dissipations in nearshore areas. If this is the case, a saturation of the run-up should be expected with predominance of frequency components lower than the group frequency.

Moreover, the potential measurement of an effective breakpoint generated long wave would represent the first evidence where the forcing mechanism becomes dominant over the incoming group-bound ILW in dissipative conditions.

3
Experimental work

3.1 Chapter overview

This chapter describes the experimental work carried out within this thesis. The chapter begins with a detailed description of the experimental facilities and instrumentation deployed. Then, the two sets of experimental data are presented, which are the basis of the analysis developed in chapters 5, 6 and 7. The obtained data sets are:

- *IBIMS-ICL*: The aim is to explore the propagation of identical wave groups and the influence of the wave group period on short-wave breaking and long-wave dynamics.
- *DIFFREP-ICL*: The aim is to investigate the generation of waves longer than the group structure due to periodic repetition of the wave group structure.

The description of these data sets includes the design of the wave conditions, measuring operations and overview of the wave cases composing the data set. Finally, some aspects of the time series post-processing are mentioned.

3.2 Experimental setup

The experiments presented in this study have been carried out in the Wave Evolution Flume at Imperial College London (See Figure 3.1). This wave flume has a length

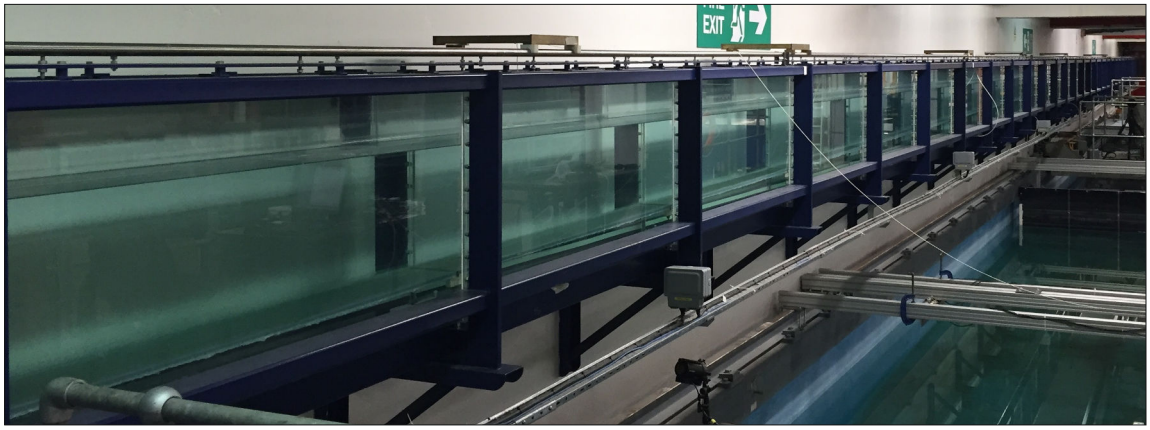

Figure 3.1: View of the Wave Evolution Flume from the deep end, in the vicinity of the wave generation.

of 60m, with a distance from the wave paddle to the emerged end of 52m. A beach profile has been built with glass panels forming a mild beach slope of 1:100. The flume width is 0.3m with a working water depth of 0.7m at the generation end, and of 0.5m at the toe of the beach profile (see Figure 3.2).

The waves are generated using a flap-type, bottom-hinged, wave paddle which is numerically controlled with active-force feedback. This guarantees the generation of the desired waves and the absorption of any unwanted reflected waves. Wave generation is performed using a first-order force control technique included in the commercial software that controls the wave paddle. Although the software does not allow for second order generation, the force control technique has been shown to effectively

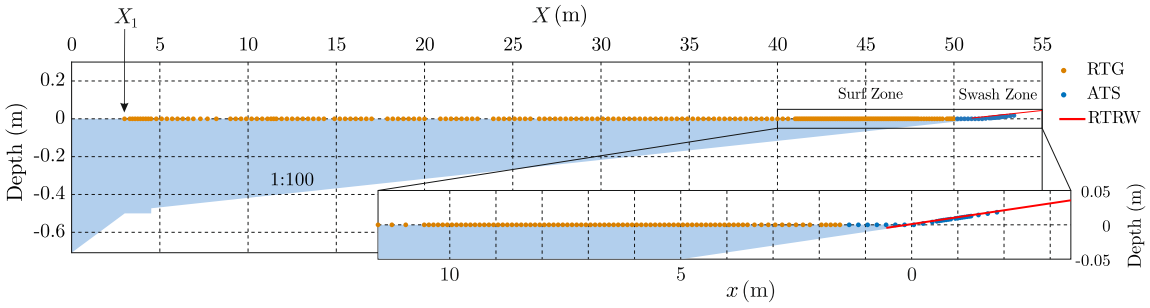

Figure 3.2: Schematic plot of the wave flume with the 1:100 beach profile, still water level and instrument locations. The detail plot focuses on the surf and swash zones. Yellow and blue dots indicate the location of the resistive-type gauges (RTG) and acoustic-type sensors (ATS), respectively, while the red line indicates the extension of the resistance-type run-up wire (RTRW). Note that the X-coordinate system has its origin at the wave paddle, whereas the x-coordinate system has its origin at the shoreline at the still water conditions. X_1 ($X = 3$m) denotes the first measuring position.

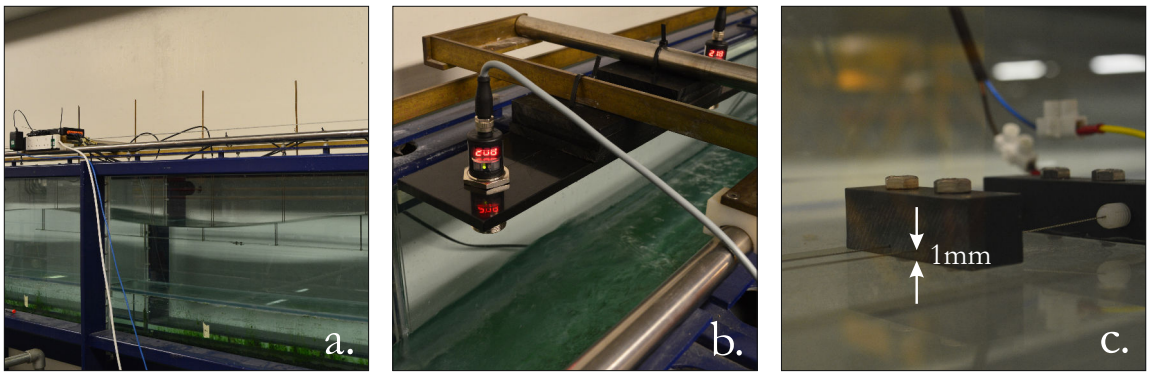

Figure 3.3: Instrumentation deployed on the Wave Evolution Flume: Resistance-type gauges (RTG) (*a*), acoustic-type sensor (ATS) (*b*), and emerged edge of the resistance-type run-up wire (RTRW) (*c*).

suppress high frequency spurious waves and an optimal active absorption of reflected waves (Spinneken et al. 2011). The presence of spurious long waves was identified in earlier experimental tests. Therefore, for this study, I have developed a methodology to correct the generation of wave groups by reducing the presence of spurious waves in the low frequency domain. The corrected generation methodology consists on the active suppression of spurious long waves using a generation-separation-correction scheme. The methodology consists on the following steps:

i An initial generation is performed based on a first-order input for the wave paddle signal.

ii The water surface elevation is measured along a dense array close to the wave paddle. Subsequently, the spurious Incident Free Long Wave (IFLW) is separated.

iii After back propagation of the IFLW to the wave paddle location, the wave paddle signal is corrected suppressing the presence of spurious long waves.

This methodology and the separation technique will be explained in detail in chapter 4 and provides in practice similar results to a theoretical second-order generation function.

Water surface elevation is measured using resistance-type gauges (RTG), acoustic-type sensors (ATS) and a resistance-type run-up wire (RTRW) (see Figure 3.3). The RTG and ATS have been deployed on movable platforms that, with repeated experiments, allow obtaining a surface elevation data set with a spatial resolution from 0.3m in the shoaling zone to 0.1m in the surf zone. The non-intrusive ATS

are deployed in the swash zone with an average separation of 0.2m, whereas the run-up wire, parallel to the beach profile, measures the swash horizontal location time series. In total, this high spatial resolution allows obtaining 234 cross-shore measuring locations along the 52m of wave flume (see Figure 3.2). Additionally, the breaking process is also recorded by video images.

3.3 *IBIMS-ICL* data set description

The aim of this data set is to explore the influence of the wave group modulation, i.e. wave group frequency, on the long wave dynamics over very gentle beach slopes and its influence on the properties of short wave groups. Therefore, series of bichromatic wave groups are generated with same energetic content but varying the wave group frequency. Their propagation over a 1:100 beach slope is analyzed.

This data set can be accessed on Zenodo at the following link used under Creative Commons Attribution licence: *https://doi.org/10.5281/zenodo.580327*.

3.3.1 Wave-conditions design

This data set comprises 12 bichromatic wave cases with the same wave energy content (see table 3.1). These are fully-modulated cases ($a_1/a_2 = 1$) with the same initial amplitude for the primary frequencies f_1 and f_2 ($a_1 = a_2 = 0.015$ m). The generated wave conditions are divided into three different series by modifying the mean primary frequency, $f_p = (f_1 + f_2)/2$ (Series A, $f_p = 1.1$ Hz; B, $f_p = 0.9$ Hz; and C, $f_p = 0.6$ Hz). Consequently, the second order sum-term component is imposed and remains constant for each series. Within each series, for any chosen value of f_p, the wave group frequency is varied by modifying the difference frequency ($f_g = \Delta f = f_1 - f_2$). Assuming that the group velocity (linear theory), c_{gp}, corresponding to the mean primary frequency, f_p, is a good approximation of the actual celerity of the wave groups (Janssen et al., 2003), then each wave series is characterized by a constant wave energy and energy flux but a varying wave group period.

The selection of these wave conditions, that is, the definition of the couple $[f_1, f_2]$ is made in such a way that all the groups are identical within a time series. It may be reduced to the condition $Rp = T_r/T_g = 1$, where T_r, being T_r the repetition period between two identical phases, matches the group period $T_g = 1/f_g$. Thus, the

TABLE 3.1: Generated bichromatic wave conditions for *IBIMS-ICL* data set

Case	f_p (Hz)	f_1 (Hz)	f_2 (Hz)	$\Delta f = f_g$ (Hz)	a_1 (m)	N	n	Rp
A-1	1.1	1.257	0.943	0.314	0.015	1	3	1
A-2	1.1	1.200	1.000	0.200	0.015	1	5	1
A-3	1.1	1.144	1.056	0.088	0.015	1	12	1
A-4	1.1	1.127	1.073	0.054	0.015	1	20	1
A-5	1.1	1.122	1.078	0.043	0.015	1	25	1
B-1	0.9	1.029	0.771	0.257	0.015	1	3	1
B-2	0.9	0.981	0.818	0.164	0.015	1	5	1
B-3	0.9	0.936	0.864	0.072	0.015	1	12	1
B-4	0.9	0.922	0.878	0.044	0.015	1	20	1
C-1	0.6	0.686	0.514	0.171	0.015	1	3	1
C-2	0.6	0.640	0.560	0.080	0.015	1	7	1
C-3	0.6	0.624	0.576	0.048	0.015	1	12	1

relationship between $[f_p, f_g]$ and n, the number of short waves forming a group, for $Rp = 1$, is

$$f_g = \frac{f_p}{n + 1/2}. \tag{3.1}$$

The minimum number of generated waves per group is 3, which yields the higher group frequencies from 0.314Hz for series *A*, to 0.171Hz for series *C*. Conversely, the group frequency decreases when the number of short-waves in each group increases. For the longest generated group (length around 30m), f_g decreases until 0.048Hz, representing 12 individual waves per group (case *C-3*). Using bichromatic experimental conditions, the separation between high and low frequency motions is straightforward. Every wave motion at around the primary frequencies (f_1 and f_2) and higher (frequency range in the present experiments of around 0.5 - 2Hz) belongs to the high frequency domain. Conversely, the wave motions at around the group frequency and below are considered as low frequency (frequency range of 0.04 - 0.4Hz).

The sampling frequency is 128Hz for RTG, decreasing to 100Hz for ATS. The designed experiments are characterized by 12-minute long data series. However, reasonably steady conditions were expected to develop along the flume only after the initial 200s.

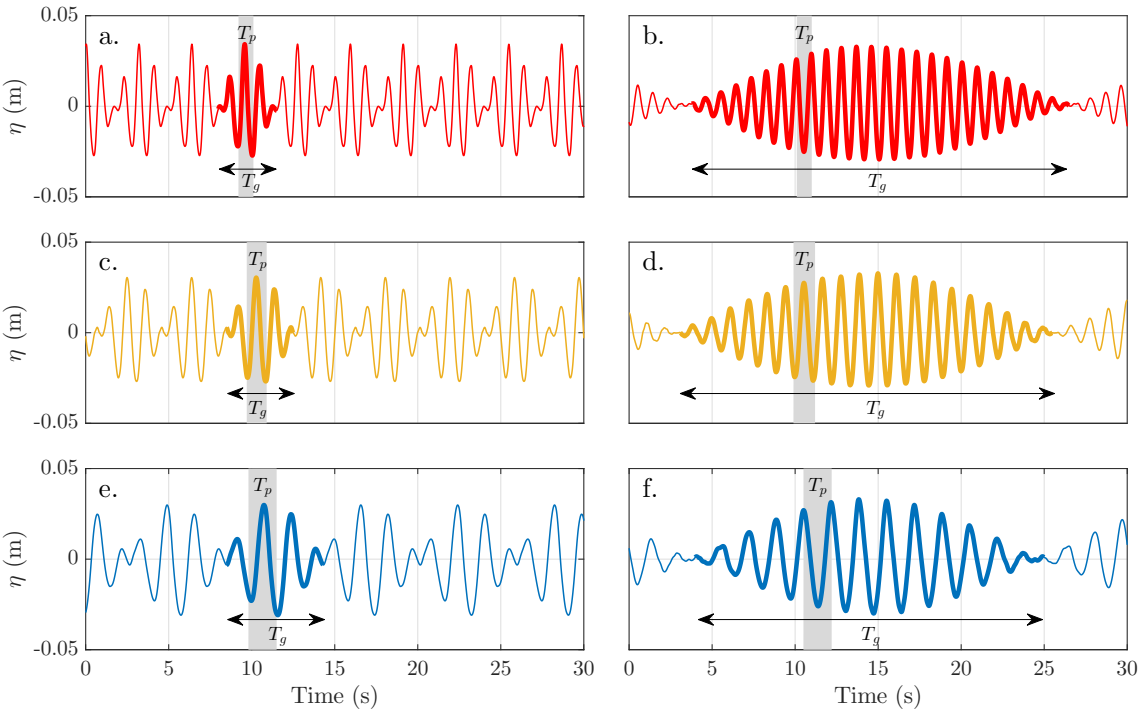

FIGURE 3.4: Water surface elevation η at X_1 for cases *A-1* (a), *A-4* (b), *B-1* (c), *B-4* (d), *C-1* (e) and *C-3* (f). The thicker line highlights an individual wave group within the time series when $T_r = T_g$ ($Rp = 1$). The wave group period is T_g and the mean period of the short individual waves is T_p (shaded area).

3.3.2 Description of generated wave groups

Figure 3.4 shows the water surface elevation of wave cases with the highest (left-side plots) and lowest (right-side plots) group frequencies for Series A (top plots), B (middle plots) and C (bottom plots). The fact that the wave groups are all identical within a time series is very clear in the left-side plots. For series A, plot a shows the case *A-1* where the groups consist of 3 crests, whereas plot b shows case *A-5* with 25 wave-crest forming the groups. Likewise, for series B, plot c shows the case *B-1* where the groups also consist of 3 crest, whereas in plot d, the case *B-4* displays 20 wave-crest forming the groups. As f_p decreases, the maximum number of crest n that satisfies a proper wave-generation ($f_g > 0.04$Hz) also decreases. That is the reason why for series C, plot f shows a wave group with 12 wave crests but slightly similar wave-group period T_g than plots b and d. Two different wave periods are clearly identified in *IBIMS-ICL* data set (see Figure 3.4): The mean primary wave period or time between two consecutive short wave crests forming the groups ($T_p = 1/f_p = 2/(f_1+f_2)$) and the period of the wave groups ($T_g = 1/f_g = 1/(f_1-f_2)$).

3.4 *DIFFREP-ICL* data set description

The aim of this dataset is to study the generation and propagation of long waves at frequencies lower than the wave group frequency and to evaluate their importance on the run-up on highly dissipative beach conditions (1:100 beach slope). For this reason, bichromatic wave groups are generated controlling the wave group repetition period. The long wave dynamics at the group and repetition frequencies are hence studied. This data set comprises a range of group frequencies (f_g), wave group repetitions (Rp), mean primary frequencies (f_p) and initial amplitudes of the primary components (a_1, a_2).

This data set can be accessed on Zenodo at the following link used under Creative Commons Attribution licence: *http://doi.org/10.5281/zenodo.1251992*.

3.4.1 Wave-conditions design

This data set comprises 10 bichromatic wave conditions, whose main characteristics are displayed in Table 3.2. These are fully modulated waves cases comprising a range of wave group frequencies ($f_g = f_1 - f_2$), wave group repetitions (Rp), mean primary frequencies ($f_p = (f_1 + f_2)/2$) and initial amplitudes of the primary components ($a_1 = a_2$), where the primary frequencies are f_1 and f_2. Within a times series of water surface elevation η, Rp is the number of wave groups before a given wave phase repeats exactly. When Rp is set to 1, that means that identical wave groups repeat exactly within a times series as seen in section 3.3 with *IBIMS-ICL* data set. In the present experiments, Rp is varied from 1 to 5 indicating that a given wave phase repeats exactly every 1 to 5 wave groups. The different wave group repetition Rp has been combined with varying f_g, f_p and amplitude (a_1, a_2), inducing variations in the location, width and length of the breakpoint location.

The range of f_p varies from 0.3Hz to 0.9Hz. f_p has an influence on the main breakpoint location by affecting the steepness of the primary waves and group velocity. Therefore, for a given primary waves amplitude, the main breaking onset moves shoreward for increasing values of f_p. The primary waves amplitude, a_1 and a_2, varies from 0.010m to 0.025m causing a seaward migration of the location of breaking onset for increasing amplitudes. The group frequency f_g varies from 0.074Hz to 0.284Hz and controls the width of the moving breakpoint. For a certain Rp and f_p, f_g is

Table 3.2: Generated bichromatic wave conditions for *DIFFREP-ICL* data set.

Case	f_p (Hz)	f_1 (Hz)	f_2 (Hz)	$\Delta f = f_g$ (Hz)	f_r (Hz)	a_1 (m)	n	Rp
MR-01	0.6	0.686	0.514	0.171	0.171	0.015	3	1
MR-02	0.6	0.700	0.500	0.200	0.100	0.015	3	2
MR-03	0.6	0.695	0.505	0.189	0.063	0.015	3	3
MR-04	0.6	0.695	0.505	0.189	0.063	0.025	3	3
MR-05	0.6	0.658	0.542	0.116	0.039	0.015	5	3
MR-06	0.6	0.697	0.503	0.194	0.039	0.015	3	5
MR-07	0.5	0.579	0.421	0.158	0.053	0.015	3	3
MR-08	0.3	0.347	0.253	0.095	0.032	0.010	3	3
MR-09	0.9	1.042	0.758	0.284	0.095	0.015	3	3
MR-10	0.6	0.637	0.563	0.074	0.025	0.015	8	3

computed as:

$$f_g = \frac{f_p}{n + \Delta n}, \tag{3.2}$$

where $(n + \Delta n)$ is the number of wave crests forming the groups: n is the integer number of crests, whereas Δn is a necessary increment to satisfy the repetition condition imposed by Rp. Therefore, Δn is a Rp-dependent parameter numerically computed by varying Δn in increments of $5 \cdot 10^{-5}$ until the mean absolute difference of η between repetition periods T_r is minimized. As a result, Δn = [0.5, 0, 0.16665, 0.1] for Rp = [1, 2, 3, 5].

The sampling frequency is 128 Hz for RTG, decreasing to 100 Hz for ATS. The designed experiments are characterized by 12-minute long data series. However, reasonably steady conditions were expected to develop along the flume only after the initial 200s.

3.4.2 Description of generated wave groups

Figure 3.5 shows the water surface elevation of wave cases with different repetition number Rp. For case *MR-01* (plot *a*), $Rp = 1$ and a given wave phase repeats exactly every 1 wave group, that is, all the wave groups are identical within a time series. In contrast, the signal repeats after 2 wave groups for case *MR-02* (plot *b*), whereas for cases *MR-03* (plot *c*) and *MR-06* (plot *d*), the signal repeats every 3 and 5 wave groups, respectively. Three different wave periods are clearly identified in *DIFFREP-ICL* data set (see Figure 3.5): The mean primary wave period or time between two consecutive short wave crests forming the groups (T_p), the period of the

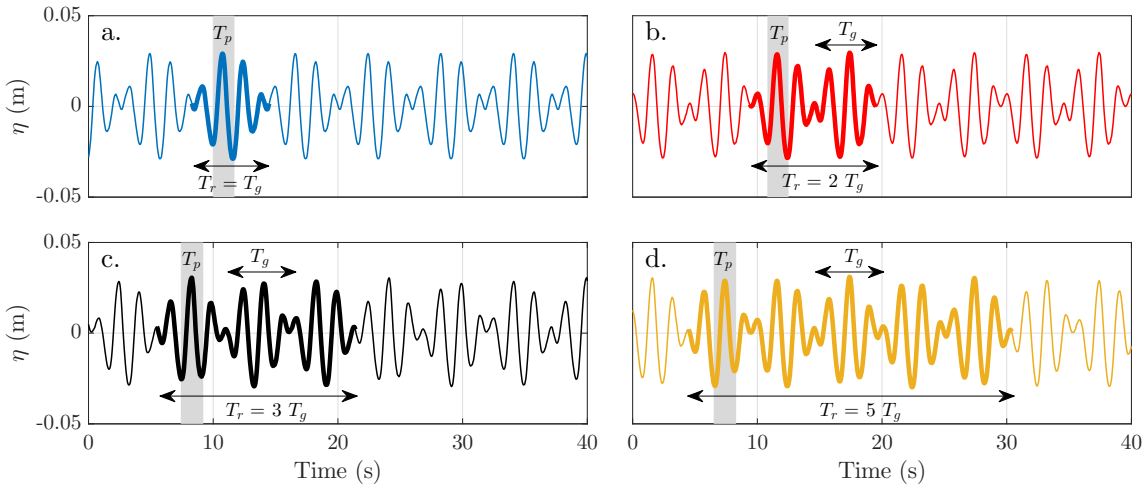

FIGURE 3.5: Water surface elevation η at X_1 for cases with different number of wave groups per repetition time: $T_r = T_g$ for *MR-01* (a), $T_r = 2\,T_g$ for *MR-02* (b), $T_r = 3\,T_g$ for *MR-03* (c) and $T_r = 5\,T_g$ for *MR-06* (d). The thicker line highlights the sequence of *Rp* wave groups within a repetition period T_r. The wave group period is T_g and the mean period of the short individual waves is T_p (shaded area).

wave groups (T_g) and the repetition period (T_r).

3.5 Post-processing

The measured water surface elevation signals at different cross-shore locations are ensemble averaged. Figure 3.6-a shows, for a location in the vicinities of the wave generation (X_1), the ensemble measured signals (η^*) along T_r and the corresponding averaged signal ($\widetilde{\eta}$). The matching degree between η^* and $\widetilde{\eta}$ at this location is excellent. However, this matching degree reduces while wave-groups propagate shoreward (this variability is illustrated in Figure 3.6-c). Figure 3.6-b shows η^* and $\widetilde{\eta}$ for a location within the surf zone. The differences between the ensemble signals η^* are slightly higher than in plot a, but the averaged signal $\widetilde{\eta}$ still performs a very good match. Note that the ATS were not able to properly measure the wave crests. This issue will be addressed below.

In order to quantify the validity of the averaged signal $\widetilde{\eta}$, its mean absolute error ($\overline{E_{abs}}$) is computed as the mean value of the standard deviation of the ensemble signals η^* at every instant. Likewise, its relative error (E_{rel}) is computed with respect to the H_{m_0} as:

$$E_{rel} = \frac{\overline{E_{abs}}}{H_{m_0}} \cdot 100, \tag{3.3}$$

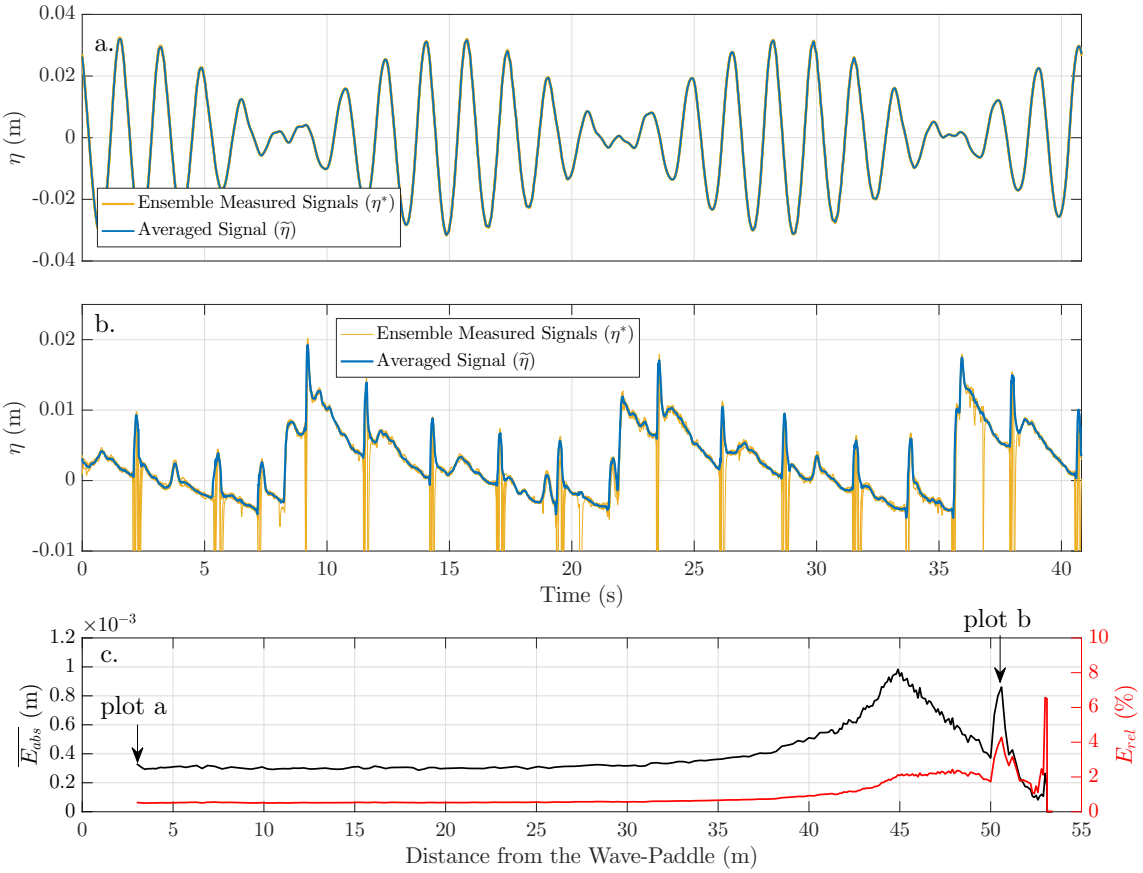

Figure 3.6: Ensemble measured (η^*) and averaged ($\widetilde{\eta}$) water elevation time series for case *MR-10* at the vicinities of the wave-generation (plot a) and within the surf zone (plot b). The cross-shore mean absolute (black) and relative (red) errors of $\widetilde{\eta}$ are shown in plot c, where the locations of plot a and b are highlighted.

where $H_{m_0} = 4\sigma_\eta$. Figure 3.6-*c* illustrates the cross-shore mean absolute and relative errors for case *MR-10* belonging to *DIFFREP-ICL* data set. As mentioned before, the absolute error in the vicinities of the generation (plot *a*) is very low, $\overline{E_{abs}} = \mathcal{O}(10^{-4}$ m), and similar to the RTG accuracy ($\pm 5 \cdot 10^{-4}$ m). Overall, the relative error remains below 1% during the shoaling region and progressively grows above 2% within the surf zone, which is an acceptable level of error. Locally, both the relative and absolute errors grow for the locations with ATS (plot *b*). ATS are functional when the wave steepness remains below a certain level. However this is not always the case in plot *b* and some of the ensemble signals η^* are unable to correctly perform the short wave-crests. When this situation happens, the averaged signal $\widetilde{\eta}$ at the target crest is only built using valid ensemble signals η^* at that crest. If a particular wave phase is not properly measured by any η^*, then this particular phase is rebuilt

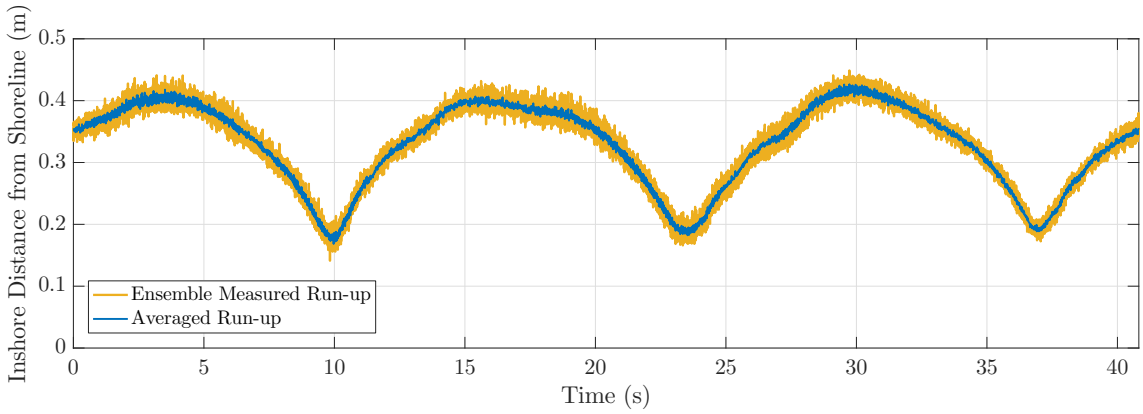

Figure 3.7: Ensemble measured and averaged run-up time series for case *MR-10*.

using parabolic interpolation and manual check.

Finally, for the present analysis new water surface elevation signals (henceforth η) are built repeating $\widetilde{\eta}$ a minimum of 30 times. Using averaged signals instead of the measured time series allows the reduction of noise and undesired errors in the time series. Furthermore, η series built on repeated $\widetilde{\eta}$, might be as long as needed to satisfy any resolution in the frequency domain.

Likewise, the same technique is carried out for the run-up signals (Figure 3.7). For the wave case *MR-10*, the absolute and relative errors are $9 \cdot 10^{-3}$ m and 3.3 %, respectively. In general, $\overline{E_{abs}} = \mathcal{O}(10^{-2}$ m) for run-up signals, whereas the relative error increases for cases where the run-up excursion decreases.

3.6 Concluding remarks

Two laboratory data sets, *IBIMS-ICL* and *DIFFREP-ICL*, have been presented. They comprise a variety of experimental wave conditions performing fully modulated bichromatic wave-groups propagating on a 1:100 sloping bed. The characteristics of these wave conditions, experimental conditions design and aims of the experiments are properly addressed for both data sets. The experimental facilities and measuring technique with a high spatial resolution have been fully described. On top of that, the measured signal has been post-processed using an ensemble-average technique which reduces importantly the noise and undesired errors.

4

Generation and separation of low frequency waves

4.1 Chapter overview

The study of wave groups and associated long waves using laboratory wave conditions requires an accurate wave generation with proper control of the generated energy at high and low frequencies. Limitations in the wave generation technique, i.e., first-order wave generation, may give rise to extra energy in the lf domain by means of undesired propagating waves.

This chapter introduces the wave generation technique adopted in the present work to overcome existing limitations of first-order wave generation systems. A first-order wave generation produces unwanted free waves, known as spurious waves, propagating shoreward and in linear superposition with existing wave trains. The superposition of spurious waves with the target waves performs a characteristic cross-shore pattern formed of an undulating cross-shore amplitude similar to quasi-nodes and -antinodes due to the phase relationship between wave components propagating with different celerities. Using linear wave theory, a theoretical estimation of the location of these nodes and antinodes is obtained. In order to identify these spurious waves and confirm their existence, a methodology is proposed based on the analysis of existing different cross-shore undulating patterns. Once the existence of the spurious wave is confirmed, a proper low frequency wave generation procedure is proposed

using existing wave separation techniques. Finally, this chapter describes the accurate wave generation of the wave cases forming the *IBIMS-ILC* and *DIFFREP-ILC* data sets by means of the proposed lf correction procedure.

4.2 Generation of lf waves at the wave maker

In the context of bichromatic waves being generated in a wave flume, the first-order water surface elevation is given by

$$\eta^{(I)} = A_{0,1}\,\cos(2\pi f_1 t - k_1 x + \phi_{0,1}) + A_{0,2}\,\cos(2\pi f_2 t - k_2 x + \phi_{0,2}) \qquad (4.1)$$

where the pairs $[A_{0,1},\, A_{0,2}]$ and $[\phi_{0,1},\, \phi_{0,2}]$ are the initial wave amplitudes and phases for the primary frequencies f_1 and f_2. The nonlinear interactions between f_1 and f_2 results in the raise of new frequency components (bound waves), that to the second order are: $2f_1$ and $2f_2$ due to self-interactions, whereas $f_1 - f_2$ and $f_1 + f_2$ due to the cross-interactions.

In the context of wave-maker theory, the primary waves (f_1 and f_2) and the interaction bound wave components ($2f_1$, $2f_2$, f_1+f_2 and f_1-f_2) satisfy the second-order free surface boundary condition, but they do not fully satisfy the second-order boundary condition at the wave-maker. As a consequence, each interaction also gives rise to a free wave component, which is commonly known as a spurious wave because of its unwanted nature (Hansen et al., 1980). This free wave contamination is an important limitation of existing wave theories to correctly reproduce the target wave case. Furthermore, outgoing waves (radiated and reflected) coming from the surf zone may re-reflect at the wave paddle giving rise to extra free waves. The existence of these re-reflected waves is minimized when active wave absorption is applied (Baldock et al. (2000), Spinneken (2010), among others) which is commonplace in most wave generation facilities. The accuracy of the absorption depends on the target frequency, but usual performances yield up to 90% of effective absorption for wave frequencies above 0.4Hz, reducing to 60% around 0.1Hz (Baldock et al., 2000).

Much work has been done during the last decades in order to improve the wave generation systems above first-order. Schäffer (1996) formulated the wavemaker generation theory to second-order. Later on, Spinneken (2010) and Aknin (2015) formulated second-order force-feedback controlled wave-maker theory, where a com-

pensation signal is generated to cancel the spurious wave. However, second-order wave theory is not implemented in the generation software of the existing wave paddle at Imperial College London. Instead, the Wave Evolution Flume has first-order generation implemented based on force-feedback control, where excellent absorption with a very small presence of spurious waves at high frequency has been reported (Spinneken, 2010, Spinneken et al., 2011). However, the energy content of unwanted free ingoing waves in the lf domain is still important and a second-order correction is required.

As a consequence of the limitations of the wave generation in the wave flume, the lf wave amplitude at the group frequency f_g may be decomposed in the following components:

$$ILW(X,t) = A_0^{ILW}\left(\frac{h_0}{h_X}\right)^{\alpha}\cos(2\pi f_g t - |\widetilde{k_X^B}|\,X + \phi_0^{ILW}), \tag{4.2}$$

$$IFLW(X,t) = A_0^{IFLW}\left(\frac{c_{g,0}}{c_{g,X}}\right)^{1/2}\cos(2\pi f_g t - |\widetilde{k_X^F}|\,X + \phi_0^{IFLW}), \tag{4.3}$$

$$OFLW(X,t) = A_0^{OFLW}\left(\frac{c_{g,0}}{c_{g,X}}\right)^{1/2}\cos(2\pi f_g t + |\widetilde{k_X^F}|\,X + \phi_0^{OFLW}), \tag{4.4}$$

where ILW is the Ingoing Long Wave (group-bound under non-resonant conditions), IFLW is the Ingoing Free Long Wave (unwanted) and OFLW is the Outgoing Free Long wave, which is the combination of reflected waves at the shoreline and radiated from the breaking location.

From Equations (4.2) to (4.4), $[A_0^{ILW}, A_0^{IFLW}, A_0^{OFLW}]$ and $[\phi_0^{ILW}, \phi_0^{IFLW}, \phi_0^{OFLW}]$ are the initial amplitudes and phases of the ILW, IFLW and OFLW, respectively; X is the distance from the wave paddle and t is the time domain. The average wavenumber accounting for the time required for a wave train to travel a distance X from the wave paddle ($X = 0$) is

$$\widetilde{k_X^j} = \frac{2\pi f_g}{X}\int_0^X \frac{1}{c^j}\,dX, \tag{4.5}$$

where the superscript accounts for the free (F) or bound (B) nature of the wave. For free waves at f_g, $\widetilde{k^F}$ is computed using the celerity $c^F = c_g$ based on the Dispersion Equation at f_g. In contrast, the ILW at f_g is a group-bound wave and, therefore, $\widetilde{k^B}$ is computed using $c^B = c_{gp}$ (Equation (2.9)) as a good descriptor of the wave group

velocity (Janssen et al., 2003).

The cross-shore variation in amplitude of the free waves accounts for the cross-shore energy flux conservation. Therefore, IFLW and OFLW evolve following linear shoaling with the coefficient $(c_{g,0}/c_{g,X})^{1/2}$. Conversely, the ILW amplitude growth during wave group shoaling follows a function of the local water depth (h) raised to a power α (Van Dongeren et al., 2007). The value of α will be discussed later on.

4.3 Qualitative analysis of cross-shore undulating patterns

The superposition of different wave trains has direct observable effects on the resultant surface elevation. When two wave crests meet at the same time-space, they are in phase and the resulting crest is the linear sum of the individual ones. In this case, their interference is constructive (see Figure 4.1, left plot). Conversely, when a wave crest and a wave trough meet at the same space-time, the two features are in antiphase and they cancel out (if their amplitudes are the same). In this case, their interference is destructive (see Figure 4.1, right plot). Therefore, the sequence of constructive and destructive interferences is a common process between propagating wave trains with different celerity or direction.

4.3.1 Cross-shore undulations

When 2 wave trains with the same frequency propagates with different celerities ($c_1 \neq c_2$), the cross-shore distribution of their relative phases is stationary, that is, the relative phase between the wave trains is different in every cross-shore location but constant in time. In particular, the linear superposition of two wave trains with same wave amplitude (i.e. $A_1 = A_2 = A$) and propagating in opposite direction with the same celerity (i.e $c_1 = -|c_2|$) give rise the very well known *standing wave* pattern (Figure 4.2a). At locations where the wave trains are in phase (constructive interference), the vertical motion of a water particle is maximum ($A_1 + A_2 = 2A$). Conversely, at locations where the wave trains are in antiphase (destructive interference), the vertical motion is null ($A_1 - A_2 = 0$). Therefore, the envelope performs an undulation (see Figure 4.2a) where the locations with maximum and null ver-

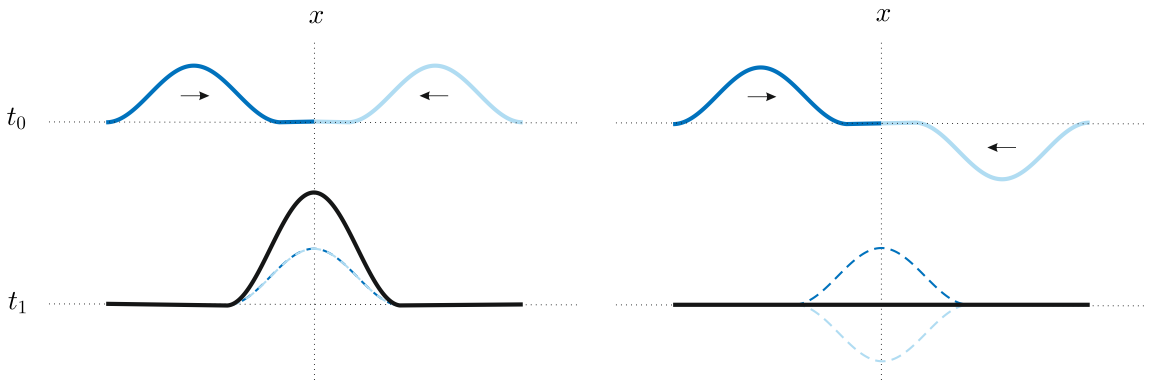

Figure 4.1: Sketch of constructive (left) and destructive (right) wave interferences.

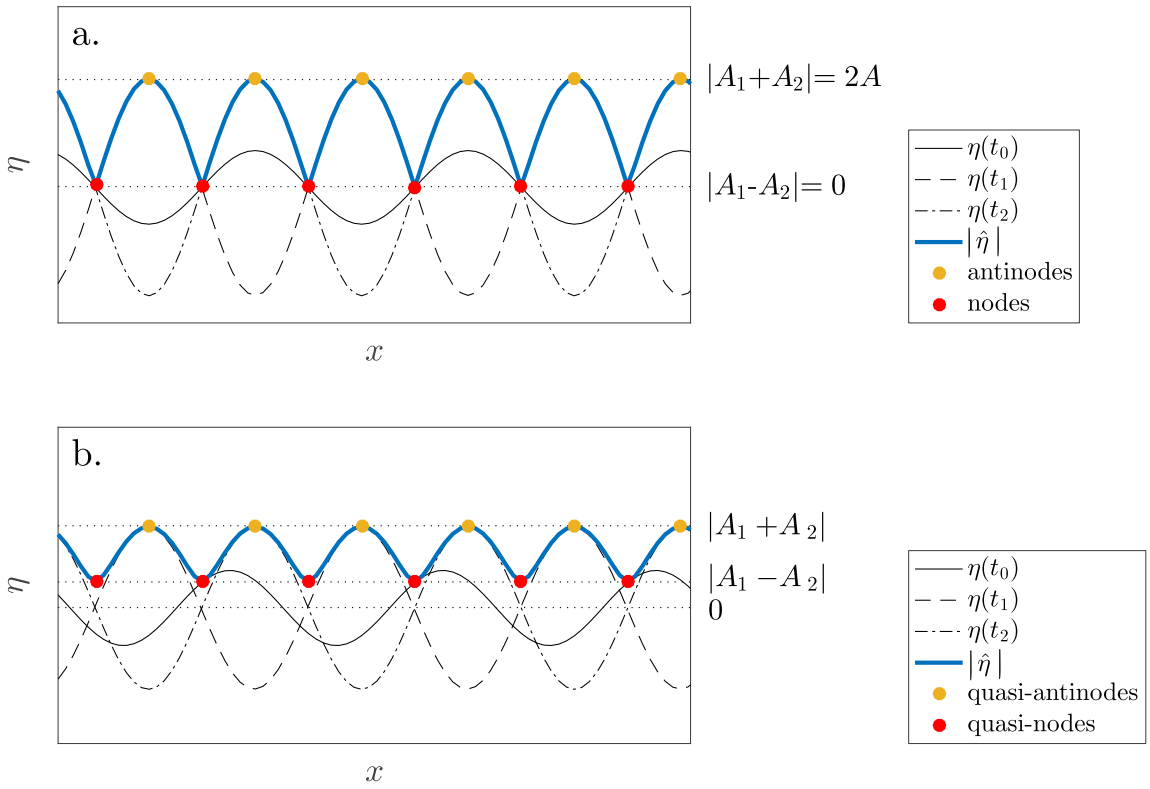

Figure 4.2: Sketch of the water surface elevation envelope $|\hat{\eta}|$ for wave trains with the same amplitude: $A_1 = A_2$ (plot a), and different amplitude $A_1 \neq A_2$ (plot b). Plot a performs a standing wave pattern where the cross-shore undulation of $|\hat{\eta}|$ is formed of nodes and antinodes, whereas the undulation of $|\hat{\eta}|$ in plot b is formed of quasi-nodes and -antinodes. $\eta(t_0)$, $\eta(t_1)$ and $\eta(t_2)$ are the water surface elevation at three different time instants.

tical motion are called antinodes and nodes, respectively. Furthermore, the fact that $c_1 = -c_2$ suppresses any cross-shore wave motion. When $A_1 \neq A_2$ the resulting wave field is no longer a standing wave. The minimal vertical elevation is now $|A_1 - A_2| \neq 0$ and the cross-shore envelope performs an undulation formed of quasi-nodes and quasi-antinodes (see Figure 4.2b). As a result, there is a progressive wave motion in the direction of the dominant wave train. In general, when $A_1 \neq A_2$ and $|c_1| \neq |c_2|$, the cross-shore envelope $|\hat{\eta}|$ performs an undulation with quasi-antinodes and quasi-nodes.

Although node-antinode notation should only be applied to standing waves, henceforth, the locations where two wave trains are in phase will be known as antinodes, whereas the locations where two wave trains are in antiphase will be known as nodes.

4.3.2 Nodes and antinodes in pairs of wave trains

For a given wave frequency, 2 waves trains with different propagation characteristics (celerities) always build a cross-shore undulating pattern consisting of nodes and antinodes. Therefore, the simultaneous propagation of n different wave trains will develop N different node-antinode patterns, where

$$N = \frac{n!}{2!(n-2)!}. \tag{4.6}$$

N performs the number of combinations of unordered subsets of 2 wave trains within a certain set of n propagating wave trains. For instance, 3 different wave trains build 3 different cross-shore node-antinode patterns, whereas 5 different wave trains build 10 different node-antinode patterns. Instead of analysing all the node-antinode patterns in one, a practical approximation for the purpose of this chapter is to analyse individually the resulting node-antinode pattern of pairs of wave trains.

In this section, the location of a set of nodes and antinodes belonging to a pair of wave trains is analytically solved for flat beds using linear wave theory. Likewise, this analytical solution is extended to a pair of wave trains propagating on changing water depths.

Flat bed

Given 2 propagating wave trains whose angular frequency is ω and their amplitudes and wave-numbers are $[A_1,\ A_2]$ and $[k_1,\ k_2]$, respectively, the associated potential is

$$\phi(X,y,z) = \Re\{-i\frac{g}{\omega}\left(A_1\,K_{p,1}(z)\,e^{i(\omega t+k_1\,X+\phi_1)} + A_2\,K_{p,2}(z)\,e^{i(\omega t+k_2\,X+\phi_2)}\right)\} \tag{4.7}$$

where $K_p(z) = \cosh(k(z+h))/\cosh(k\,h)$, h is the water depth, g is the gravitorial acceleration and i is the imaginary unit. Equation 4.7 may be rewritten in terms of the functions $a(X,z)$ and $\varphi(X)$ as

$$\phi(X,y,z) = \Re\{-i\frac{g}{\omega}\,a(X,z)\,e^{i(\varphi(X)-\omega\,t)}\}, \tag{4.8}$$

whose resulting surface elevation is

$$\begin{aligned}\eta(X,t) &= -\frac{1}{g}\left|\frac{\partial\phi}{\partial t}\right|_{z=0}\\ &= a(X,0)\,\cos(\varphi(X)-\omega t).\end{aligned} \tag{4.9}$$

From Equation 4.9, $a(X,0)$ is the envelope of the surface elevation. Using the identity $e^{i\alpha} = \cos(\alpha) + i\sin(\alpha)$, where α is a convenient variable, the expression of the envelope $a(X,0)$ that satisfies Equation 4.8 is

$$\begin{aligned}[a(X,0)]^2 &= [A_1\,\cos(k_1\,X-\phi_1) + A_2\,\cos(k_2\,X-\phi_2)]^2\\ &+ [A_1\,\sin(k_1\,X-\phi_1) + A_2\,\sin(k_2\,X-\phi_2)]^2\\ &= {A_1}^2 + {A_2}^2 + 2\,A_1\,A_2\,\cos(X(k_1-k_2)+(\phi_1-\phi_2)).\end{aligned} \tag{4.10}$$

At the antinodes, $a(X,0)$ is maximum by definition and conversely, at the nodes, $a(X,0)$ is minimal. Based on Equation 4.10, $a(X,0)$ is maximum and minimal when $\cos(X(k_1-k_2)+(\phi_1-\phi_2)) = \pm 1$, respectively. Therefore,

$$X_{anti} = \frac{2\pi m}{|k_1-k_2|} - \frac{\phi_1-\phi_2}{k_1-k_2}, \quad \text{with } m\in\mathbb{N} \tag{4.11}$$

$$X_{node} = \frac{\pi(2m+1)}{|k_1-k_2|} - \frac{\phi_1-\phi_2}{k_1-k_2}, \quad \text{with } m\in\mathbb{N}. \tag{4.12}$$

Consequently, the distance between consecutive antinodes (identical between

nodes) is

$$L = \frac{2\pi}{|k_1 - k_2|} = \frac{2\pi}{\omega} \left| \frac{c_1\, c_2}{(c_2 - c_1)} \right|. \tag{4.13}$$

Note that, in general the distance between antinodes (or nodes) is independent of the amplitude of the involved wave trains, but dependent only on their propagation characteristics, that is, their phase velocities. Furthermore, according to Equations (4.11) and (4.12), the observation of the undulation pattern of an experimental wave train on a flat bed composed of linear superposition of two waves would provide information of their wave phases and celerities.

Sloping bed

The immediate effect of wave trains propagating on a sloping bed is the progressive reduction of their phase velocity as the water depth reduces. Therefore, the cross-shore wave celerity changes as a function of the cross-shore bathymetry, and, in general, $c = c(x)$ is valid. In this context, the equivalent wave number corresponding to the propagating wave train j is

$$k_j = \frac{\omega}{X} \int_0^X \frac{1}{c_j} dX. \tag{4.14}$$

As a result, the following implicit expressions are a generalization of Equations 4.11 and 4.12 for wave trains propagating on uneven bathymetries:

$$\int_0^{X_{anti}} \left| \frac{1}{c_1} - \frac{1}{c_2} \right| dX = \frac{2\pi m - |\phi_1 - \phi_2|}{\omega}, \qquad \text{with } m \in \mathbb{N} \tag{4.15}$$

and

$$\int_0^{X_{node}} \left| \frac{1}{c_1} - \frac{1}{c_2} \right| dX = \frac{\pi(2m+1) - |\phi_1 - \phi_2|}{\omega}, \quad \text{with } m \in \mathbb{N}, \tag{4.16}$$

where X_{node} and X_{anti} are the locations of a set of nodes and antinodes, respectively.

Note that, no specification has been done about the relative propagation direction between the two wave trains throughout this section. The wave number k_j and wave train celerity c_j are positive quantities when the propagation of the wave train j is computed against X (origin at the wave paddle and positive towards the shoreline). Conversely, these are negative quantities when the wave train propagates with increasing X (see Figure 3.2 for the X-coordinate reference).

4.3.3 A theoretical example of propagating wave trains

It is illustrative to show by mean of an example the cross-shore behaviour of several wave trains of the same frequency travelling with different propagation characteristics. Using Equations (4.2) to (4.4), theoretical lf wave signals have been created propagating over a 1:100 beach slope mimicking the Wave Evolution Flume. The theoretical lf wave amplitude pattern induced by the presence of the ILW propagating with the primary waves group velocity (bounded to the wave groups) and the OFLW is displayed in Figure 4.3. Likewise, the theoretical lf wave amplitude pattern induced by the same combination of ILW and OFLW plus the IFLW (spurious) is displayed in Figure 4.4. The theoretically designed pattern corresponds to the lf wave motion at f_g observed for the wave condition *B-1* (see Table 3.1 for more details). The used theoretical amplitude and phase at the wave paddle (X_0) for each wave train at f_g and the ILW growth rate α ($A^{ILW} \sim h^{-\alpha}$ as observed by Battjes et al. (2004) and Van Dongeren et al. (2007), among others) are displayed in Table 4.1. The theoretical bathymetry, showed in Figures 4.3-*d* and 4.4-*d*, replicates the 1:100 sloping bed built in the Wave Evolution Flume.

Figure 4.3 presents the case of 2 wave trains at f_g: a group-bound ILW propagating shoreward with its reflected wave at the shoreline travelling seaward (OFLW). In Figure 4.3, the lf wave amplitude (blue solid line in plot *a*) and the envelope of the surface elevation $\hat{\eta}$ (blue solid line in plot *b*) presents the expected progressive growth as the water depth reduces, but riding on top, a node-antinode pattern exists with almost constant space separation between nodes or antinodes. Furthermore, the locations of these antinodes are in very good agreement with the theoretical location computed by Equation (4.15) using

$$k_1 = -\widetilde{k_B} = -\frac{2\pi f_g}{X} \int_0^X \frac{1}{|c_{gp}|}\, dX, \tag{4.17}$$

and

$$k_2 = \widetilde{k_F} = \frac{2\pi f_g}{X} \int_0^X \frac{1}{|c_g|}\, dX. \tag{4.18}$$

where k_1 is the wave number of the wave train 1 propagating as an incident long wave with the wave groups celerity (bound), whereas k_2 is the wave number of a free long wave propagating seaward.

This is consistent with the existence of only 2 wave trains travelling in opposite

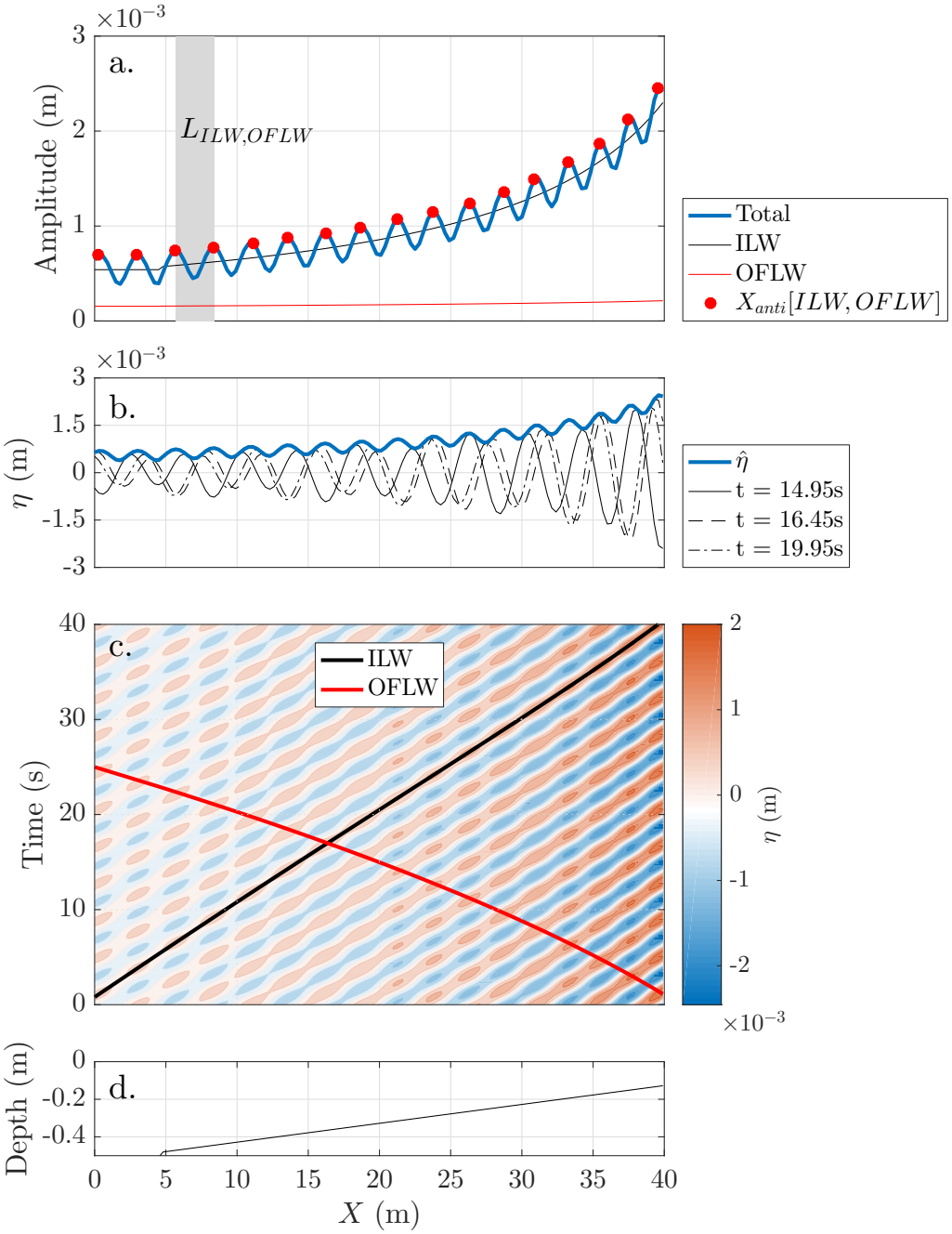

Figure 4.3: Theoretical propagation of 2 wave trains travelling in opposite directions (ILW and OFLW). Plot *a* shows the cross-shore evolution of the Total, ILW and OFLW amplitudes. X_{anti} [ILW,OFLW] is the set of computed locations of the antinodes using Equation 4.15. $L_{ILW,OFLW}$ (shaded area) is the flat-bed approximation of the mean distance between antinodes (Equation (4.13)). Plot *b* shows the water surface elevation at three different time instants alongside with its envelope. Plot *c* shows the η contour plot where the time-space trajectories of ILW and OFLW are highlighted. Plot *d* illustrates the cross-shore water depth.

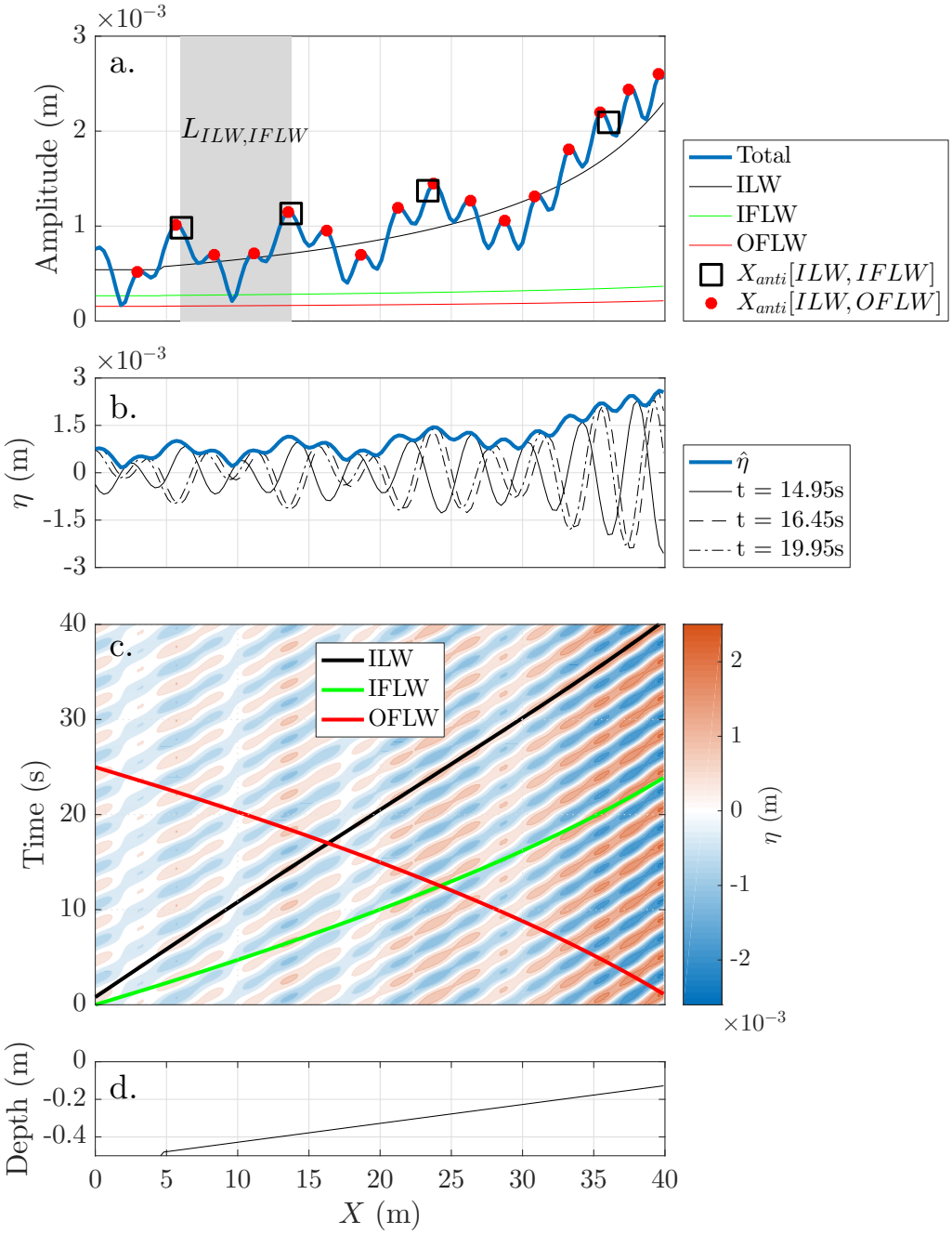

Figure 4.4: Theoretical propagation of 3 wave trains (ILW, IFLW and OFLW). Plot *a* shows the cross-shore evolution of the total and respective amplitudes. X_{anti} [ILW,IFLW] and X_{anti} [ILW,OFLW] are the set of computed locations (using Equation 4.15) of the antinodes belonging the pairs [ILW, IFLW] and [ILW, OFLW], respectively. $L_{ILW,IFLW}$(shaded area) the flat-bed approximation (Equation (4.13)) of the mean distance between antinodes for [ILW, IFLW]. Plot *b* shows the water surface elevation at three different time instants alongside with its envelope. Plot *c* shows the η contour plot where the time-space trajectories of ILW, IFLW and OFLW are highlighted. Plot *d* illustrates the cross-shore water depth.

Table 4.1: Wave amplitude and phase at $X = 0$ of the ILW, IFLW and OFLW for the theoretical simulation based the bichromatic wave group condition *B-1*. α is the ILW growth rate.

	Figure 4.3	Figure 4.4
A_0^{ILW} (m)	$5.33 \cdot 10^{-4}$	$5.39 \cdot 10^{-4}$
ϕ_0^{ILW} (rad)	2.39	2.32
α	1.05	1.05
A_0^{IFLW} (m)	-	$2.59 \cdot 10^{-4}$
ϕ_0^{IFLW} (rad)	-	3.45
A_0^{OFLW} (m)	$1.49 \cdot 10^{-4}$	$1.58 \cdot 10^{-4}$
ϕ_0^{OFLW} (rad)	2.06	1.35

directions (ILW and OFLW). Actually, $L_{ILW,OFLW} = 2.65$m showing that Equation (4.13) is a good a estimation of the mean distance between the antinodes in the vicinity of the wave generation. Therefore, the use of the flat-bed approximation (Equation (4.13)) to explain the distance between observed antinodes is a simple and reliable procedure to determine whether the existing waves travel in the same or opposite direction. However, a more accurate calculation about the location of the antinodes, using Equation (4.15), is needed to confirm whether the propagating waves are free or bound components.

The dominance of the ILW over OFLW is clear in Figure 4.3-*a*, where the ILW growth rate (as observed by the measured α parameter in *B-1*) is larger than the linear shoaling of the OFLW. This dominance is also noticeable in Figure 4.3-*c*, where the time-space evolution of the surface elevation highlights a dominant ingoing propagation in agreement with the time-space trajectory of the ILW. Therefore, the relative importance between the existing wave trains may be qualitatively inferred from the observation of the cross-shore amplitude evolution and main propagation trajectory.

Figure 4.4 presents the case of 3 wave trains at f_g: a group-bound ILW propagating shoreward alongside with a IFLW and a OFLW, which are a spurious incident free wave and the resultant reflected wave at the shoreline, respectively. In plots *a* and *b*, the envelope of the surface elevation presents 2 clear node-antinode patterns, which confirms the coexistence of at least 3 wave trains. The first node-antinode pattern involves the ILW and IFLW, whose antinodes at locations X_{anti} [ILW,IFLW] are successfully estimated by Equation (4.15). Once again, $L_{ILW,IFLW} = 7.05$m showing that Equation (4.13) is a good estimation of the initial distance between the antin-

odes. Note the different propagation celerity of the ILW and IFLW showed in Figure 4.4-c as the ILW travels with the wave group velocity and the IFLW as a free wave. The second node-antinode pattern is the one involving the ILW and OFLW, which has been already explained in Figure 4.3. A third node-antinode pattern potentially develops due to the interference between the IFLW and OFLW. However, this third pattern is not noticeable in Figure 4.4 (masked by the previous two node-antinode patterns) because the wave amplitude of both the IFLW and OFLW are far lower than the ILW one.

4.3.4 Towards a qualitative wave separation

The observation of the cross-shore amplitude evolution and space-time progagation provides useful qualitative information about the existing long wave components, their nature (bound/free) and propagation direction. The following steps provide the strategy to determine the number of involved wave trains, identify their ingoing or outgoing nature and to indicate which is the dominant one at a certain frequency within a stationary signal:

i Identification of different node-antinode patterns. Given a measured lf wave time series at different cross-shore locations with enough resolution, the number N of existing node-antinode patterns is usually different from the number N^* of node-antinode patterns that an observer may identify analysing the undulations of the cross-shore envelope $\hat{\eta}$. The meaning of N and N^* is clearly seen in the example presented with Figure 4.4. In this example, 2 clear node-antinode patterns were identified ($N^* = 2$), whereas 3 node-antinode patterns actually exist ($N = 3$). Therefore, if an observer identifies exactly N different node-antinodes patters ($N^* = N$), then, using Equation 4.6, the number n of existing wave trains is the positive solution of the equation $n^2 - n - 2N = 0$. That is,

$$n = \frac{1 + \sqrt{1 + 8N}}{2}. \tag{4.19}$$

However, since $N^* \leq N$ in practice, the number of existing wave trains n based on the observation of N^* different node-antinode patterns is

$$n \geq \lceil 0.5\,(1 + \sqrt{1 + 8N^*})\rceil, \tag{4.20}$$

where the operator $\lceil \cdot \rceil$ rounds the element to the nearest higher integer.

ii Identification of the free or bound nature of the existing wave trains and their propagation direction. Two wave trains can propagate in the same direction or in opposite direction to each other. Therefore, depending on their nature (free or bound), the following pairs may exist at a certain frequency: [free$^+$, free$^-$], [bound$^+$,free$^+$] and [bound$^+$,free$^-$], where the sign indicates the propagation direction. Each of the previous pairs build a node-antinode pattern and, therefore, identifying which of the above pairs are involved in a certain cross-shore structure may be achieved using Equation (4.13) as a valid approximation of the mean distance between antinodes for each existing undulating pattern.

iii Determination of the dominant wave train. The overall trajectory of the surface elevation crests in the time-space contour plot matches with the trajectory of the dominant wave train. This is the case in Figure 4.4-*c*, where the time-space propagation of the surface elevation crests is very well described by the ILW trajectory. Consequently, the ILW dominantes over the IFLW and the OFLW.

Note that this strategy requires a dense cross-shore resolution. Therefore, in order to identify any node-antinode pattern whose mean distance between antinodes is L, the data set cross-shore resolution (Δx) must satisfy $\Delta x \leq L/2$.

The presented analysis provides qualitative but useful information about the existing wave trains and their behaviour before performing any proper wave separation procedure. Furthermore, this preliminary analysis allows a critical assessment of the wave separation procedure that is presented next.

4.4 The problem of wave separation

For a certain frequency f, the water surface elevation η_f formed of n wave trains is

$$\eta_f(X,t) = \Re\left\{\left[\sum_{j=1}^{n} Z^j(X)\right] e^{i(2\pi f t)}\right\}, \tag{4.21}$$

where Z^j is the complex amplitude for each wave train j at any cross-shore location. Consequently, the wave separation procedure consists in obtaining Z^j for each existing wave component. The separation technique focuses on distributing the wave

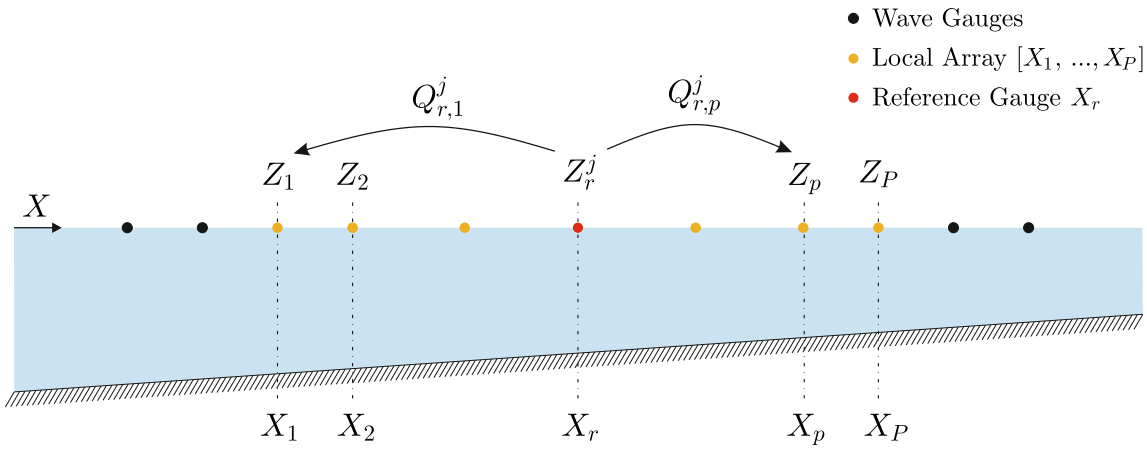

Figure 4.5: Schematic layout of the separation method.

energy budget at the target frequency f among the n wave components (i.e., ILW, IFLW and OFLW) based on their different propagation characteristics along a number of P wave gauges (local array). That is, the separation at the reference location X_r is computed by solving a linear system that involves local wave data from adjacent positions X_p within the local array (see Figure 4.5). Working in the frequency domain, that system is defined as:

$$Z_p = \sum_{j=1}^{n} \left(Q^j_{r,p} \, Z^j_r \right), \tag{4.22}$$

where $Q^j_{r,p} = K^j_{r,p} \cdot e^{i\Phi^j_{r,p}}$ represents the propagation coefficient of any wave train j from X_r to X_p. K and Φ are factors that perform the cross-shore evolution of the amplitude and the phase, respectively, based on the nature of the wave train (they will be properly addressed below).

Most of the available wave-separation techniques (Kostense, 1985, Lin & Huang, 2004, Battjes et al., 2004, Van Dongeren et al., 2007, among others) are based on the above described methodology to separate lf components. The differences of these techniques consist of the number of wave trains involved in the linear system presented in Equation (4.22) and their respective amplitude and phase cross-shore propagation. However, performing a successful wave separation requires a previous understanding of the target surface elevation series (Section 4.3.4) in order to adapt the separation procedure to the existing wave trains, and intuition to critically assess the wave separation outcomes.

The wave separation methodology addressed in this section is performed in the

frequency domain and can be applied to any frequency adapting the procedure to the propagation nature of the existing components (free or bound). The particular case of wave separation of wave components occurring at subharmonics of the primary waves, e.g., at f_g, is explained in the next section.

4.4.1 Separation of the group-bound ILW, IFLW and OFLW

Considering the existence of the group-bound ILW (Equation (4.2)), IFLW (Equation (4.3)) and OFLW (Equation (4.4)) at f_g, the separation procedure is performed within a local array composed of P locations (see Figure 4.5). As a result, the overdetermined version of the system presented in Equation (4.22) is:

$$\begin{pmatrix} Q_{r,1}^{ILW} & Q_{r,1}^{IFLW} & Q_{r,1}^{OFLW} \\ Q_{r,2}^{ILW} & Q_{r,2}^{IFLW} & Q_{r,2}^{OFLW} \\ \vdots & \vdots & \vdots \\ Q_{r,p}^{ILW} & Q_{r,p}^{IFLW} & Q_{r,p}^{OFLW} \\ \vdots & \vdots & \vdots \\ Q_{r,P}^{ILW} & Q_{r,P}^{IFLW} & Q_{r,P}^{OFLW} \end{pmatrix} \begin{pmatrix} Z_r^{ILW} \\ Z_r^{IFLW} \\ Z_r^{OFLW} \end{pmatrix} = \begin{pmatrix} Z_1 \\ Z_2 \\ \vdots \\ Z_p \\ \vdots \\ Z_P \end{pmatrix}, \tag{4.23}$$

where the ILW travels as a group-bound wave and the IFLW and OFLW as free waves. For free waves, the wave celerity c reduces as the water depth reduces following the Dispersion Equation. Therefore, the cross-shore amplitude evolves following the theoretical linear shoaling (flux energy conservation is preserved during cross-shore propagation) and the shoaling coefficient Sh applies. Consequently, the amplitude and phase propagation factors for IFLW and OFLW are

$$K_{r,p}^{IFLW} = K_{r,p}^{OFLW} = Sh_{r,p} = \sqrt{\frac{c_{g,r}}{c_{g,p}}}, \tag{4.24}$$

$$\Phi_{r,p}^{IFLW} = \Phi_{r,p}^{OFLW} = 2\pi f_g \int_{X_r}^{X_p} \frac{1}{c}\, dX, \tag{4.25}$$

where the celerity (c) and the group celerity (c_g) are negative for waves propagating shoreward (IFLW), but positive for the waves propagating seaward (OFLW).

The group-bound ILW requires particular considerations. As in Equation (4.2), its amplitude growth is assumed to follow a function of the local depth raised to a power α (Van Dongeren et al., 2007). The computation of α is iterative, as it will

be explained below, with an initial guess $\alpha = 1$. A good approximation of the phase velocity is the linear theory group velocity at the mean frequency of the primary waves, c_{gp} (Equation (2.9)). Therefore, the amplitude and phase propagation factors for the group-bound ILW are

$$K_{r,p}^{ILW} = (h_r/h_p)^{\alpha}, \tag{4.26}$$

$$\Phi_{r,p}^{ILW} = 2\pi f_g \int_{X_r}^{X_p} \frac{1}{c_{gp}}\, dX. \tag{4.27}$$

where c_{gp} is negative since the group-bound ILW propagates shoreward.

4.4.2 Performance of the separation procedure

For a given water surface elevation at a certain frequency (η_f), the separation of the ILW, IFLW and OFLW as described by the linear system (4.23) depends on the size of the local array (P) and the parameter α (Equation (4.26)).

Formally, a local array consisting of 3 different gauges ($P = 3$) is enough to solve the system (4.23). However, if the phase difference across the gauges forming the local array is relatively small, the separation procedure becomes highly sensitive to noise. Therefore, Battjes et al. (2004) suggest a minimum array length to obtain a stable outcome when separating an experimentally measured η_f. In the present study, the separation procedure is generally computed with $P = 25$ to guarantee the stability of the separation procedure and a smooth evolution of the separated components.

Once the length of the local array is chosen, the separation technique is computed iteratively. The α-value is initially set to 1 and after a first separation solving the system (4.23), the resulting ILW is immediately used to re-compute α. Using the function $\beta h^{-\alpha}$ as a good estimation of the ILW growth, α and β are the best fit parameters over the cross-shore ILW amplitude. The α-value is usually seen to converge in no more than 5 iterations.

Figure 4.6 illustrates the separation of the theoretical case presented in Figure 4.4. Since η is a theoretical wave field generated by superposition of different wave trains, the ILW, IFLW and OFLW are successfully separated using a local array with $P = 3$. The stability of the solution is clear in Figure 4.6-*a* where the theoretical (real) and separated (Sp) components are coincident. Furthermore, the convergence

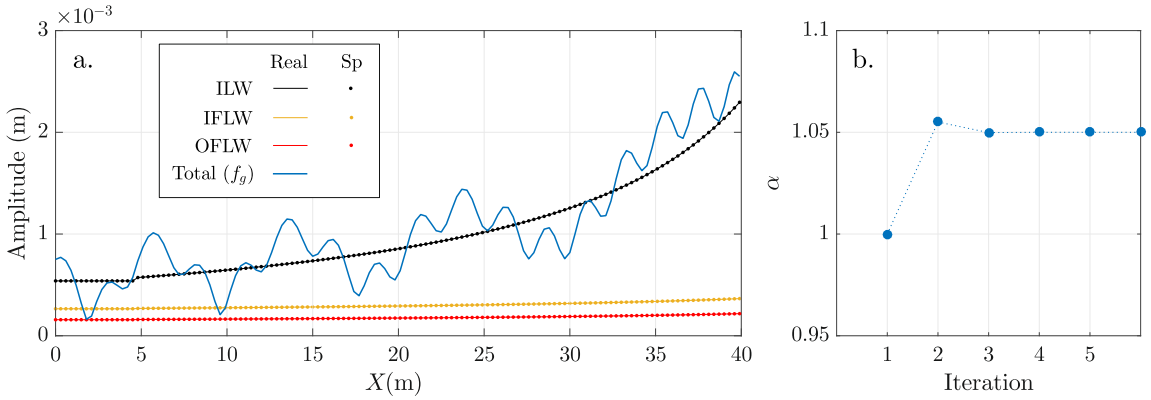

Figure 4.6: Outcomes from the separation of the ILW, IFLW and OFLW from the theoretical wave case presented in Figure 4.4. The separation is computed using a local array consisting of 3 adjacent wave gauges ($P = 3$). Plot a shows the cross-shore amplitude evolution of the theoretical (Real) and the Separated (Sp) components, whereas plob b illustrates the convergence of the α-parameter.

of α is achieved after 3 iterations (Figure 4.6-b).

4.5 Wave generation based on a lf correction

The outcome from an ideal wave generation at f_g should only include the group-bound ILW and the OFLW reflected or radiated from the opposite end. This requires an accurate second-order generation with active wave paddle absorption damping any free ingoing long wave. If the wave paddle software does not allow this second-order generation or the active absorption system can not absorb the outgoing long wave (due to paddle stroke limitation at very low frequencies), the presence of energy propagating shoreward as a free wave (IFLW) is noticeable. A correction methodology is proposed here in order to improve the wave paddle generation of long waves. The correction uses a generation-separation-correction procedure in which the spurious free long waves are separated and suppressed. The methodology is performed in the following steps:

1. After an initial wave generation (first-order input), the water surface elevation signal is measured with a dense array of sensors close to the wave paddle. Any existing IFLW is identified as explained in Section 4.3.4, and separated using the local array technique with the solving scheme presented in Section 4.4.1. Therefore, A_X^{IFLW} and ϕ_X^{IFLW} are achieved at this stage.

2. Back propagation of the separated IFLW in any cross-shore location X provides

its initial amplitude and phase at the wave paddle as:

$$A_0^{IFLW} = \frac{A_X^{IFLW}}{Sh_X} \tag{4.28}$$

$$\phi_0^{IFLW} = \phi_X^{IFLW} - 2\pi f \int_0^X \frac{1}{c}\, dX \tag{4.29}$$

where Sh is the linear shoaling coefficient and c is the celerity of freely propagating waves. Note that c is negative since the IFLW propagates shoreward.

3. The new input for the wave generation consists in adding a Correction Wave (CW) at the target frequency f to the original first-order input. The initial amplitude and phase of the CW are:

$$A_0^{CW} = A_0^{IFLW} \tag{4.30}$$

$$\phi_0^{CW} = \phi_0^{IFLW} + \pi. \tag{4.31}$$

Consequently, the interaction between the IFLW and the CW results in a total destructive interference at the wave paddle and no IFLW propagates shoreward.

In practice, this methodology provides similar results to a theoretical second-order wave generation function with the inconvenience that it requires measuring and effectively correcting the wave generation at every frequency.

4.5.1 lf correction at the group frequency

For the experimental wave case *B-1* (*IBIMS-ICL* data set), Figure 4.7 illustrates the cross-shore amplitude evolution of f_g and its separated components (group-bound ILW, IFLW and OFLW) before (plots *a* and *b*) and after (plots *c* and *d*) the lf correction in the wave generation is applied.

Before the correction, the total amplitude at f_g performs two clear node-antinode patterns in Figure 4.7-*a*. Consequently, at least 3 different wave components coexist at f_g according to Equation (4.20). The longer node-antinode pattern, whose distance between antinodes is $L = \mathcal{O}(10\text{m})$, corresponds to the linear superposition of the group-bound ILW and the IFLW, whereas the shorter one ($L = \mathcal{O}(1\text{m})$) corresponds to the linear superposition of the group-bound ILW and the OFLW. Since

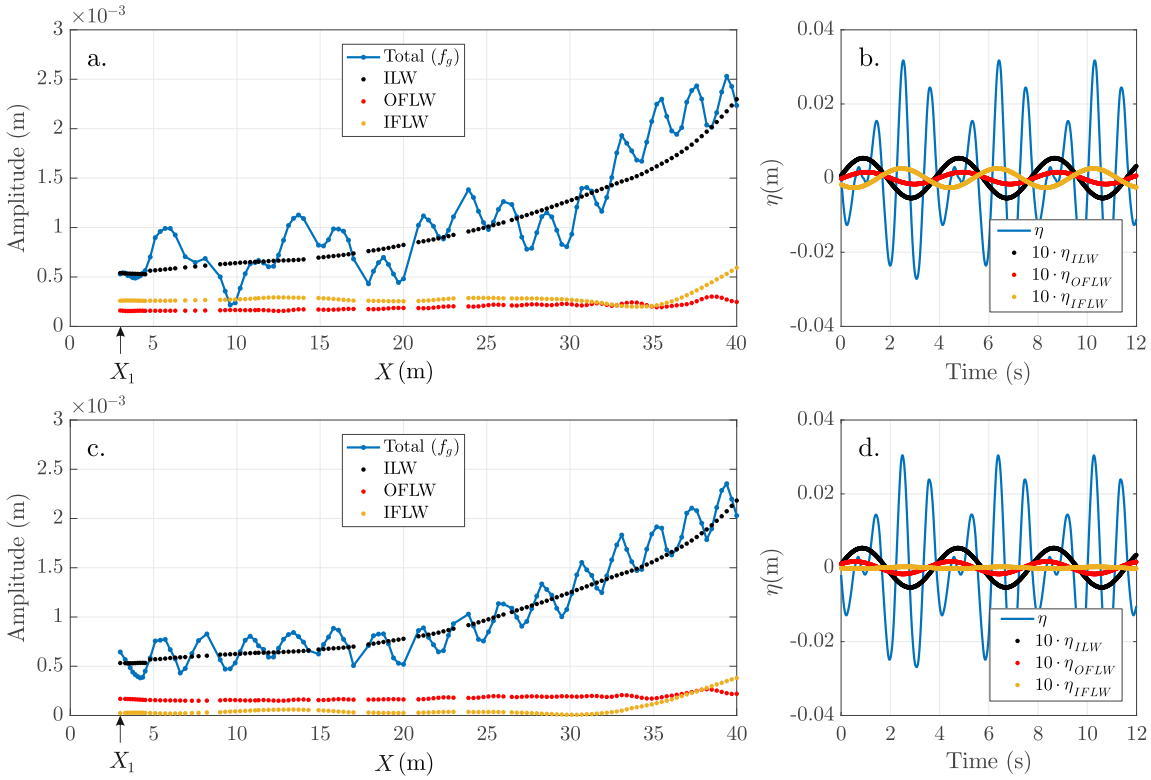

Figure 4.7: Wave case *B-1* belonging to *IBIMS-ICL* data set before (plots *a* and *b*) and after (plots *c* and *d*) the lf correction procedure. Plots *a* and *c* show the amplitude cross-shore evolution of the total energy at f_g and its ILW, OFLW and IFLW components, whereas plots *b* and *d* show the water surface elevation time series at X_1 with the separated components at f_g multiplied by a factor of 10.

the amplitude of the antinodes belonging to [ILW, IFLW] is larger than the associated to [ILW, OFLW], then $A^{IFLW} > A^{OFLW}$. Certainly, this is confirmed by the outcome from the separation procedure. Both IFLW and OFLW behaves as free waves whose growth is consistent with linear shoaling. In contrast, the growth of the group-bound ILW is very well described by the coefficient $(h_0/h)^{-\alpha}$, where $\alpha = 1.05$ in this particular case. Likewise, the ILW is, as expected, in antiphase with the envelope of the hf wave group (plot *b*). The smooth pattern (no undulations) of the separated ILW, IFLW and OFLW validates the separation procedure and confirms that no more components exists at f_g.

After the correction, the total amplitude at f_g performs only one node-antinode pattern in Figure 4.7-*c*, which is the resultant from the pair [ILW, OFLW]. The outcome from the separation procedure confirms the effective suppression of the IFLW, whose amplitude in plot *c* is negligible. Table 4.2 shows the amplitude and

Table 4.2: Amplitudes and phases obtained at X_0 (wave paddle location) of the existent wave components at f_g for the experimental wave case *B-1* (*IBIMS-ICL* data set) before and after lf correction.

	Before	After
A_0^{ILW} (m)	$5.39 \cdot 10^{-4}$	$5.33 \cdot 10^{-4}$
ϕ_0^{ILW} (rad)	2.32	2.39
A_0^{IFLW} (m)	$2.59 \cdot 10^{-4}$	$0.24 \cdot 10^{-4}$
ϕ_0^{IFLW} (rad)	3.45	3.88
A_0^{OFLW} (m)	$1.58 \cdot 10^{-4}$	$1.49 \cdot 10^{-4}$
ϕ_0^{OFLW} (rad)	1.35	2.06

phase back-propagated to the paddle location (X_0) of the separated components before and after the lf correction. The initial amplitudes of the ILW and the OFLW remain practically the same, whereas the reduction of the IFLW amplitude after lf correction is about 91% of its amplitude before correction. Note that the unexpected growth of the IFLW from $X = 35$m shoreward in plots *a* and *c* is not realistic. This is due to limitations of the separation procedure to properly separate waves propagating in the same direction whose both phase velocities tend to converge into $\sqrt{gh}$ when approaching shallow water.

4.5.2 lf correction at subharmonics of the group frequency

The lf correction and separation method described in section 4.5 is a general procedure that, although described for the group frequency (generally the dominant lf component), it can be applied to any frequency component. Accurate long wave generation requires correction of spurious waves at the group frequency, and subharmonics and superharmonics of the group frequency (when relevant). This section describes the separation technique performed at subharmonics of f_g.

Several authors have already reported the presence of lf waves at frequencies resultant of the repetition period of an specific wave group structure (Baldock et al. (2000), Alsina et al. (2016) or Moura & Baldock (2018), among others). These are energetic wave components at lower frequencies than the group frequency f_g, like f_r. For instance, when $Rp = 3$ (3 wave groups per repetition period as in Figure 3.5-*c*), $f_r = f_g/3$, and $2f_r$ is also an energetic component. The generation and dynamics of long waves occurring at frequencies lower than the group frequency will be explained

in detail in chapter 7. The experimental study of this type of long waves requires an accurate wave generation at this lower frequency range and second-order correction at frequencies below f_g, like f_r. During wave group shoaling the nonlinear interaction between triads leads to energy growth of superharmonics and subharmonics of the primary frequencies. When $Rp = 3$, the subharmonics f_g, $2f_r$ and f_r mainly receives energy from the primary wave components f_1 and f_2. A lf correction in any of the above low frequencies is experimentally observed to have implications in the rest. Therefore, in order to experimentally perform a successful correction for every single lf components, each component has to be corrected (following steps 1-3) in an energetic-descending order, i.e., f_g is corrected in the first place, followed by $2f_r$ and f_r. This procedure is illustrated in Figure 4.8 as a diagram for cases with $Rp = 3$: The initial input is just linear consisting of the primary frequencies f_1 and f_2. After wave generation, the signal $\eta^{(I)}$ is measured along the flume, where the superscripts indicates the stage of the lf correction sequence. The outcome from the correction steps 1-3 is the wave train WC(f_g) that effectively suppresses the IFLW at f_g. This sequence is repeated for frequencies $2f_r$ (stage II) and f_r (stage III). Therefore, the final input consists of the primary frequencies [f_1, f_2] and the corresponding corrections WC(f_g), WC($2f_r$) and WC(f_r). The final outcome from this wave generation is the corrected signal $\eta^{(IV)}$. The performance of this procedure is illustrated in Figure 4.9 for the wave case *MR-03* (*DIFFREP-ICL* data set) with satisfactory results.

Figure 4.9 illustrates the cross-shore amplitude of $\eta^{(I)}$ at f_g (plot *a*), $2f_r$ (plot *b*) and f_r (plot *c*), and the cross-shore amplitude of $\eta^{(IV)}$ at f_g (plot *d*), $2f_r$ (plot *e*) and f_r (plot *f*). The separated components are also illustrated in Figure 4.9. At f_g, the ILW is dominant before correction, followed by the IFLW (plot *a*), which is successfully suppressed after correction (plot *d*). At f_r and $2f_r$, the ILW is negligible during wave group shoaling and only the IFLW and OFLW are present (plots *b* and *c*). After applying the lf correction at f_r and $2f_r$, plots *e* and *f* confirm that the IFLW is successfully suppressed.

4.5.3 Validation of the experimental wave cases

In order to verify a proper suppression of the lf spurious waves throughout all the experimental wave cases presented in this thesis, Figures 4.10 and 4.11 illustrate the

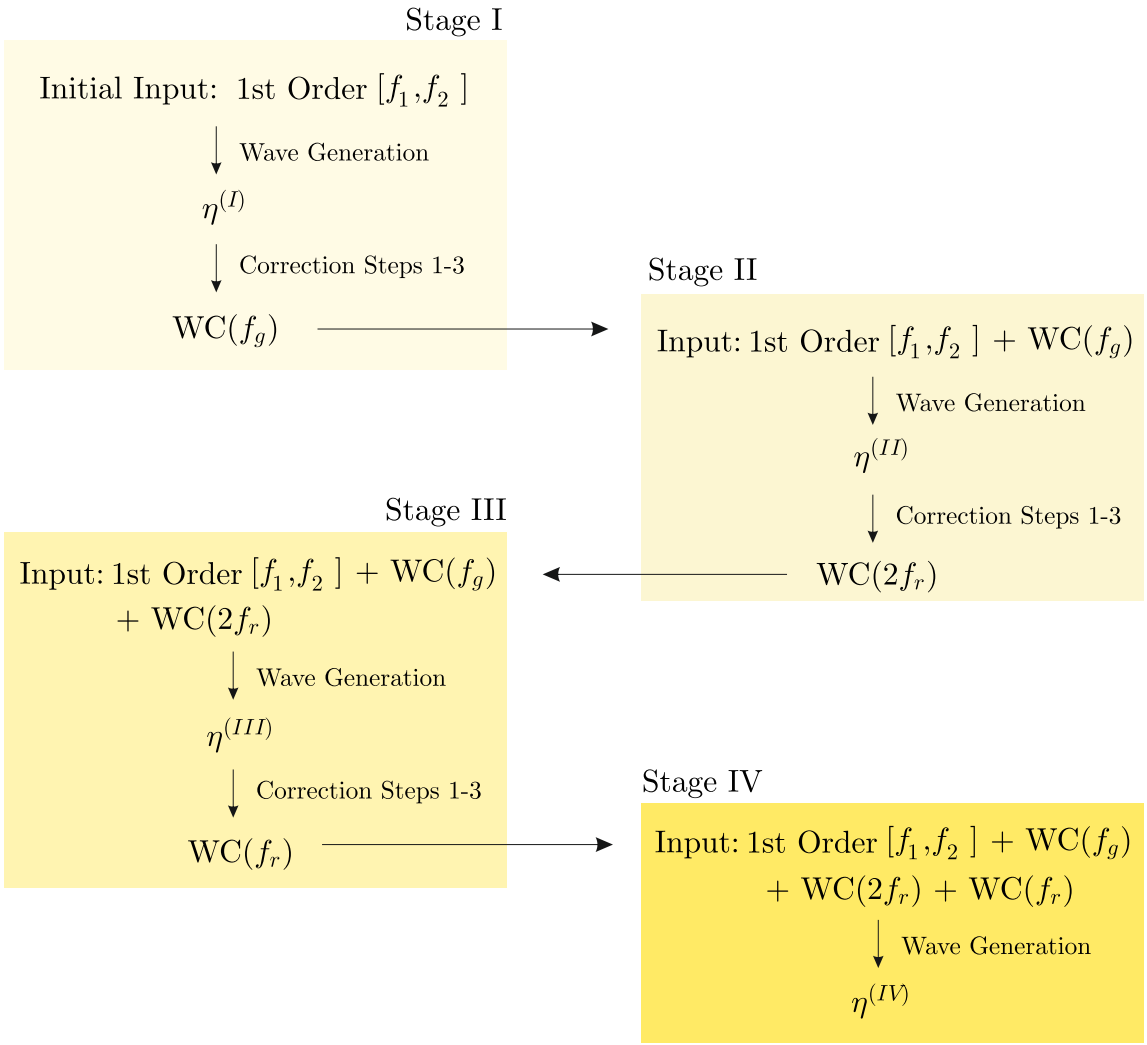

Figure 4.8: Diagram about the lf correction procedure applied to the lf energetic components f_g, $2f_r$ and f_r for a wave case with $Rp = 3$.

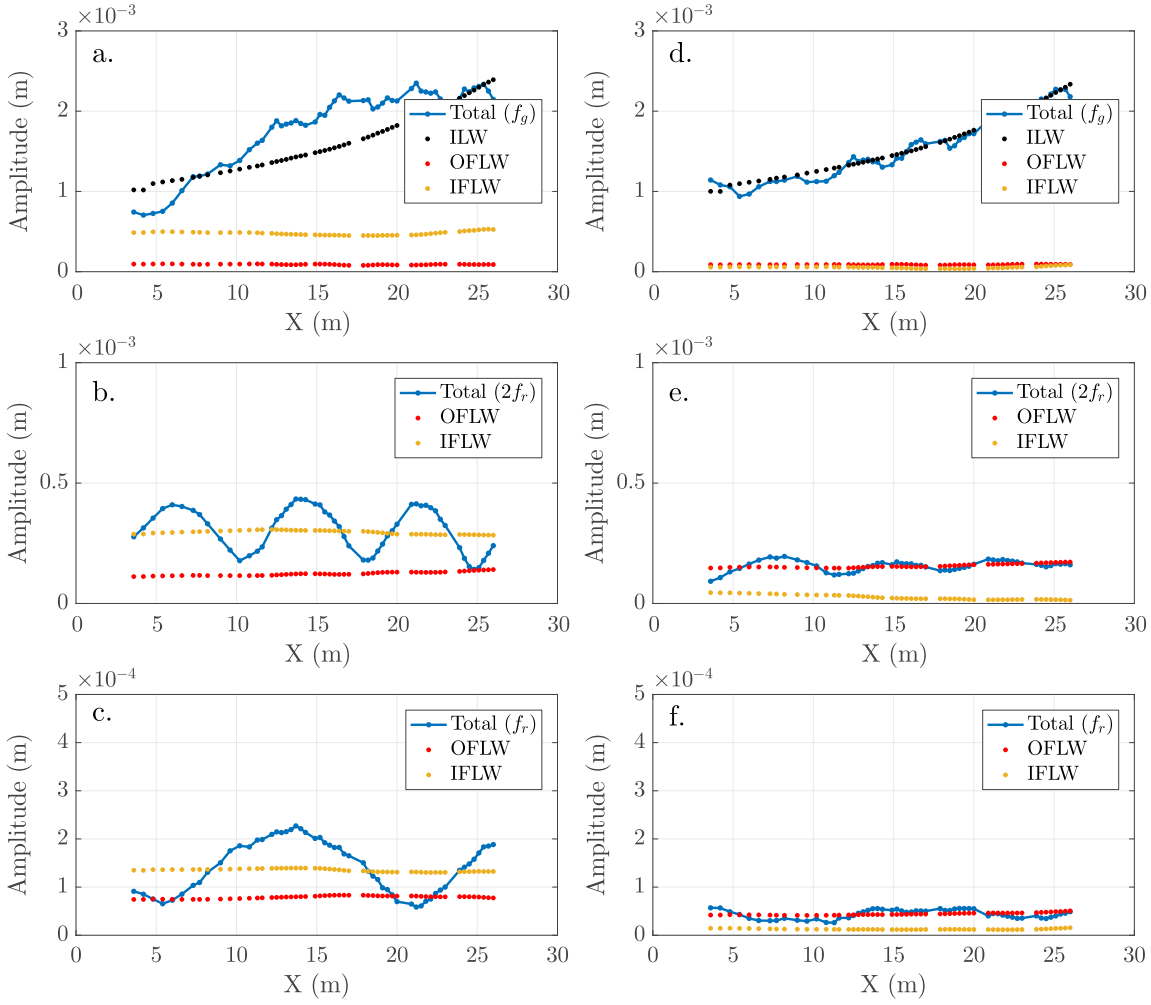

Figure 4.9: Wave case *MR-03* belonging to *DIFFREP-ICL* data set before (plots *a*, *b* and *c*) and after (plots *d*, *e* and *f*) the lf correction procedure. Plots *a* and *d* show the cross-shore amplitude at f_g, with the separated components ILW, IFLW and OFLW. Plots *b* and *e* show the cross-shore amplitude at $2f_r$, with the separated components IFLW and OFLW, whereas plots *c* and *f* show the corresponding ones to f_r.

amplitude of the IFLW before and after the lf correction for the *IBIMS-ILC* and *DIFFREP-ILC* data sets, respectively. The efficiency of the procedure is assessed by the suppression percentage after correction.

Wave cases forming the *IBIMS-ILC* data set are characterized by $Rp = 1$, where f_g is the only lf energetic component. Therefore, Figure 4.10 accounts for the IFLW at f_g only, showing the IFLW amplitude before and after the lf correction (plot *a*). Note that, the magnitude of the IFLW decreases in general with increasing frequencies. Overall, the IFLW amplitude after correction is $\mathcal{O}(10^{-4}\text{m})$. In relative terms, plot *b* shows the IFLW suppression percentage, where most of the cases successfully suppress above 60% of the spurious energy, increasing to nearly 90% for some cases.

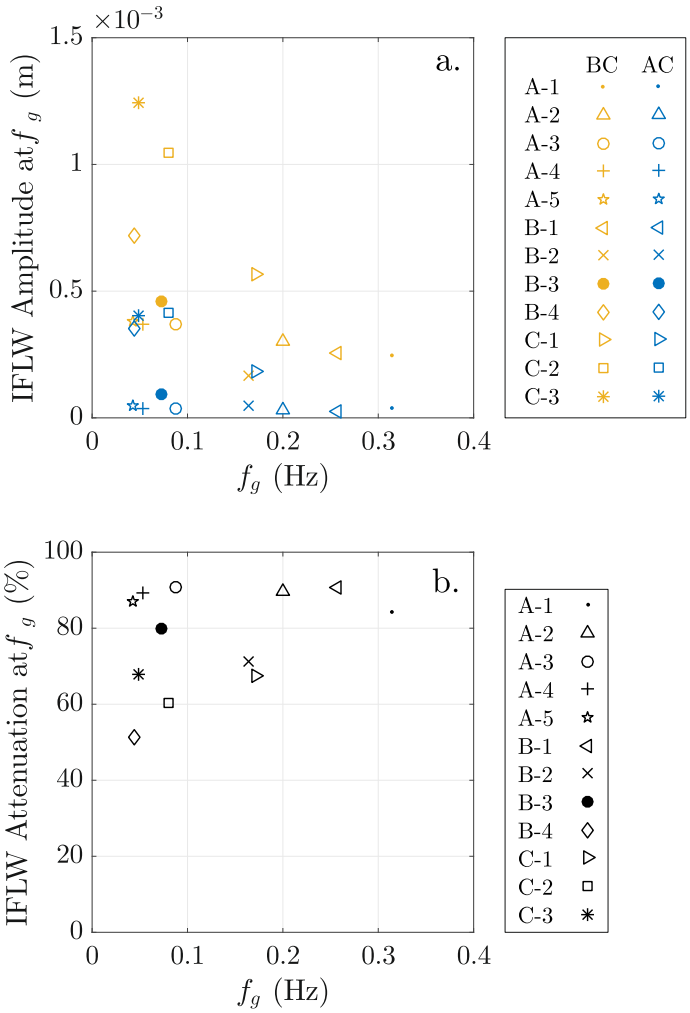

Figure 4.10: Plot *a* shows the IFLW amplitude at f_g before and after the lf correction is applied for *IBIMS-ILC* data set. Plot *b* shows the IFLW attenuation percentage. The amplitudes are provided at the first measuring location (X_1).

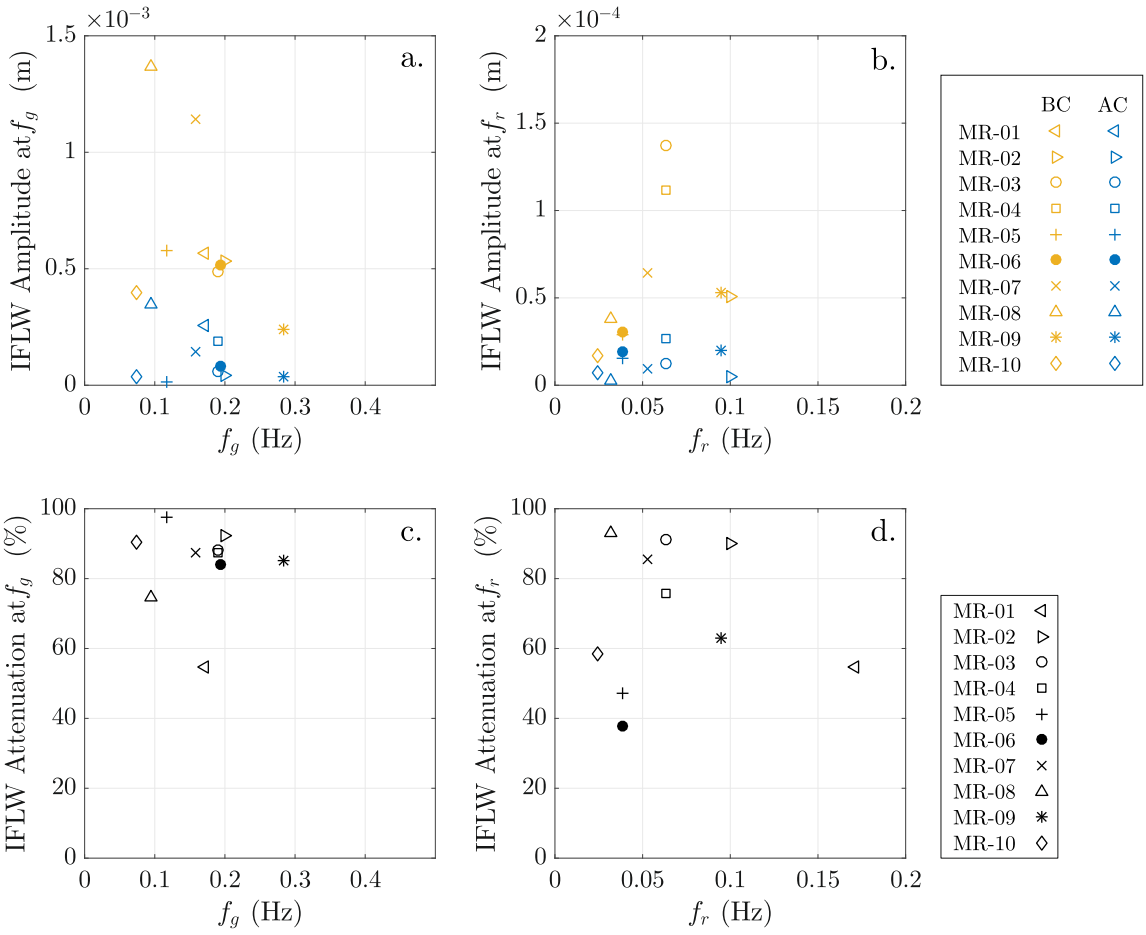

Figure 4.11: Plots *a* and *b* show the IFLW amplitude at f_g and f_r, respectively, before and after the lf correction is applied for *DIFFREP-ILC* data set. Plots *c* and *d* show the IFLW attenuation percentage at f_g and f_r, respectively. The amplitudes are provided at the first measuring location (X_1).

In contrast, wave cases forming the *DIFFREP-ILC* data set are characterized by a range of Rp with a variety of lf components at the lf domain. In this case, Figure 4.11 only illustrates the IFLW suppression at f_g and f_r. At f_g, the suppression percentage is in general above 90 % (plot c) and the resulting IFLW amplitude after correction is $\mathcal{O}(10^{-4}\text{m})$ (plot a). At f_r, Figure 4.11-d shows a decay in the efficiency of the correction procedure (overall above 60 %) compared with f_g (overall above 80%). However, the resulting IFLW amplitude at f_r is $\mathcal{O}(10^{-5}\text{m})$, which is an order of magnitude below the IFLW at f_g.

4.6 Concluding remarks

Wave generation machines based on first-order wave generation theory give rise to unwanted (spurious) waves. Furthermore, these spurious waves may potentially increase with re-reflections at the wave paddle since the efficiency of the active wave absorption at the wave paddle usually decays for low frequencies. In this context, the existence of these spurious waves, in particular lf spurious waves, is very inconvenient for a proper study of the wave-group dynamics and the associated lf water motions that will be addressed in the upcoming chapters.

The development of a second-order wave generation theory and its implementation in wave machines is itself a challenge beyond the purposes of this PhD thesis. Instead, this chapter proposes a lf correction procedure to successfully suppress between 60% to 90% of the spurious energy content. In practice, this methodology provides similar results to a theoretical second-order wave generation, with satisfactory results for the bichromatic waves conditions forming the *IBIMS-ILC* and *DIFFREP-ILC* data sets.

When a number n of wave trains travel with different propagation characteristics, their linear superposition results in a number N of different cross-shore undulating patterns formed of nodes and antinodes. However, the actual number n of existing wave trains is usually an uncertainty. In this context, this chapter propose a simple procedure using linear wave theory to identify the number of existing wave trains and their nature (free or bound). This methodology is based on the analysis of the nodes and antinodes forming the cross-shore undulating patterns. Moreover, a wave separation procedure is also presented in this chapter with excellent results

separating both theoretical and measured wave fields. This separation procedure is based on previous wave separation methods, but improved for performing and correctly separating the group-bound ILW at the group frequency.

5

Influence of the group modulation on short wave breaking on a mild slope

Author's Note: The results of this chapter have been partially published in Padilla & Alsina (2017).

5.1 Chapter overview

This chapter describes the influence of the wave group modulation on high frequency (hf) wave components. The immediate consequence studied in this chapter is the influence of the different wave modulation on the individual depth-induced breaking of the short waves forming the groups.

This chapter begins with the tracking of the individual crests forming the groups during shoreward propagation. This allows a proper description and identification of the individual breaking events within the wave-group structure. The influence of the group modulation, controlled by the group frequency, and lf components on the short wave breaking is confirmed through the differences in (1) the breaking onset and (2) the wave-height to water-depth ratio (γ) within the surf zone, for a range of different group frequencies. Subsequently, a physical explanation of this influence is given by the analysis of the substancial nonlinear transformations undergone by the

wave groups during shoaling, i.e. losses of vertical and horizontal wave symmetry. In particular, these horizontal symmetry losses are explained in terms of nonlinear energy transfers from the primary frequencies to the hf components.

5.2 Introduction

The presence of wave groups of short gravity waves implies the existence of more than one frequency component in the wave energy frequency distribution. The simplest wave group modulation case is described by bichcromatic wave groups generated by two components of similar frequency. These are the primary frequencies f_1 and f_2 whose linear superposition defines the first-order water surface elevation:

$$\eta^{(I)} = \eta_{f_1} + \eta_{f_2}. \tag{5.1}$$

Biésel (1952) and Longuet-Higgins & Stewart (1962) evaluated the nonlinear wave-wave interactions of the primary components and proposed a second-order solution to the water surface elevation:

$$\eta^{(II)} = \eta^{(I)} + \eta_{2f_1} + \eta_{2f_2} + \eta_{f_1+f_2} + \eta_{f_1-f_2}, \tag{5.2}$$

where self-interaction (η_{2f_1}, η_{2f_2}) and cross-interaction terms ($\eta_{f_1+f_2}$, $\eta_{f_1-f_2}$) define the second-order wave components. Regarding the generation of lf motions (difference term $\eta_{f_1-f_2}$), the solution proposed by Biésel (1952) and (Longuet-Higgins & Stewart, 1962) for a grouped wave train in a finite water depth results in group-bound Ingoing Long Waves (ILWs) in antiphase with the envelope of the primary waves.

During shoreward propagation of bichromatic wave groups, the nonlinear interactions between different wave components cause energy transfers between those component within the wave spectrum (Phillips, 1960, Hasselmann et al., 1963). The nonlinear coupling between components and the associated energy transfers occur to frequency components above ($2f_1$, $2f_2$ and f_1+f_2) and below (f_1-f_2) the primary frequencies. In particular, the nonlinear energy transfer to the difference frequencies is associated to the growth of the ILW during shoaling (Janssen et al., 2003, De Bakker et al., 2015), whereas energy transfer to high frequencies results in changes in the

shape of individual short waves (Elgar & Guza, 1985, Doering & Bowen, 1995). As a result, short waves progressively change in wave shape, from a nearly sinusoidal profile in deep water to more skewed waves in shallow water characterized by sharp crests and flat broad troughs (Guza & Thornton, 1982, Elgar & Guza, 1985, Doering & Bowen, 1995). Along with the amplitude evolution, the phase of the different hf harmonics changes during shoaling leading to a relatively steepening of the wave shape face. The lack of horizontal symmetry in the wave shape (i.e. sharper crests and trough flattening) is known as skewness whereas the lack of vertical wave symmetry or its tendency to become pitched forward is called wave asymmetry.

The local nonlinearity of hf waves propagating across a natural beach is important to sediment transport (Ruessink et al., 2009). Wave skewness and asymmetry increase during shoaling and eventually the hf waves will break. After breaking, the remaining hf energy still drives water oscillations to the shoreline. However, due to hf energy dissipation during breaking, the wave energy close to the shoreline may be dominated by lf wave motions, specially in dissipative beach conditions.

5.2.1 Experimental data

The experiments used in this chapter belong to *IBIMS-ILC* data set, whose wave conditions design, measuring process and signal post-processing can be found in section 3.3. These experiments were carried out in the Wave Evolution Flume at Imperial College London. The description of the facilities, instrumentation and experimental setup can be found in section 3.2.

For this analysis, 12 bichromatic wave cases have been used. Fully modulated wave groups have been generated, characterized by an exact repetition of wave groups in the time series, $T_r = T_g$. The wave groups propagation over a gentle beach slope (1:100) have been measured with a dense array of resistive wave gauges. Table 3.1 summarises the information about the wave conditions used in this chapter.

5.3 Breaking of the incident hf grouping waves

5.3.1 Tracking of the short waves forming the wave groups

The high spatial resolution of the present data enables a quasi-continuous tracking of individual wave crests in the spatial and temporal domain. In Figure 5.1-*a*, a contour plot of the time and space distribution of the water surface elevation is illustrated. In the space-time domain, the trajectory, s, of an individual crest n (where n is the label of the wave crest) can be tracked by computing the propagation time of the crest n between wave sensors at known cross-shore locations. Therefore, the discrete trajectory of a high frequency wave crest n can be obtained from its celerity defined by

$$\frac{\mathrm{d}s(x_i, n)}{\mathrm{d}t} = \frac{\Delta x_i}{\Delta \tau_i}, \tag{5.3}$$

where Δx is the separation between wave sensors and $\Delta \tau$ is the time-lag computed using cross-correlation functions $R_{\eta,\eta}$ as described in Appendix B.

Figure 5.1-*a* reveals the trajectories, s, of the different wave crests (colored lines) forming a wave group. The individual crests tend to follow slightly parallel trajectories to each other, which means that the wave celerity is very similar for every single crest and very well described by the celerity c_p of free propagating waves at the mean primary frequency f_p. This is validated using the trajectory of a single wave crest as a reference to compare the relative time-shift with the adjacent remaining crests. In Figure 5.2, the water surface elevation contour plot is displayed with respect to the cross-shore location (x) and time shift (δ) between the individual wave-crests and the reference wave crest $n = 10$ at $\delta = 0$. If the wave crests propagate with the same celerity, then the relative time-shift between them must be a constant quantity ($\delta = const$). Indeed, this is the case in Figure 5.2 since the crests forming the groups perform straight lines until they approach the shallow water limit (black dashed line).

By following the crest elevation along s in Figure 5.1, the wave crest breaking process and location are characterized accurately (accuracy of ± 0.05m in the horizontal distance) as the maximum crest elevation within a trajectory. Since the short wave breaking event takes place over the crests themselves, this process may only appear along the trajectory s for each crest forming the group. In Figure 5.1-*a* the wave breaking location of individual wave crests is illustrated with circles. Each wave crest forming the group breaks at a different location and, overall, the sequence

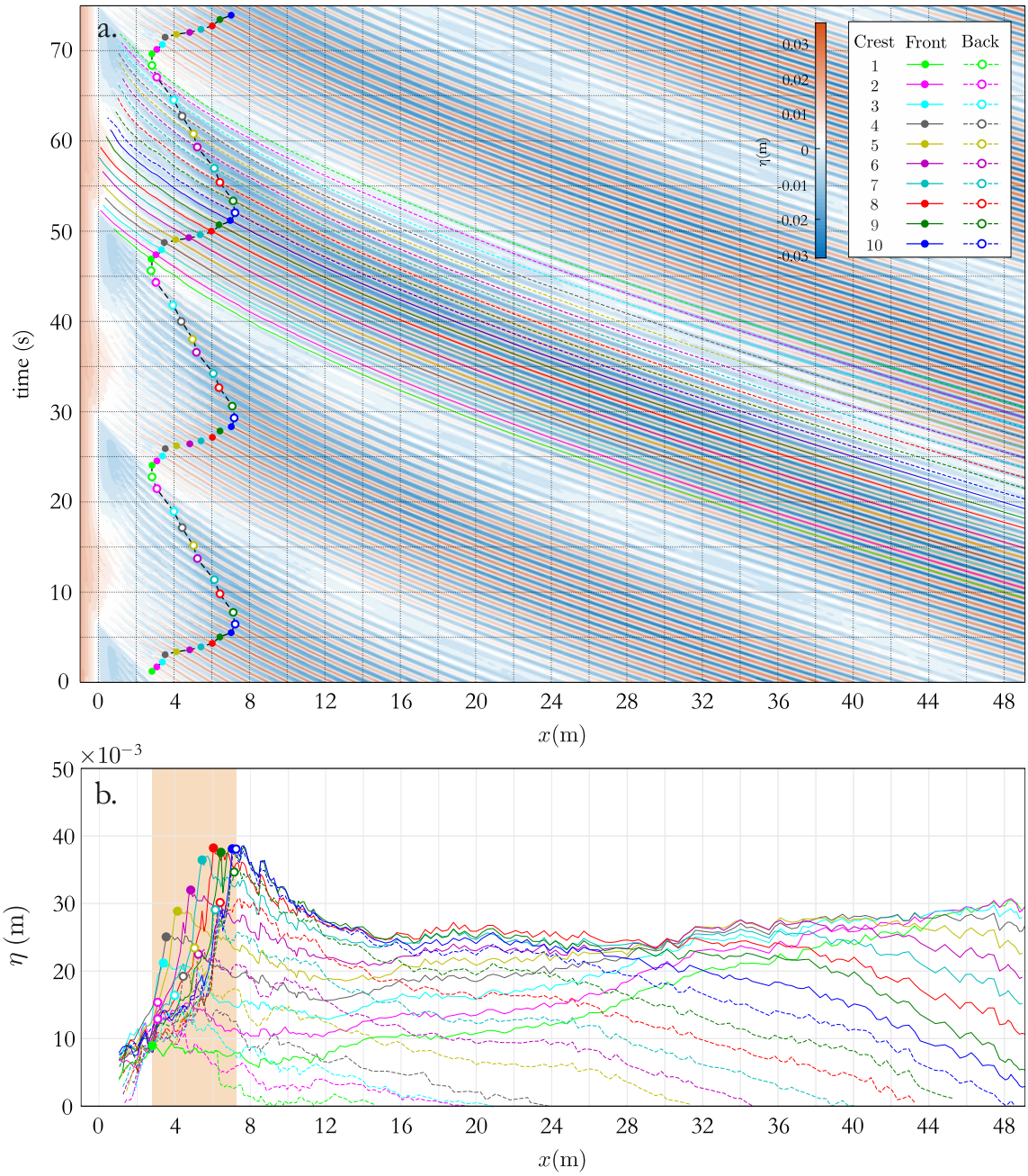

Figure 5.1: Contour plot of water surface elevation for case *B-4*. The individual wave crests as they propagate over the space-time plane are illustrated in plot *a* and the crest elevations (with respect to the mean water level) along the trajectories *s* are presented in plot *b*. The breaking location of individual waves is marked with coloured circles. The shading zone in plot *b* represents the breaking excursion.

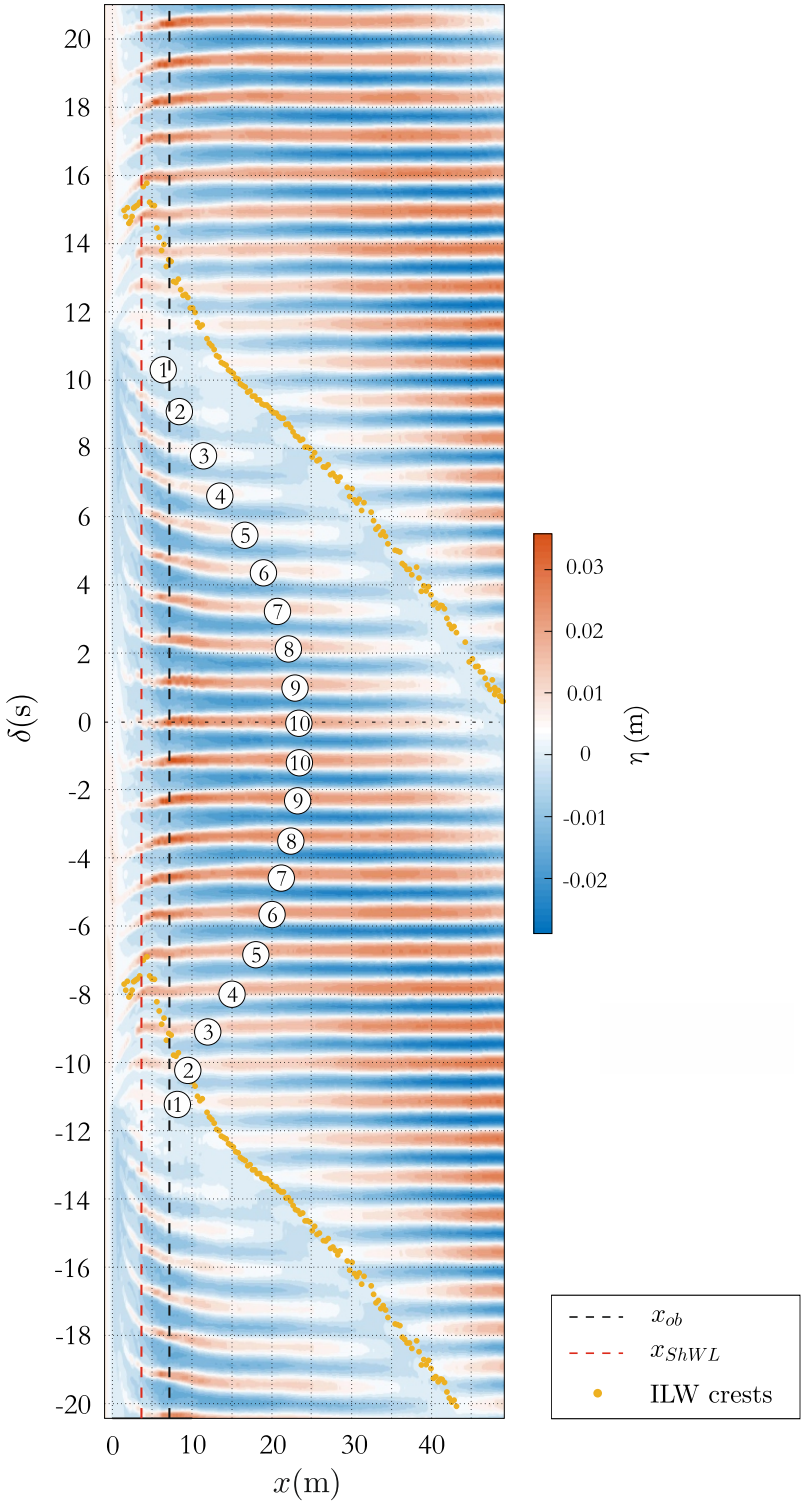

Figure 5.2: Contour plot of the water surface elevation for the wave condition *B-4* in terms of the cross-shore location and time-shift δ with respect to the central crest 10. The black dashed line indicates the shallow water limit, whereas the red dots show the trajectories of the group-bound ILW crests.

of breaking events defines a moving breakpoint. The spatial width of the moving breakpoint is the breaking excursion Δx_b.

The water surface elevation along individual crest trajectories s projected onto the axis x is presented in Figure 5.1-*b*. The breaking location is clearly identified as the drastic decrease of the crest height as the wave crests propagate. The breaking excursion Δx_b is displayed as the shaded area in plot *b*. The distribution of the breaking events follows a pattern given by the wave group modulation as illustrated also in plot *a*. However, analogous crests within the wave group (those with the same color) break at remarkably different crest elevations depending on whether they are at the front or back of the group (although the crest elevation is initially the same). This breaking sequence is extended to the rest of the crests forming the groups and allows distinguishing between wave breaking at the frontside and the backside of the group.

5.3.2 The effective water depth within the surf zone

The frontside (solid circles) always consists of higher breaking crests compared with the backside (open circles) in Figure 5.1-*b*. This different breaking behaviour is caused by the existence of long waves at the wave group frequency (η_{f_g}). Figure 5.3 illustrates a set of time series at 5 fixed cross-shore locations across the surf zone. These time series show the evolution of the wave groups from $x = 7.43$m, where no breaking is observed, to $x = 3.23$m, where the grouping modulation has been lost almost completely. The time evolution of the moving breakpoint is already illustrated in Figure 5.1-*a* (black dashed line with colored dots) where the waves at the frontside break earlier in time and at locations closer to the shoreline compared to similar waves at the backside. Likewise, Figure 5.3 shows the distribution of the individual waves breaking within the group. The breaking process starts in the centre of the group, with the highest waves, and the sequence moves to the adjacent ones at both sides, with a slight dominance for the backside where the effective depth is reduced due to the long wave presence (see yellow line in Figure 5.3). Across the surf zone, the wave group modulation is strongly reduced and the initial crest of the wave group turns into a flat sequence of bores that will eventually dissipate their energy close to the shoreline. The reduction in the wave groupiness due to the breaking of the largest waves is consistent with earliest observations of Veeramony & Svendsen

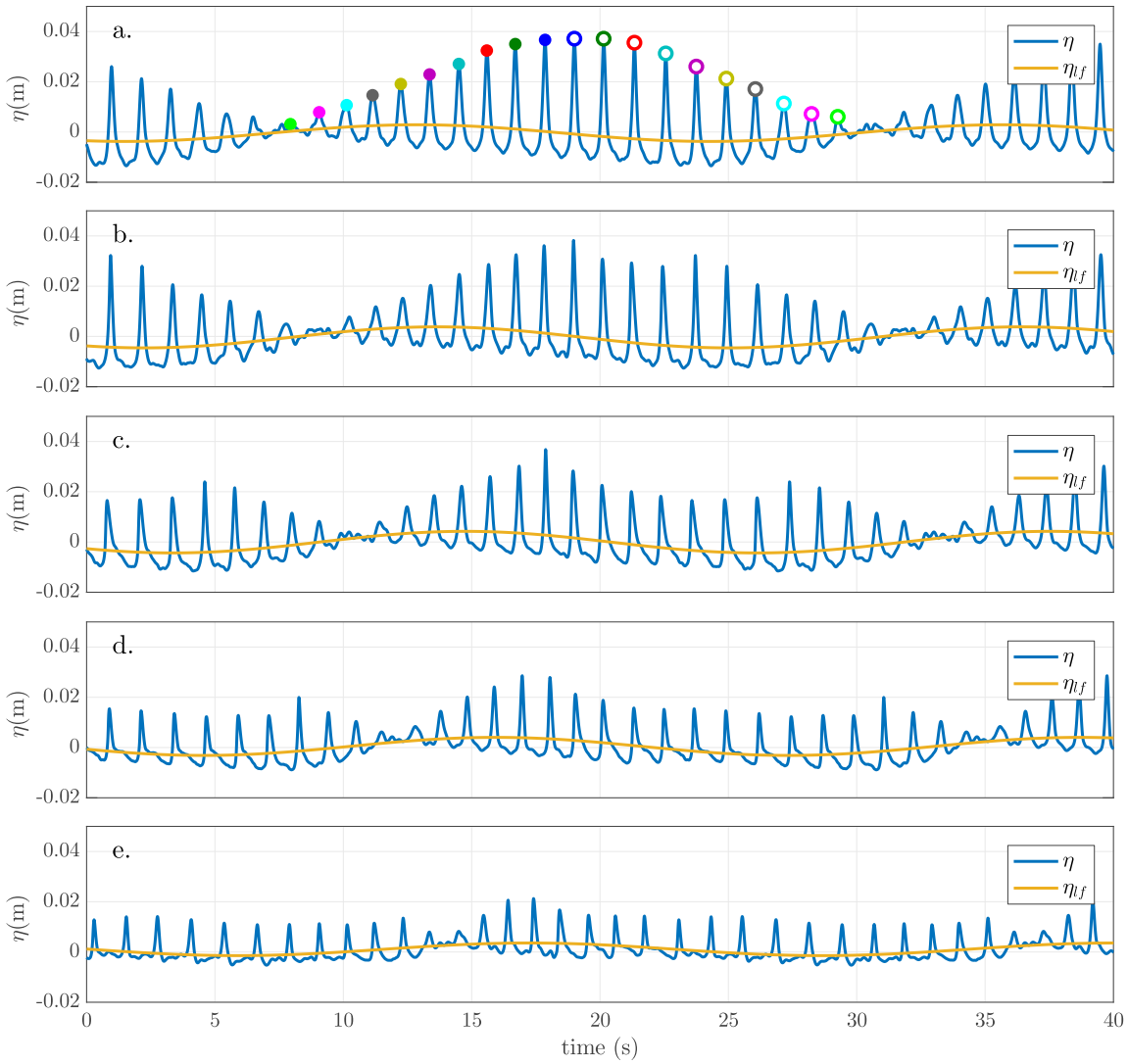

Figure 5.3: Water surface elevation time series belonging to wave condition *B-4* at different locations within the surf zone: $x = 7.43$m (a); $x = 6.43$m (b); $x = 5.43$m (c); $x = 4.43$m (d) and $x = 3.23$m (e). η_{lf} is the low-pass filtered water surface elevation signal to account for the lf components. The wave crests are marked using the same color scheme as in Figures 5.1.

(1997).

Assuming a depth-induced breaking, the wave height to depth ratio γ offers a good description of the breaking sequence when the water depth is corrected with the measured low frequency amplitude. Figure 5.4 shows the wave height at breaking versus the effective depth $h^*(x,t) = h(x) + \bar{\eta}(x) + \eta_{lf}(x,t)$, where the still water depth h has been corrected with the mean water surface elevation, set down $\bar{\eta}$, and lf oscillations, η_{lf}. It is evident that this correction requires accurate time-space breaking identification, which does not present a problem due to the aforementioned

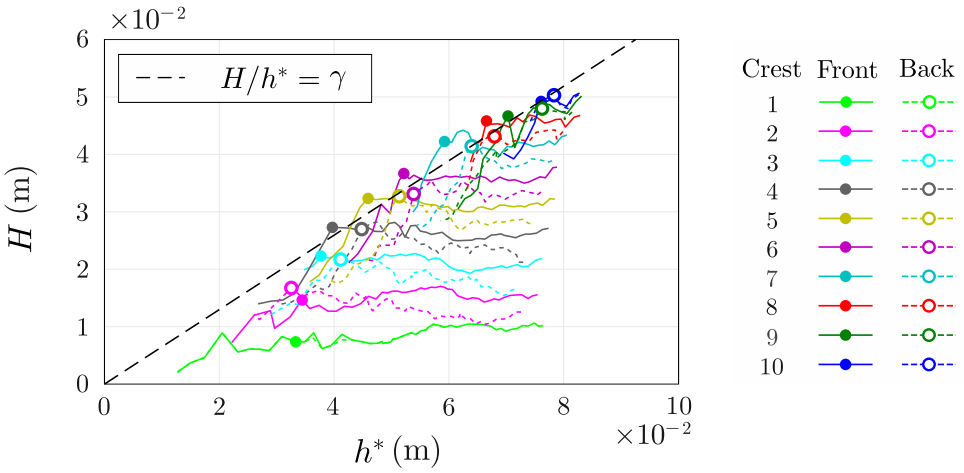

Figure 5.4: Wave height ($H = \eta_{crest} - \eta_{through}$) versus the actual water depth h^* for each crest forming the wave condition *B-4*. The wave crests are marked using the same color scheme as in Figures 5.1.

dense resolution. For this specific case, *B-4*, the ILW dominates the lf signal and is out of phase, slightly lagging behind the hf wave group structure (List, 1992, Janssen et al., 2003, Battjes et al., 2004). Therefore, it is responsible for larger breaking wave heights at the frontside of the wave groups. When the water depth at the breaking location is corrected with the lf waves, the wave height at breaking shows a linear distribution with the effective water depth as illustrated by a dashed line in Figure 5.4.

A secondary effect of the effective water depth reduction due to the long wave presence is the so-called *bore merging* phenomenon and it is noticeable in Figure 5.2. After the breaking onset, the individual bores travel to shallow water depths, where their propagation celerities depend on the water depth only ($c_p \approx \sqrt{gh}$). The back-sided crests (top half crests, 1 to 9, in Figure 5.2) decelerate, increasing the time shift δ with respect to the reference wave. In this case, the back-sided crests travel in relatively shallower depths induced by the ILW trough. Conversely, the crests in the frontside (bottom half crests, 9 to 1) accelerate, decreasing the time shift δ with respect to the reference wave. In the latter case, front-sided crests travel on locally deeper areas around the ILW crest (red dots). These differences in individual wave celerity in shallow water caused by the variations in water depth, induced by long waves, have already been observed by Tissier et al. (2015). The intrawave variability of celerity can modify the wave-field considerably in shallow water inducing bore "focusing" or "merging" as illustrated by Sénéchal et al. (2011)

(i.e. faster bores overtake slower bores and focusing). Bore merging results in a concentration (focusing) of bores at the ILW crest (Figure 5.2). Figure 5.2 shows that intrawave variability in celerity is low before reaching shallow water. This suggests that most of the wave celerity differences are induced by the water depth variations caused by the long wave presence. This influence seems larger than any wave celerity variability induced by differences in wave height or amplitude-dispersion (Thornton & Guza, 1982). Further implications of bore merging will be discusses in Section 6.5.

5.3.3 Spatial distribution of the breakpoint

The same data treatment presented in Figure 5.1 to identify individual short wave breaking has been extended to all tested wave conditions (see Table 5.1). Both Table 5.1 and Figure 5.5 show the differences in the spatial distribution of the breaking mechanism for hf waves within a wave group. For wave conditions A and B, wave breaking occurred predominantly at intermediate water, while for wave conditions C wave breaking occurred at intermediate and shallow water. Figure 5.5 shows that, for a given f_p value, the breaking onset (x_{ob}) moves seaward as the group frequency decreases despite that the maximum wave height within the wave group at generation is highly similar (this was already suggested by Alsina et al. (2016)). The highest waves (at the center of the group) break in deeper water whereas the smallest ones (at the edges of the group) travel further into shallower water, widening

Table 5.1: Location where the waves forming the groups are shallow water waves (x_{ShWL}), breaking onset (x_{ob}) and breaking excursion (Δx_b) for *IBIMS-ILC* data set.

Case	x_{ShWL} (m)	x_{ob} (m)	Δx_b (m)
A-1	1.9	4.45	0.6
A-2	1.9	4.70	1.3
A-3	1.9	5.71	3.2
A-4	1.9	5.84	4.2
A-5	1.9	7.20	4.7
B-1	2.9	5.88	0.7
B-2	2.9	5.88	0.8
B-3	2.9	6.43	3.8
B-4	2.9	7.23	4.4
C-1	6.5	7.85	0.9
C-2	6.5	8.88	4.5
C-3	6.5	9.39	6.3

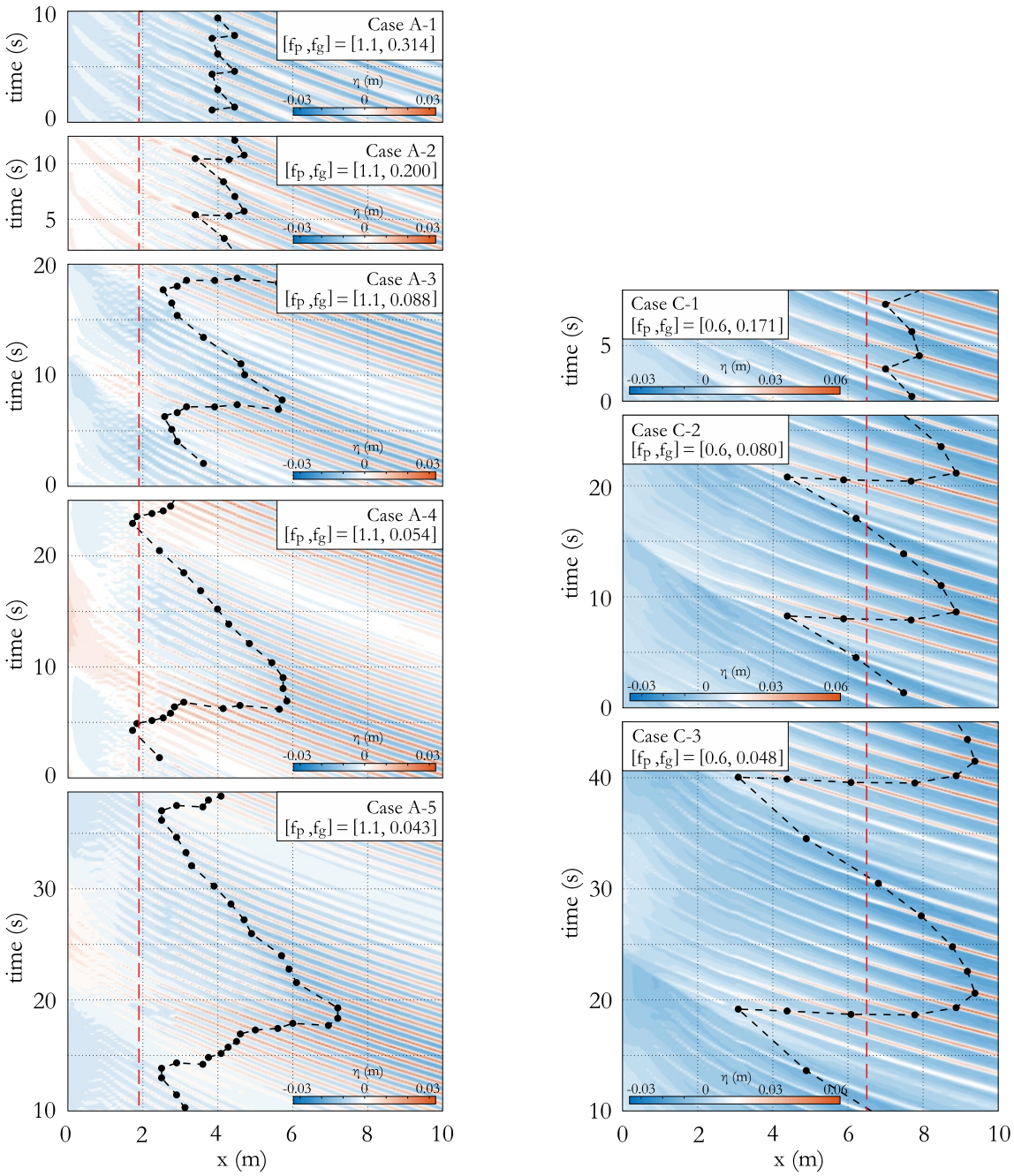

Figure 5.5: Space-time distribution of the varying breakpoint (black dashed line) for wave groups with $f_p = 1.1$ Hz (plots *a*, *b*, *c*, *d* and *e*) and $f_p = 0.6$ Hz (plots *f*, *g* and *h*). Black dots mark the locations of individual breaking events and the red dashed line indicates the shallow water limit x_{ShWL}.

the breaking excursion. This is also translated into longer breaking cycles T_b since the breaking time modulation is inversely related to the grouping frequency ($T_b = 1/f_g$). Therefore, with longer cycles and, consequently, higher number of constituent waves with the same mean period, the breakpoint excursion grows in time and space. For Series A, the breaking onset moves from $x = 4.45$m to $x = 7.20$m for $f_g = 0.314$Hz, and 0.043Hz respectively. For lower f_p-frequency wave conditions, Series C ($f_p = 0.6$Hz), the wave breaking starts at $x = 7.85$m for $f_g = 0.171$Hz and move seaward to $x = 9.39$m as the group frequency reduces to $f_g = 0.048$Hz. Although smaller waves may break in shallow water, all these breaking onsets occur always before reaching the shallow water limit x_{ShWL} associated with the mean primary frequency (red dashed lines in Figure 5.5).

5.3.4 Wave height reduction within the surf zone

The wave height distribution of individual waves with respect to the effective water depth h^* has been computed for all the tested wave conditions (Figure 5.6) and indicates that the wave-height to water-depth ratio ($\gamma = H/h^*$) describes the breaking sequence for every case remarkably well. The mean coefficient of determination R^2 is, in most of the tested cases, higher than 0.91 but with different γ values depending on f_p and group frequency. The influence of f_p on the wave breaking is well known, with larger γ values for longer individual wave crests (Bowen et al., 1968, Battjes, 1974, Alsina & Baldock, 2007). The distribution of the observed γ values with the Iribarren number or similarity surf parameter ξ is presented in Figure 5.7-a. There, the Iribarren number is computed close to the wave-maker as:

$$\xi_p = \frac{S}{\sqrt{H_s/L_p}}, \tag{5.4}$$

where S is the beach slope, L_p is the wavelength at the mean primary frequency (f_p) and H_s is the significant wave height computed from the standard deviation of the water surface signal. The γ-parameter is seen to increase for larger Iribarren numbers (Bowen et al., 1968, Battjes, 1974) (Figure 5.7-a, black dashed line). However, the scatter of the data is large, and for a given f_p value, it is also evident that there is an increase in the γ value as the group frequency increases. In other to retain the information of both influences, f_p and f_g, a modified Iribarren number is

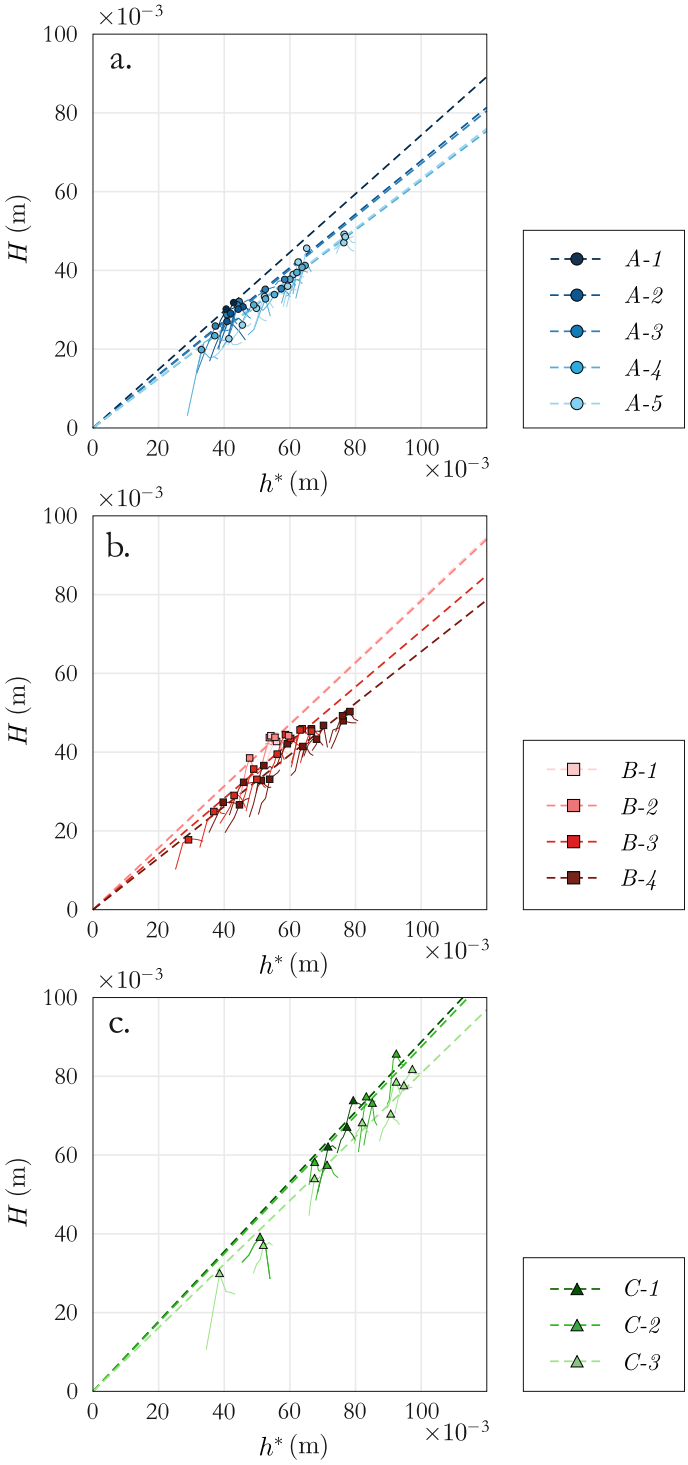

Figure 5.6: Wave-height of individual breaking crests against the effective water depth h^* for wave groups with $f_p = 1.1$Hz (a), $f_p = 0.9$Hz (b) and $f_p = 0.6$Hz (c). Dashed lines represent the best fit saturation line for each wave condition.

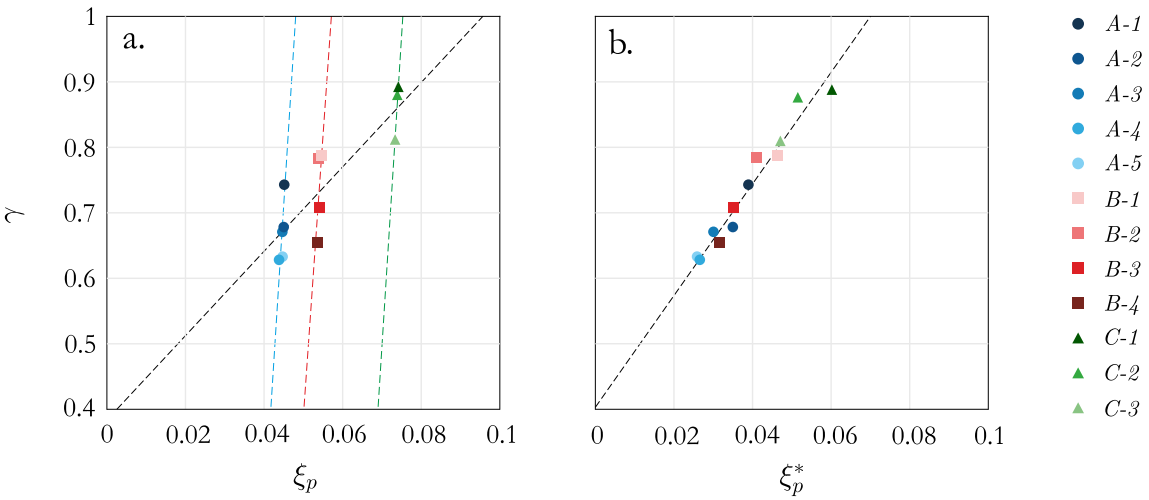

Figure 5.7: Wave-height to effective-depth ratio (γ) in terms of the Iribarren number ξ_p (a). The coloured dashed lines illustrate the influence of the group frequency (f_g) in contrast to the influence of the hf waves (black). Both trends collapse onto a single one considering a modified Iribarren number ξ_p^* accounting for the grouping structure (b).

proposed, including the wave group structure:

$$\xi_p^* = \xi_p \left(\frac{L_p}{L_g} \right)^{\kappa}, \tag{5.5}$$

where L_g is the length of the group and κ is an empirical parameter that may depend on the beach slope. For practical purposes, $L_g \approx c_{gp} \cdot T_g$, assuming the linear theory group velocity of the primary waves at the mean primary wave frequency c_{gp} as a good approach of the group celerity (this validation will be discussed later on in chapter 6). For a given value of $\kappa = 0.2$, the modified Iribarren number presented in Figure 5.7-*b* suggests a linear relationship $\gamma = 8.52 \cdot \xi_p^* + 0.4$, where wave conditions with a very different grouping structure (different grouping length and number of constituent crests), such as *B-1* and *C-3*, share a similar γ-value.

5.4 Wave-group transformations during shoreward propagation

During wave group propagation onto shallower water and before breaking, the geometry of the incident waves undergo substancial nonlinear transformations. In deep water, the short waves display a quasi-symmetrical shape. As these waves travel

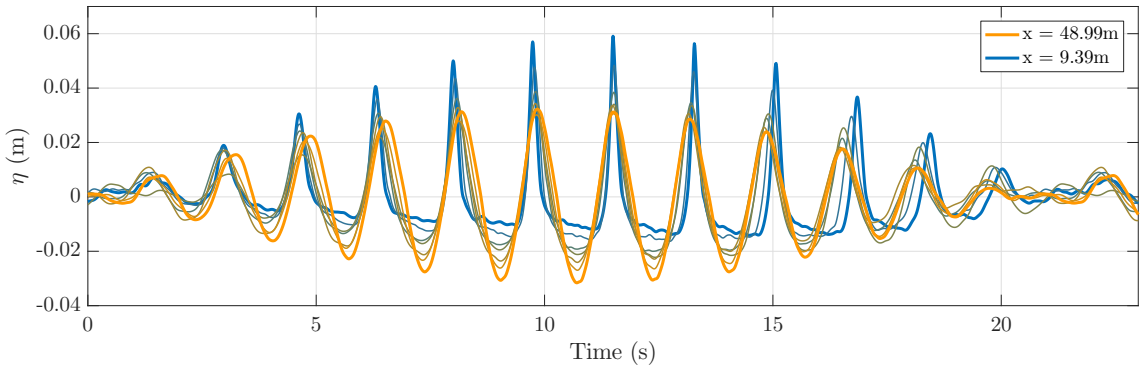

Figure 5.8: Time evolution of the a wave-group belonging to wave condition *C-3*. The evolution comprises the shoaling region only, from $x = 48.99$m (in the vicinities of the wave-maker) to $x = 9.39$m (at the breaking onset).

shoreward, they lose horizontal symmetry, becoming more skewed with shaper crests and flat broader troughs. Figure 5.8 shows the group evolution of case *C-3* during the short wave shoaling. The increase of horizontal asymmetry or skewness is clearly observed in the time series showed in Figure 5.8. Furthermore, the crests at the edges of the group tend to stretch the group. The crests at the front accelerate, whereas the ones at the back slow down. On top of that, the short waves forming the groups may lose their vertical symmetry too. This vertical asymmetry is identified as a pitching forward of the wave shape face, and for the present cases, it may be observed in certain crests within the surf zone (not shown).

These changes in the skewness and asymmetry of hf water surface elevations cannot be explained by linear theory. High order regular wave theories, as for example Stokes (1847), can predict the skewness of individual hf waves from the increasing contributions of superharmonics of the primary frequencies. However, high order Stokes-type wave theories do not explain the wave asymmetry because according to Stokes-type theories, the hf wave components remain phase-locked and in phase with the primary frequency. The pitching forward of the wave face represents a forward phase-shifting of the harmonics relative to the primary components (Elgar & Guza, 1986, Doering & Bowen, 1987, 1995).

During wave-group shoaling, these asymmetries progressively increase and eventually the short waves become unstable and break. The broken crests travel shoreward as bores dissipating the energy of the hf components and the remaining energy in the inner surf and swash zone is mainly driven by long waves (lf components).

5.4.1 Skewness and asymmetry of hf waves

Although the wave height to depth ratio, γ-parameter, describes the breaking process reasonably well, it does not offer a physical explanation of the wave group modulation (group frequency) influence on γ, or of the triggering of the wave breaking. Instead, the skewness (Sk) or the asymmetry (As) associated to η_{hf} has been traditionally used to describe the wave breaking onset because of the wave shape instability (Babanin et al., 2007).

Figure 5.9 shows the cross-shore distribution of the skewness and asymmetry computed through bispectral analysis (Equations 2.20 ans 2.21). Figure 5.9 shows an overall increase in absolute value of skewness, whereas the asymmetry remains low during wave propagation consistent with previous reported measurements (Doering & Bowen, 1987, 1995, Elgar & Guza, 1985, 1986). However, for a given f_p, a larger increase in skewness is observed as the group frequency decreases. At the same time, the onset of the asymmetry growth (in absolute value) is observed to move seaward as the group frequency decreases. A close relation between the maximum value in the cross-shore skewness distribution and the wave breaking onset is observed (Figure 5.9). During hf waves shoaling, the crest height grows larger than the trough depression, increasing wave skewness, and reaching a maximum ratio of around 1.5 before becoming unstable and breaking at x_{ob} (see Table 5.1). Trends in wave asymmetry and skewness are different for varying group frequencies, which suggests an influence of the group frequency on the nonlinear energy transfer from the primary components to superharmonics and subharmonics.

5.4.2 Hf waves phase versus primary waves phase

The celerity or phase velocity of a propagating wave is computed by tracking this wave using cross-correlation functions as explained in Appendix B. The empirical celerity ($\Delta x/\Delta\tau$) computed for any wave is presented in terms of the time ($\Delta\tau$) needed to travel between adjacent locations (Δx). Hence, $\tau = \sum \Delta\tau$ is the cumulative time for the waves to reach any location from X_0 (wave paddle).

Figure 5.10 (left-side plots) shows the cross-shore propagation time τ of the hf components [$2f_1$, $f_1 + f_2$, $2f_2$] compared to the primary components [f_1, $\eta_{[f1,f2]}$, f_2], respectively. Note that the wave crests forming the groups ideally propagate with the same celerity as free waves at f_p, although $f_p = (f_1 + f_2)/2$ is not an energetic

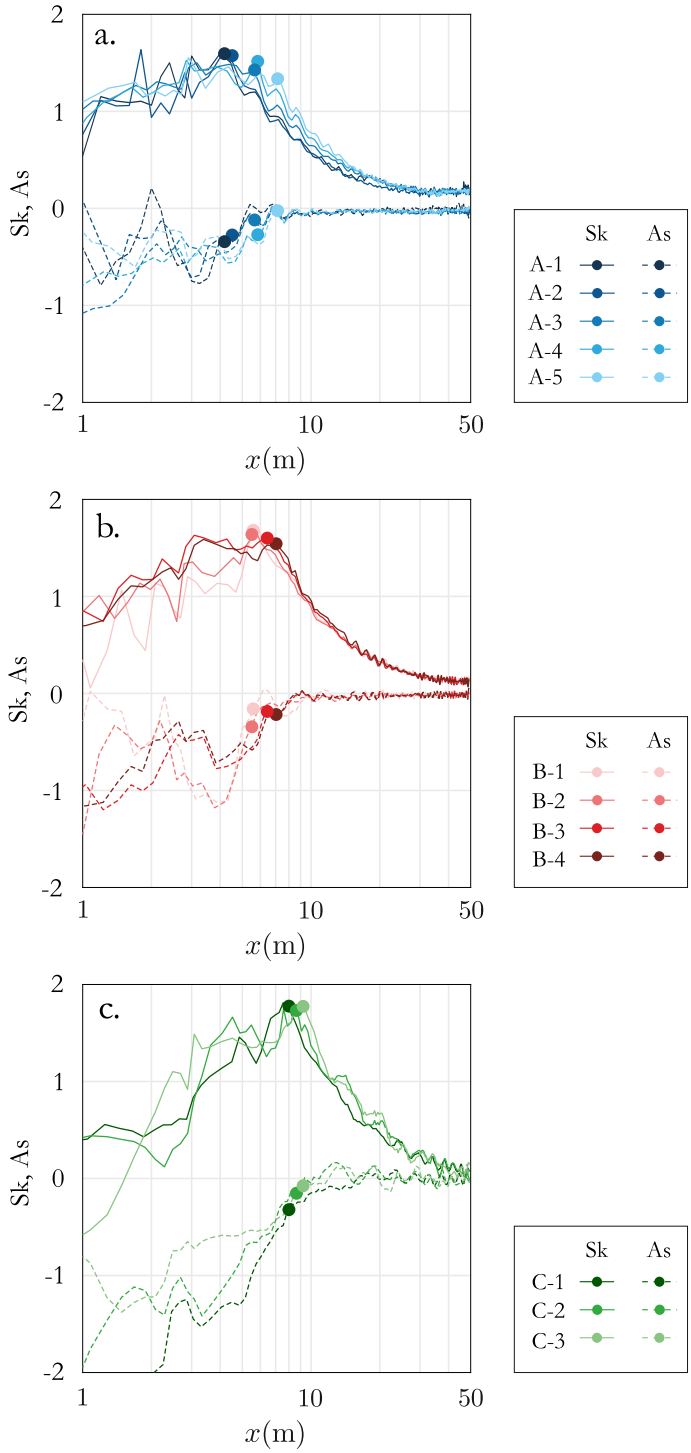

Figure 5.9: Cross-shore evolution of the hf wave skewness (solid line) and asymmetry (dashed line) for series A (a), B (b) and C (c). The breaking onsets are displayed with dots.

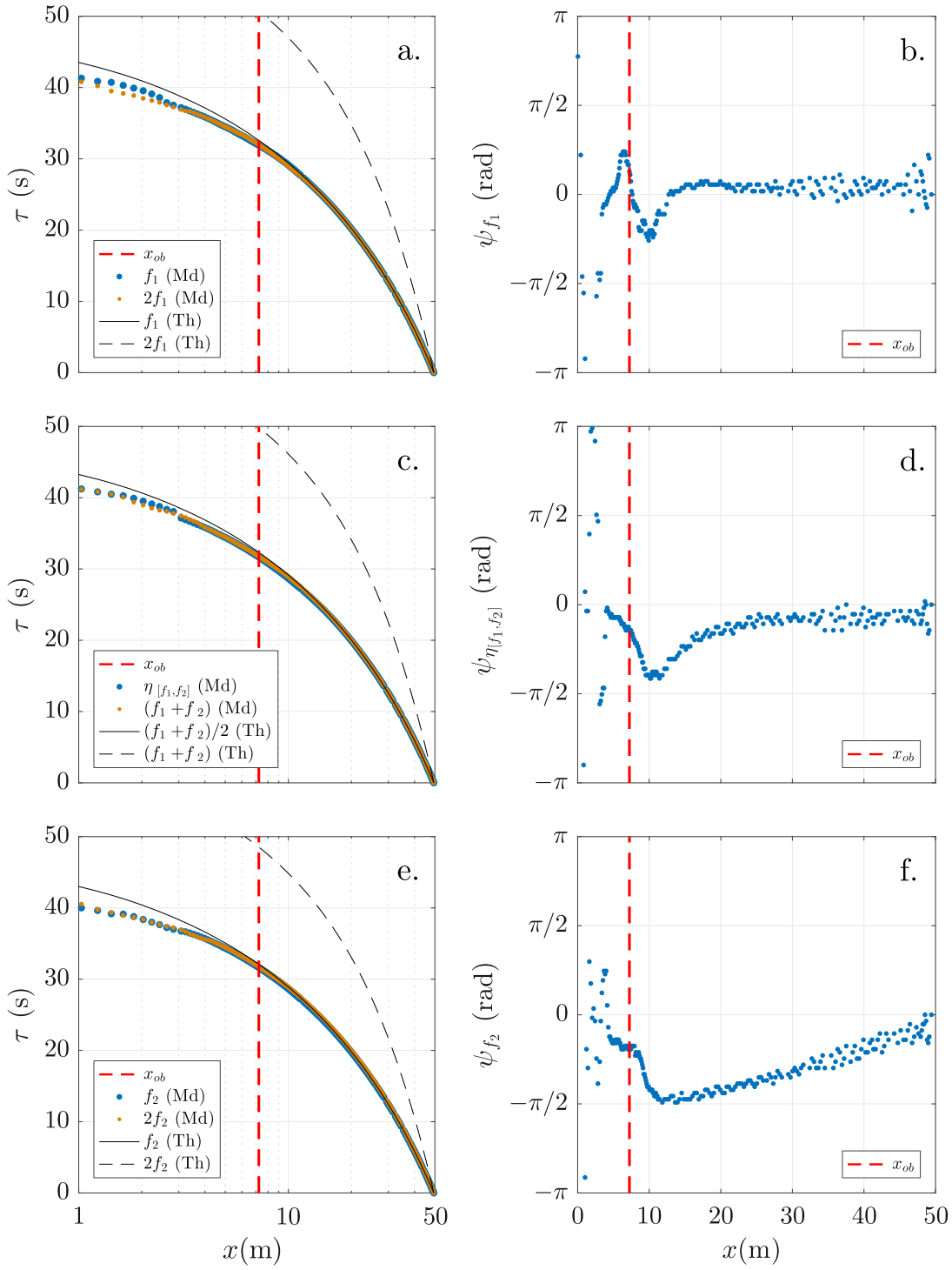

Figure 5.10: Left-side plots: Measured (Md) and theoretical (Th) cross-shore propagation time τ for $[f_1, 2f_1]$ (plot a), $[\eta_{[f1,f2]}, f_1 + f_2]$ (plot c) and $[f_2, 2f_2]$ (plot e). Right-side plots: Measured cross-shore phase difference between the pairs $[f_1, 2f_1]$ (plot b), $[\eta_{[f1,f2]}, f_1 + f_2]$ (plot d) and $[f_2, 2f_2]$ (plot f). The presented wave case is *B-4*, whose breaking onset x_{ob} is indicated by the red dashed line at $x = 7.23$m. Note that the x-coordinate system has its origin at the shoreline, where $x = 0$m. Left-side plots are in log-scale, whereas right-side plots perform linear-scale.

frequency component. Therefore, in order to be physically consistent, the wave crests forming the groups are noted as $\eta_{[f1,f2]}$ in Figure 5.10-*c* and -*d*. The phase velocity of $\eta_{[f1,f2]}$ is measured tracking the central crest of the group. The relatively good agreement observed in Figure 5.10 between the celerities for the pairs [f_1, $2f_1$] (plot *a*), [$\eta_{[f1,f2]}$, f_1+f_2] (plot *c*) and [f_2, $2f_2$] (plot *f*) during wave-group shoaling confirms the bound nature of the hf components. In Figure 5.10, the comparison between the measured (Md) celerities with theoretical (Th) ones (obtained using the Dispersion Equation) for f_1, f_p and f_2 reveals that the hf components in general undergo an acceleration after the breaking onset.

Figure 5.10 (right-side plots) shows the measured phase difference ψ between the pairs [f_1, $2f_1$] (plot *b*), [$\eta_{[f1,f2]}$, $f_1 + f_2$] (plot *d*) and [f_2, $2f_2$] (plot *f*). For instance, the phase difference between f_2 (Md) and $2f_2$ (Md) is obtained in terms of f_2 as $\psi_{f_2} = 2\pi\, f_2(\tau_{f_2} - \tau_{2f_2})$, and consequently, when $\psi_{f_2} < 0$ the wave component $2f_2$ lags behind f_2. Overall, ψ_{f_1}, $\psi_{\eta_{[f1,f2]}}$ and ψ_{f_2} are relatively low during wave group shoaling ($|\psi| < \pi/2$), in agreement with the low asymmetry shown in Figure 5.9, but enough to effectively induce nonlinear energy transfers from the primary frequencies to their superharmonics (this will be addressed below). In this context, $2f_1$ travels relatively in phase with f_1 until $x = 12$m approximately, where a relatively local phase-shift is observed (Figure 5.10-*b*). Conversely, the phase-shift undergone by $2f_2$ in Figure 5.10-*f* is progressive during the wave group shoaling and the largest within the superharmonics.

At the breaking onset, $2f_1$ locally moves ahead f_1, which is illustrated in Figure 5.10-*b* by a positive ψ_{f_1}. This is consistent with the fact that pitching forward in the wave shape usually occurs just before wave breaking. After the breaking onset, strong local phase-shifts are observed, which explain the sudden increase of the asymmetry from the breakpoint shoreward observed in Figure 5.9. Similar behaviour is observed for the rest of the wave conditions.

5.4.3 Nonlinear energy transfers to hf wave components

In Figures 5.11-*a* and -*c*, the water surface elevation where frequencies above f_1 have been filtered out ($\eta_{f<f_1}$) is compared with the total η at x_1 (vicinities of the wave paddle) for wave conditions belonging to *C-1* and *C-3*, respectively. The water surface elevation at x_1 is mainly explained by the primary components only since the differ-

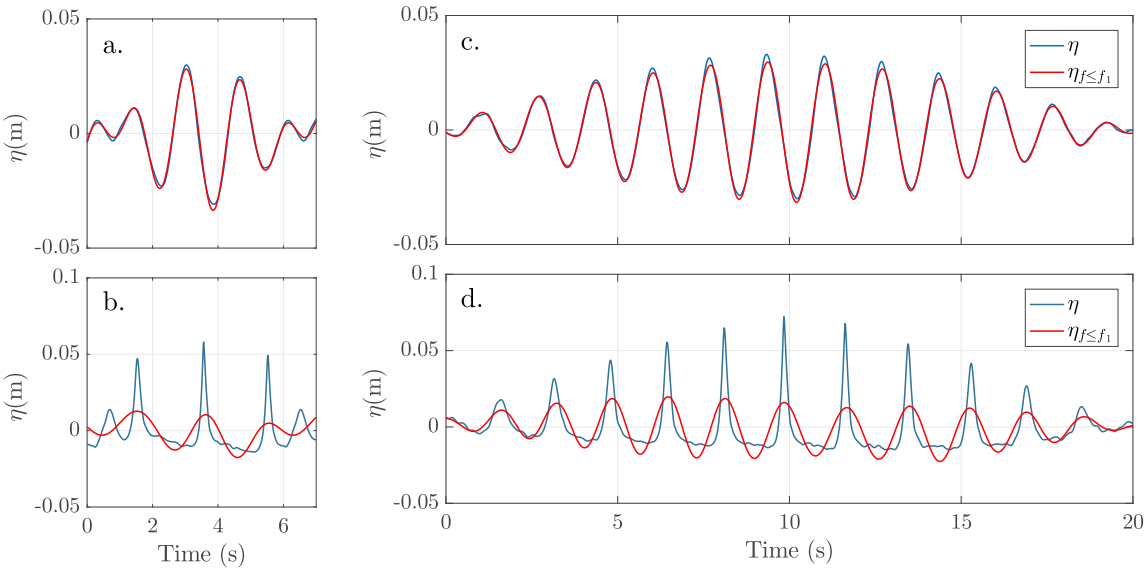

Figure 5.11: Water surface elevation time series η at x_1 (vicinities of the wave paddle) (plots *a* and *c*) and at x_{ob} (breaking onset) (plots *b* and *d*). The wave case *C-1* is illustrated in plots *a* and *b*, whereas the wave case *C-3* is illustrated in plots *c* and *d*. The water surface elevation where frequencies above f_1 have been filtered out is $\eta_{f<f_1}$.

ences between η and $\eta_{f<f_1}$ in both wave conditions are rather small. Consequently, the energy content of the superharmonics at x_1 is negligible and the Skewness and Asymmetry are relatively low as observed in Figure 5.9. In contrast, at the breaking onset (Figures 5.11-*b* and -*d*), the larger differences between η and $\eta_{f<f_1}$ indicate that the primary frequencies are unable to explain the sharper crests and flatter troughs without the contribution of their superharmonics (whose energy content has importantly grown). The progressive contribution of the arising hf components to the loss of horizontal symmetry is clear in Figure 5.11.

The growth of the hf wave components is due to nonlinear wave-wave interactions of the primary waves. Consequently, nonlinear energy transfers between harmonics will be examined using a higher-order spectral technique accounting for triad interactions (see section 2.3.4). In particular, bispectral analysis of the surface elevation is performed using time series resampled to 10Hz with a frequency resolution of 0.001Hz.

Figures 5.12 and 5.13 illustrate the spatial evolution of the high frequency components for wave conditions *C-1* ($[f_1,f_2]$ = [0.686 Hz, 0.514 Hz]) and *C-3* ($[f_1,f_2]$ = [0.624 Hz, 0.576 Hz]), respectively. Similar behaviour was observed for series *A* and *B* but series *C* show more energetic frequency components which helped to better ex-

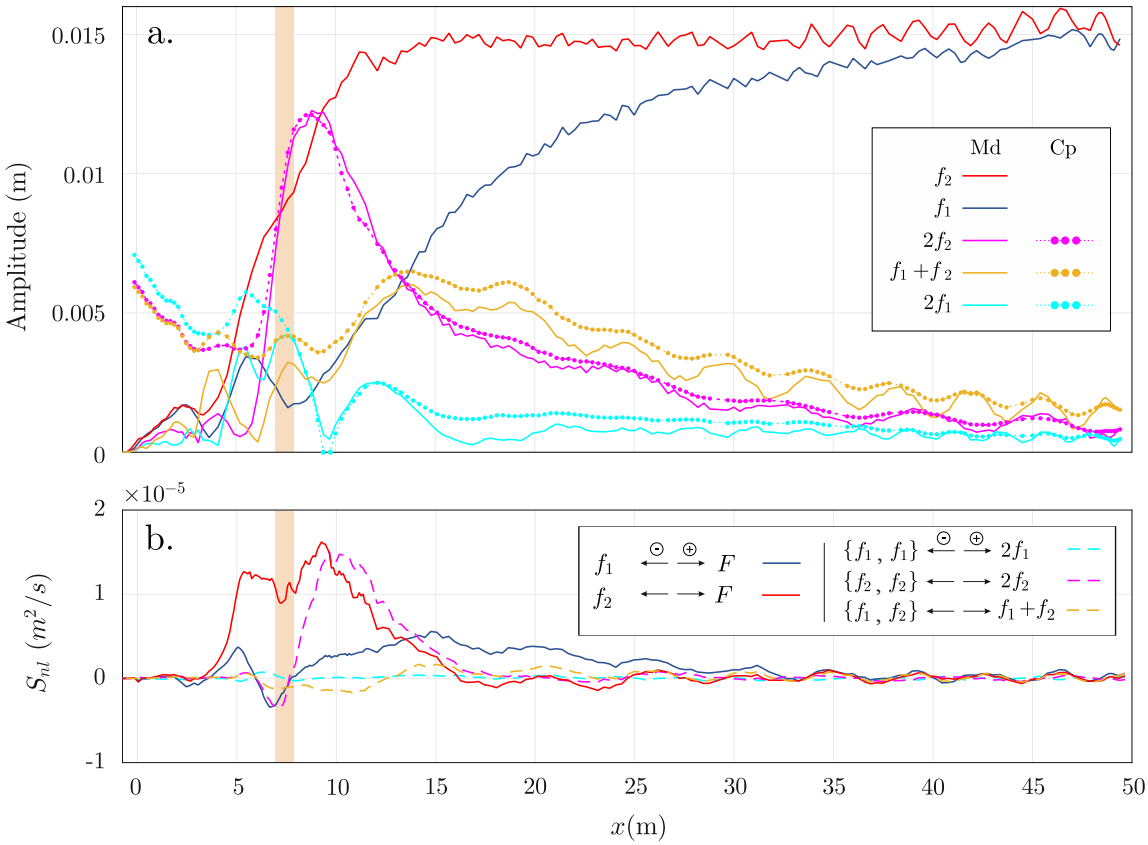

FIGURE 5.12: Plot *a* shows the measured (Md) and computed (Cp) cross-shore amplitude evolution of the primary components (f_1, f_2) and their superharmonics ($2f_1$, f_1+f_2, $2f_2$) for the wave condition *C-1*. Plot *b* shows the energy flux gradient (S_{nl}) for certain energy exchanges involving f_1 and f_2. The shaded area indicates the breaking excursion Δx_b.

plain the observed behaviour. Plot *a* (Figures 5.12 and 5.13) illustrates the measured (Md) and computed (Cp) cross-shore amplitude evolution of the hf wave components $2f_1$, $2f_2$ and f_1+f_2, comparing them to the measured evolution of the primary components f_1 and f_2. The computed cross-shore amplitude evolution is based on the high order spectral analysis described in Section 2.3.4 (Equations (2.23)-(2.26)). The dissipation term in Equation (2.25) is assumed negligible ($H_{ds,f} \approx 0$).

Overall, the hf wave components $2f_1$, $2f_2$ and f_1+f_2 are well explained in terms of nonlinear triad-interaction energy exchanges until the wave breaking onset. For the wave condition with the larger group frequency (*C-1*), Figure 5.12-*a* shows that the higher growth is achieved by $2f_2$, due to the self-self interactions of f_2 ($\{f_2, f_2\} \rightarrow 2f_2$), whose maximum is reached just before the wave breaking onset. At the same time, the energy budget associated with $2f_1$ remains remarkably low compared to $2f_2$, whereas the sum term f_1+f_2 reaches its maximum amplitude

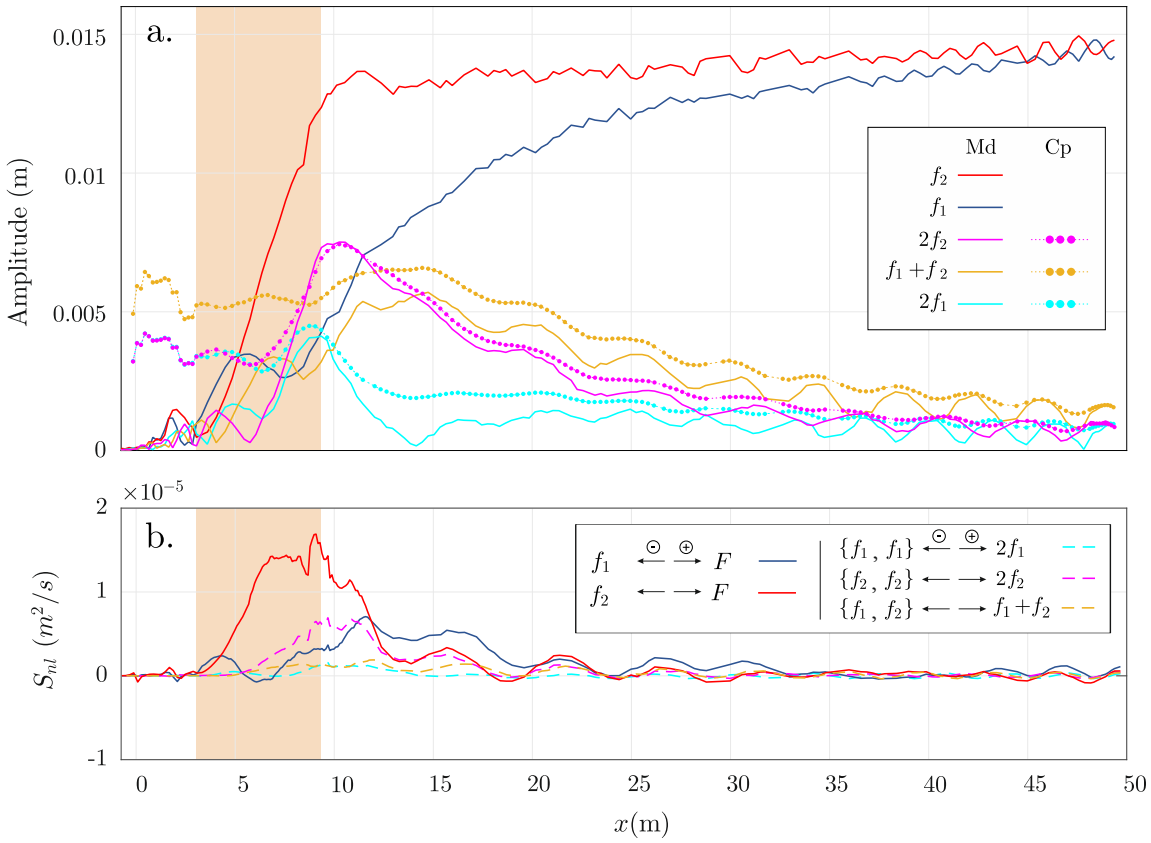

Figure 5.13: Plot a shows the measured (Md) and computed (Cp) cross-shore amplitude evolution of the primary components (f_1, f_2) and their superharmonics ($2f_1$, f_1+f_2, $2f_2$) for the wave condition *C-3*. Plot b shows the energy flux gradient (S_{nl}) for certain energy exchanges involving f_1 and f_2. The shaded area indicates the breaking excursion Δx_b.

far outside the surf zone. In contrast, the wave condition *C-3*, illustrated in Figure 5.13-*a*, is characterized by a lower group frequency (longer wave groups). In this case, the component $2f_2$ is again the more energetic superharmonic, but its energy content is noticeably lower than in *C-1*, as observed at $x = 10$m for both cases. There are small differences in the growth of the $f_1 + f_2$ component which presents a maximum close to the surf zone, whereas $2f_1$ is again the weakest superharmonic despite its slightly larger growth observed in Figure 5.13-*a*. Note that the overall cross-shore amplitude of these superharmonics is in agreement with the phase-shift observed in Figure 5.10. The larger progressive growth undergone by $2f_2$ is explained by the progressive dominant phase-shift ψ_{f_2}, whereas the relatively low ψ_{f_1} explains the weak amplitude growth observed for $2f_1$.

Figure 5.12-*b* and 5.13-*b* illustrate certain energy flux gradients involving f_1 and f_2 for the wave conditions *C-1* and *C-3*, respectively. In those Figures, the legend should

be understood as follows: the arrow indicates in which direction the energy transfer occurs according to the sign of the flux gradient S_{nl}. For instance, the solid red line, when positive, indicates a net energy transfer from f_2 to F, where F represents all the possible triad where f_2 may be involved. In general, the decreasing energy content of f_1 and f_2 during wave-group shoaling is confirmed by Figures 5.12-*b* and 5.13-*b*, where $f_1 \rightarrow F$ and $f_2 \rightarrow F$ prevail during shoreward propagation. However, f_1 undergoes a progressive and moderate net energy transfer from the wave paddle until some meters before the breaking onset (x = 15m in Figure 5.12-*b*), whereas f_2 undergoes a more intense and concentrated energy transfer in shallower depths (from x = 15m onwards in Figure 5.12-*b*). Similar net exchange from f_1 and f_2 is seen for the wave condition *C-3* (Figure 5.13-*b*), but the particular transfers to their superharmonics $2f_1$ and $2f_2$ are different. For wave condition *C-1* (Figure 5.12-*b*), the exchange $\{f_2,\ f_2\} \rightarrow 2f_2$ comprises most of the energy transfers from f_2 before breaking ($\{f_2,\ f_2\} \rightarrow 2f_2$ and $f_2 \rightarrow F$ are practically coincident before breaking) confirming the larger growth of $2f_2$ seen in plot *a*. In contrast, the energy transfer from f_2 to $2f_2$ is smaller in the wave condition *C-3* (Figure 5.13) confirming the smaller growth of $2f_2$ before breaking in Figure 5.13-*a*. Moreover, in both cases, the energy transfer from f_1 to $2f_1$ and $f_1 + f_2$ are practically negligible compared to the general transfer from f_1 ($f_1 \rightarrow$ F). This suggests that most of the energy transfers from f_1 might not be oriented to hf wave components, but to lf components instead (this will be investigated in chapter 6).

5.5 Discussion

The shoreward propagation of bichromatic wave groups with different group frequencies ($f_g = f_1 - f_2$) and mean primary frequencies ($f_p = (f_1 + f_2)/2$) is investigated. During shoreward propagation of these wave groups, the group shape progressively undergoes important transformations, usually related to the growth of hf wave components (Guza & Thornton, 1982, Elgar & Guza, 1985) and confirmed by a net energy exchange from the primary waves to their superharmonics ($2f_1$, $2f_2$ and f_1+f_2). The study of the energy fluxes to the superharmonics suggests that f_2 mainly contributes to the growth of $2f_2$ until few meters before the breaking onset where the energy transfer from f_2 switches to lf components. In contrast, the energy transfers from f_1

to $2f_1$ and $f_1 + f_2$ are negligible and the contribution of f_1 is in general more oriented to lf wave components. Moreover, the wave groups with low group frequency experience a smaller dissipation of the primary frequency components, in particular f_1, compared to wave groups with high group frequency. This trend, a reduced decay of f_1 for decreasing group frequency, has already been reported by previous authors (Baldock et al., 2000, Alsina et al., 2016) and may only be attributed to a larger energy transfer from f_1 to f_g for wave conditions with high group frequency. This result will be confirmed in chapter 6 where the energy transfers to lf wave components are investigated. In particular, a more energetic exchange $f_1 \rightarrow \{f_g, f_2\}$ will be confirmed for the wave condition *C-1*, explaining the larger amplitude decay observed at f_1 in those wave conditions.

As the wave groups travel to shallower depths, the increasing number of energetic hf components leads to sharper crests and shallower, flatter and broader troughs. For the presented wave-groups propagating on a mild slope, the horizontal wave asymmetry (skewness) is in general more relevant during shoaling, whereas the loss of vertical wave symmetry is secondary. From a physical point of view, the growth of hf components during shoreward propagation makes the skewness to progressively grow until the crests forming the groups become unstable and a spilling-type breaking occurs ($\xi_p < 0.1$). The breaking onset is, consequently, expected to happen where a certain limiting level of skewness is reached. This seems to be the opposite to what happens in steeper slopes where a plunging-type breaking typically occurs. In steeper sloping beds, skewness usually turns secondary with a more important influence of the vertical asymmetries (Elgar & Guza, 1985). Due to the high spatial resolution of the present data, the individual crests forming the groups are tracked as they shoal and their breaking events, accurately identified (Figure 5.1). The sequence of breaking events defines a moving breakpoint whose breaking onset is observed to occur when skewness overall reaches 1.5. In comparison, the limiting skewness level for breaking ocean waves is generally set to 1 (Babanin et al., 2007). Grouping waves whose skewness grows with mild reducing water depths seem to tolerate up to 50% more skewness before breaking. Although skewness seems to explain reasonably well the breaking process, a local measure of the steepness of each crest would be a desired quantity, but impractical for the present experimental setup.

Although a larger skewness growth is been observed for the wave condition *C-3*,

compared to *C-1*, a larger growth of the dominant superharmonic component $2f_2$ is present for the wave case *C-1*. Therefore, it is difficult to assess which frequency component contributes more to the wave skewness since the wave shape is the result of the contribution of all the harmonics and superharmonics. Nevertheless, the influence of the wave group modulation in hf wave skewness and eventual breaking is clear from the present experiments. A noticeable tendency of low group frequency wave conditions to promote a larger growth in the wave skewness has been observed (Figure 5.9), whose immediate consequence is an earlier breaking onset (Figure 5.5). This is in agreement with Elgar & Guza (1985), where an important reduction of the skewness and asymmetry is observed when the energy transfers to lf components are strong. For increasing wave group frequencies, a larger nonlinear energy transfer from f_1 to f_g has been suggested. This results in a larger dissipation of the primary components and a reduction of the high frequency energy budget with consequences in the hf waves asymmetry. Previous studies (Battjes et al. (2004), among others) consider that the nonlinear energy transfer to subharmonics have little influence on the primary waves energy budget but the present study shows that this is not the case. The wave group frequency influence in the hf wave asymmetry is, therefore, due to two processes, both associated to nonlinear energy transfers: one is the increasing growth of superharmonics for reducing wave group frequency and the second process is the reduction of primary components due to energy transfer to subharmonics.

The influence of the wave group modulation in wave skewness and breaking has important implications in coastal morphology as shown in Alsina et al. (2016). There, long wave groups (low group frequency) induced earlier wave breaking and a breaker bar located at further seaward locations. The presented results are consistent with previous analysis of random wave conditions (Norheim et al., 1998, Rocha et al., 2017) showing an increase in hf wave asymmetry when the spectral bandwidth is narrowed (which leads to longer wave groups). Norheim et al. (1998) attributed this to the fact that sum and difference interactions tend to cancel in broad spectrum conditions. As suggested by Baldock (2012) and Alsina et al. (2016), there seems to exist a link between hf and lf energy. The group frequency controls the group modulation and the nonlinear energy transfer to superharmonics that contributes to the wave asymmetry.

For the present studies, the breaking onset of individual waves correlates well

with a constant wave height to depth ratio, γ, when the water depth is corrected with the long wave amplitude. A modification of the Iribarren number, Equation (5.5), is proposed to account for the influence of the wave group modulation on the hf wave breaking parameter γ. However, the applicability of Equation (5.5) to random wave conditions where wave group modulation occurs over a wide range of group periods requires further investigation.

5.6 Concluding remarks

New laboratory data on bichromatic wave groups propagating on a 1:100 sloping bed have been presented (*IBIMS-ILC* data set, section 3.3). A quasi-continuous evolution of the wave groups during shoreward propagation is showed, with special attention to their nonlinear transformations and eventual breaking of the crests forming the groups.

The individual wave tracking has shown a varying breakpoint location oscillating with the wave group frequency and whose amplitude affects the surf zone width. Longer wave groups (lower group frequency) have shown a longer breakpoint excursion and their breaking onsets move seaward compared to the shorter wave groups. This is explained by progressive losses of horizontal and vertical symmetry (skewness and asymmetry, respectively) of the wave groups during shoaling. Both quantities are controlled by the primary wave frequency difference, i.e., the wave group frequency. However, the influence of the group frequency in the wave skewness seems to be crucial on mild slopes, since the breaking onset is observed to occur when a limiting skewness level ($Sk \approx 1.5$) is reached.

The hf wave-height reduction within the surf zone is very well described by the wave-height to water-depth ratio (γ). The influence of the group frequency in the hf wave breaking is also highlighted in the γ-parameter, which is shown to increase with the group frequency. The γ-parameter is shown to describe the breaking sequence remarkably well ($R^2 > 0.91$), where individual breaking events are highly influenced by water-depth variations promoted by the existence of lf components in near-shore areas. Traditional models estimate γ using the Iribarren number ξ, which does not account for variations in the group frequency. Therefore, a modification to the Iribarren number has been proposed in this work (Equation 5.5), since the location and

width of the moving breakpoint depends not just on hf components, but importantly on lf waves as well.

From this chapter, we conclude the existence of a strong link between the group frequency (which might be extended to bandwidth in random waves) and the growth of lf and hf components while shoaling, with important implications on the wave breaking process.

6

Influence of the group modulation on long wave propagation on a mild slope

Author's Note: The results of this chapter have been partially published in Padilla & Alsina (2017).

6.1 Chapter overview

This chapter describes the influence of the wave group modulation on low frequency (lf) wave components. To do so, different bichromatic wave conditions with the same energy content but different group frequency (the length of the group is different) are analysed.

This chapter begins with the analysis of the celerities of different lf wave motions propagating shoreward, e.g., the incoming long waves. At the group frequency, the ILW amplitude growth during wave-group shoaling is explained in terms of the increasing phase-lag between the ILW and the hf wave envelope, where the influence of the group modulation, i.e., the group frequency, is clear. Subsequently, the growth of the lf wave components is explained as a consequence of nonlinear energy transfers from the primary frequencies. Using bispectral analysis, the specific exchanges between the primary wave components (at f_1 and f_2) and the main lf wave components

(at f_g and $2f_g$) are studied. Finally, as the use of a mild slope causes energy dissipation of most of the hf wave components due to wave breaking, the dominance and the energy content of lf components in the inner surf and swash zones is discussed.

6.2 Introduction

The long wave generation mechanism proposed by Biésel (1952) and (Longuet-Higgins & Stewart, 1962, 1964) considers the generation of long wave motions by the nonlinear interaction of pairs of primary components. They proposed a steady state equilibrium solution where the resulting second-order long wave travel bounded to the incident group and in antiphase with the swell envelope. The formulation of this equilibrium solution over a flat bed is presented in Appendix A, where Equation A.8 represents the amplitude of the resulting group-bound ILW (A^{ILW}). Moreover, the relative phase between the ILW and the swell envelope remains constant as $\psi = \pi$ rad.

During wave-group shoaling, the ILW has been observed to lag behind the group with an additional phase shift $\Delta\psi$ (List (1992), Van Dongeren & Svendsen (1997), Janssen et al. (2003) and Battjes et al. (2004), among many others). Janssen et al. (2003) theoretically explained that this phase lag allows energy transfers from the primary waves to lf components, i.e. the ILW among others. Although, there is no analytical solution for the evolution of the group-bound ILW over changing depths, Battjes et al. (2004) and Van Dongeren et al. (2007) showed that a function of the local depth in the way: $A^{ILW} \sim h^{-\alpha}$ may be a good descriptor of the ILW amplitude growth. Battjes et al. (2004) discussed that α is limited by [1/4, 5/2] which are the corresponding α-values to the Green's law and the extension of the equilibrium solution over an sloping bottom, respectively.

For a given beach slope, Battjes et al. (2004) showed that the phase lag appears to increase with increasing frequency as well as the ILW amplitude does. This observed frequency dependence has been generalized as a function of the normalized bed slope parameter β (Equation 2.16), that identifies whether a *mild-slope* or a *steep-slope* regime prevails. In Equation 2.16, h is usually taken as the water depth at the mean breaking location h_b (β_b for this case). Alternatively, h may be replaced by the incident wave height H. In that case, β_H (Equation 2.30) accounts for the

relationship between the beach slope and the steepness of the wave. According to these definitions, β_b is a dimensionless parameter closely related to the normalized surf zone width χ defined by Symonds et al. (1982), whereas β_H defined in deep water is proportional to the similarity surf parameter (Iribarren number). Battjes et al. (2004) found that for low values of β (they suggest $\beta_b < 0.1$), a mild-slope regime exists where the ILW amplitude growth in the shoaling zone is large compared to the steep-slope regime ($\beta_b > 0.45$).

Close to the wave breaking location, when the hf waves are in shallow water, bound lf waves can also be progressively "released" from the hf wave groups since these non-dispersive conditions correspond to those where the forced long wave satisfies the free wave dispersion relationship (Baldock & Huntley, 2002, Baldock, 2012). This is consistent with field data analysis (Elgar et al., 1992, Herbers et al., 1995) showing that as hf waves shoal, before hf wave breaking, the relationship between lf and hf waves changes from one corresponding to a group-bound ILW in deep water to freely propagating ILW in shallow water as the difference interaction between primary components becomes close to resonant.

Baldock (2012) has suggested that the ILW is released before or at the breakpoint if the hf waves are shallow water waves. Conversely, if the hf waves are not shallow water waves at the breakpoint, the ILW may reduce in amplitude along with the reduction in the primary wave forcing after breaking (Baldock & Huntley, 2002, Baldock, 2012). A number of experimental and field data sets suggest that the ILWs follow strong near-shore dissipation after wave group breaking (Baldock et al., 2000, Battjes et al., 2004, Henderson et al., 2006, Baldock, 2012). Near-shore lf wave dissipation has been suggested to occur through nonlinear interaction that transfer energy from the lf wave components back to hf wave components and it is not generally attributed to frictional losses (Henderson & Bowen, 2002, Henderson et al., 2006).

For some lf components and beach slope combinations resulting in small values of the dimensionless normalized bed slope parameter β, the near-shore dissipation of lf waves is attributed to long wave breaking (Battjes et al., 2004, Van Dongeren et al., 2007, De Bakker et al., 2014) suggesting lf energy saturation at the shoreline. Battjes et al. (2004) found that for small values of β (mild-slope regime) lf reflection at the shoreline was small. They suggested that the observed lf energy losses are due to

long wave breaking. Laboratory data have confirmed that with decreasing depth the lf wave self-self interaction may dominate energy transfer causing the lf wave front to steepen up and eventually break (Van Dongeren et al., 2007). This seems consistent with field measurements of run-up elevation (Ruessink et al., 1998a, Sénéchal et al., 2011, Guedes et al., 2013) showing run-up energy saturation at lf domain during highly dissipative energetic storms.

6.2.1 Experimental data

The experiments used in this chapter belong to *IBIMS-ILC* data set, whose wave conditions design, measuring process and signal post-processing can be found in section 3.3. These experiments were carried out in the Wave Evolution Flume at Imperial College London. The description of the facilities, instrumentation and experimental setup can be found in section 3.2.

These are 12 bichromatic wave cases where fully-modulated identical wave groups propagate shoreward on a 1:100 sloping bed. Table 3.1 summarises the information about the wave conditions used in this chapter.

6.3 Celerity of propagating long waves

The phase celerity between different wave components (hf wave envelope and lf waves) have been computed using cross-correlation functions as explained in Appendix B. This correlation technique is applied to various combination of signals and therefore the notation of the correlation function varies depending of the pair of signals used. For instance, $R_{ILW,ILW}$ denotes the correlation function performed between pairs of ILWs measured at different cross-shore locations. The empirical celerity ($\Delta x/\Delta\tau$) is presented in terms of the time ($\Delta\tau$) needed to travel between adjacent locations (Δx) and $\tau = \sum \Delta\tau$ is the cumulative time for the waves to reach any location from the wave paddle. Figure 6.1 presents the obtained τ for wave conditions A-4 (left-side plots a to c), whereas the right-side plots d to f correspond to the wave condition *A-2*.

The short waves envelope provides the shape of the wave-group structure and it

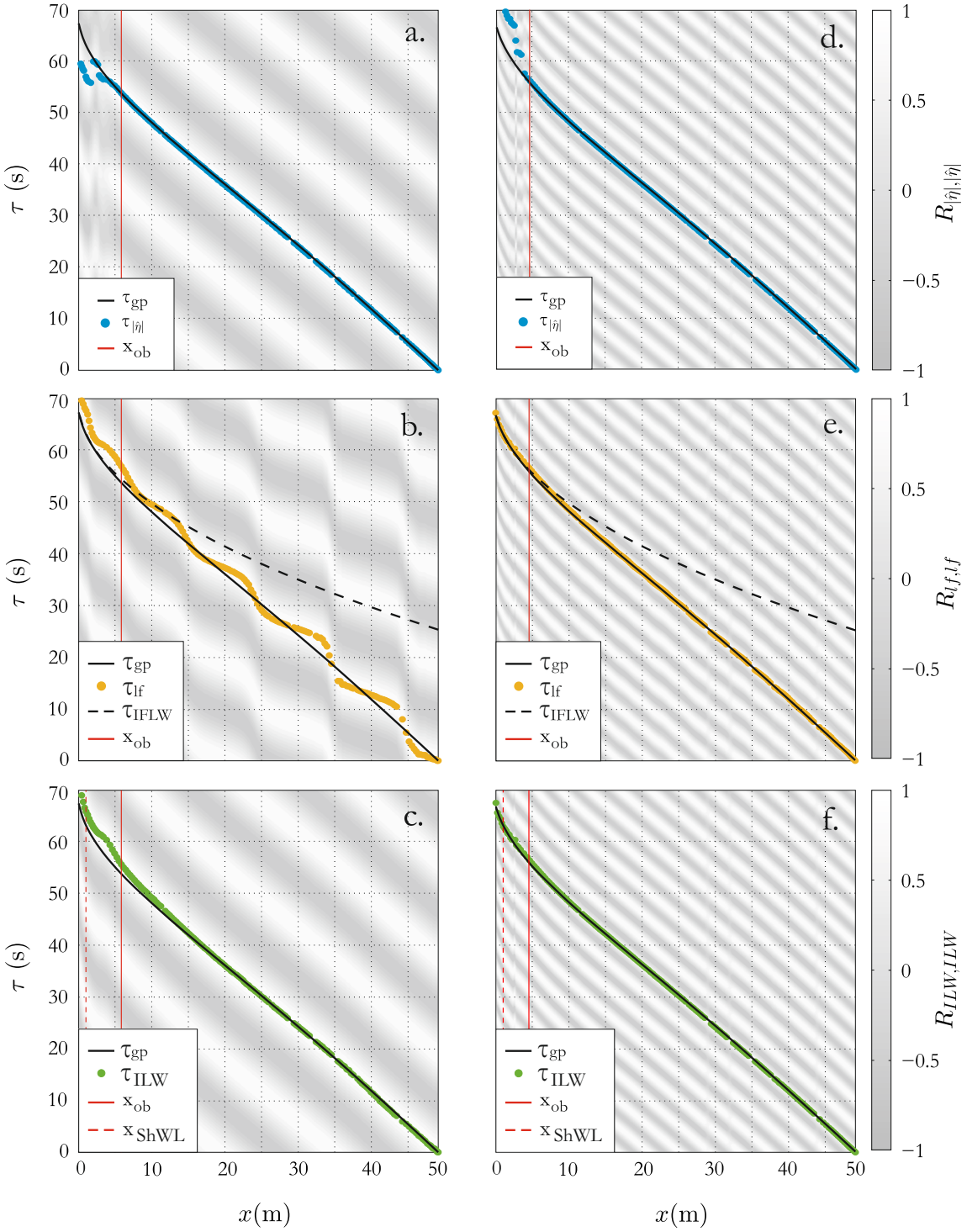

Figure 6.1: Case *A-4* is represented in the left-side plots (*a-c*), whereas case *A-2*, in the right-side plots (*d-f*). Plots *a* and *d* correlate the short-wave envelopes, such that the gradient of the blue circles is the celerity of the wave groups. Plots *b* and *e* correlate η_{lf}, and plots *c* and *f* correlate the separated ILW. The breaking onset (x_{ob}) and the shallow water limit for the mean primary frequency (x_{ShWL}) are also illustrated.

is obtained through Hilbert transformation as

$$|\hat{\eta}| = |\eta_{hf}(t) + i\Gamma(\eta_{hf})|_{lf}, \tag{6.1}$$

where $\Gamma(\ \cdot\ )$ denotes the Hilbert transform operator and the subscript are the high- (hf) or low-pass (lf) filter applied to the water surface elevation signal η. The propagation time of the envelope ($\tau_{|\hat{\eta}|}$) is presented in panels *a* and *d* for cases *A-4* and *A-2*, respectively. Panels *a-b* also include τ_{gp}, which is the theoretical cumulative time for a wave travelling with the celerity c_{gp} (Equation (2.9)). In both cases, τ_{gp} matches $\tau_{|\hat{\eta}|}$ remarkably well even in the vicinity of the breaking onset, where a higher mismatch due to cumulative errors should be expected. This match validates the use of c_{gp} (Equation (2.9)) as a good approach for the hf wave group celerity. Actually, c_{gp} will be used hereafter as the reference for the grouping structure propagation celerity. Note that at a certain location within the surf zone, the grouping structure disappears due to the breaking sequence of individual crests and tracking the wave group envelope becomes difficult.

Panels *b* and *e* present the motion of the total lf waves (low-pass filtered water surface elevation at wave group frequencies and subharmonics), whereas panels *c* and *f* only accounts for the ILW separated using the array method as explained in section 4.4.1. The case *A-4* illustrated in panel *b*, shows the typical behaviour for a quasi-standing wave with a dominance of the ILW over the reflected one. Conversely, case *A-2* exhibits a much weaker long wave reflection in panel *e*, where no standing pattern is identified. For this later case, panels *e* and *f* result in a similar pattern which implies that the lf domain is almost entirely composed by ILW energy. A growing propagation time-lag is observed between the τ_{ILW} and τ_{gp}, where the ILW lags behind the groups as they propagate to shallow water conditions. This time lag, which is more noticeable in panel *c* than *f*, is in time units and does not reflect the relative phase shift ψ between the groups and the ILW.

6.3.1 Relative phase between the ILW and the wave group

The growing propagation time-lag observed in Figure 6.1-c between τ_{ILW} (the cumulative propagation time of the ILW), and τ_{gp} (the theoretical propagation time associated with the group structure) implies that the ILW lags behind the groups as

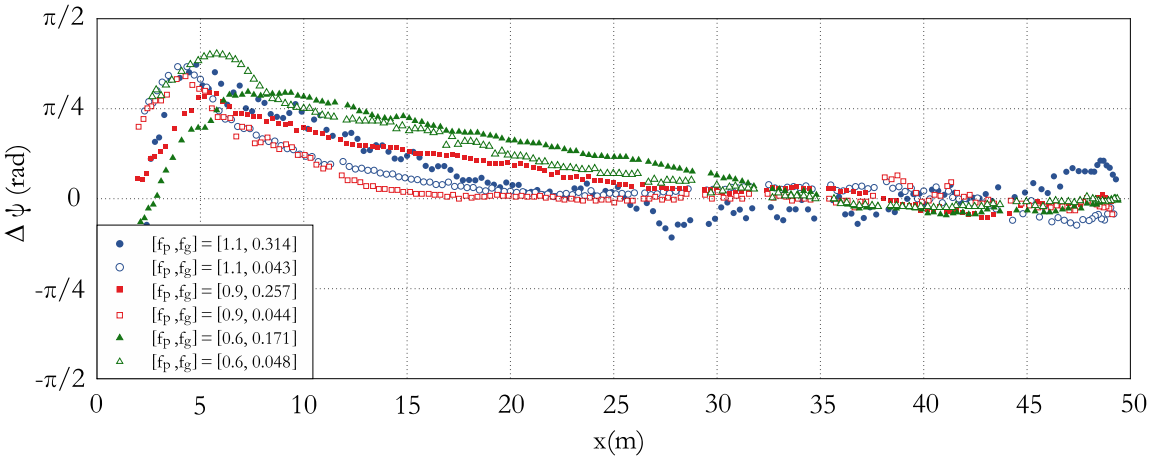

Figure 6.2: Additional phase shift $\Delta\psi$ between the group structure and the ILW, above the expected π-shifted phase typical from the equilibrium solution. ILWs lag behind the groups for positive values of $\Delta\psi$. The present cases show the longest and shortest groups for series A (blue circles), B (red squares) and C (green triangles).

they propagate to shallower water. The relative phase shift ψ between ILW and the wave group structure is obtained as $\psi = \pi + 2\pi f_g(\tau_{ILW} - \tau_{gp})$, and the additional phase shift with respect to the theoretical π value as $\Delta\psi = \psi - \pi$. Figure 6.2 shows the cross-shore variation of the additional phase shift $\Delta\psi$ for different wave conditions. Close to the wavemaker, where an equilibrium situation is expected, $\psi \approx \pi$ which means that the ILW and the group structure are in antiphase. During wave group shoaling, ψ separates from π strongly as the group frequency decreases. After hf wave breaking and when approaching shallow water depths, the additional phase shift decays. This may be due to nonlinearities in this region which also affect the separation method.

Figure 6.2 shows that for a given f_p, the phase lag between the wave group envelop and the ILW increases as the group frequency increases. Only the higher and lower f_g for each wave series are illustrated in Figure 6.2, where open symbols denote the lower f_g and solid symbols denote the higher f_g.

6.4 Nonlinear energy transfers to lf wave components

The amplitude growth of lf components during wave group shoaling and nonlinear energy transfers from the primary frequencies (f_1 and f_2) to lf components are investigated using bispectral analysis in order to account for their nonlinear triad

interactions. The approach presented here is similar to the followed in section 5.4.3, where time series are resampled to 10Hz with a frequency resolution of 0.001Hz.

For the wave condition *C-1* (Figure 6.3) and *C-3* (Figure 6.4), plot *a*, in both cases, shows a contour plot of the cross-shore and frequency spectral distribution. Initially, close to the wave paddle, the spectral energy is dominated by the target primary frequencies (f_1 and f_2), around $f_p = 0.6$ Hz. In the vicinity of the wave-maker, f_1 and f_2 concentrate more than 98 % of the spectral energy content, which progressively decreases as they travel shoreward and transmit energy to higher and lower frequency components. During wave group propagation, high and low frequency components arise as a consequence of nonlinear triad interactions. Whereas superharmonics grow quickly during the wave-group shoaling, they also dissipate during hf wave breaking (dashed black line denotes the breaking onset). After hf wave breaking, the remaining energy is dominated by subharmonic components.

Figures 6.3b and 6.4b illustrate the cross-shore amplitude evolution for the lf wave components, comparing them to the evolution of the primary components f_1 and f_2. Both Figures display the measured (Md) amplitudes at different frequency components and the computed ones (Cp) based on bispectral analysys (Equation (2.25)). The dissipation term is assumed negligible ($H_{ds,f} \approx 0$), except for the primary frequencies only, where the dissipation term proposed by Jonsson (1967) is used (section 2.3.4). Moreover, at f_g, the separated (Sp) ILW and OFLW are also shown, where the OFLW is compared to its linear theory cross-shore evolution (Th).

In the lf domain for the wave condition *C-1* (Figure 6.3b), the ILW grows considerably during hf wave group shoaling, reaching a maximum energy content at the onset of the hf wave breaking where the shallow water limit is not reached yet ($x_{ShWL} = 6.5$m for $f_p = 0.6$Hz). After hf wave breaking, the ILW amplitude reduces but another lf component ($2f_g$) still grows. Shoreward $x \approx 5$m the ILW and $2f_g$ component reduces considerably to reach an almost zero amplitude at the shoreline. The differences between the separated (Sp) and computed (Cp) ILW and $2f_g$ indicate that the reduction in lf amplitude close to the shoreline is not explained by nonlinear frequency interactions (see Figure 6.3b).

The energy flux gradients involving the components f_1, f_2, f_g and $2f_g$ are illustrated in Figure 6.3c. Positives values of S_{nl} mean that f_g, f_1 and f_2 receive energy, whereas negative ones imply a transfer of energy from those to the rest of the triad.

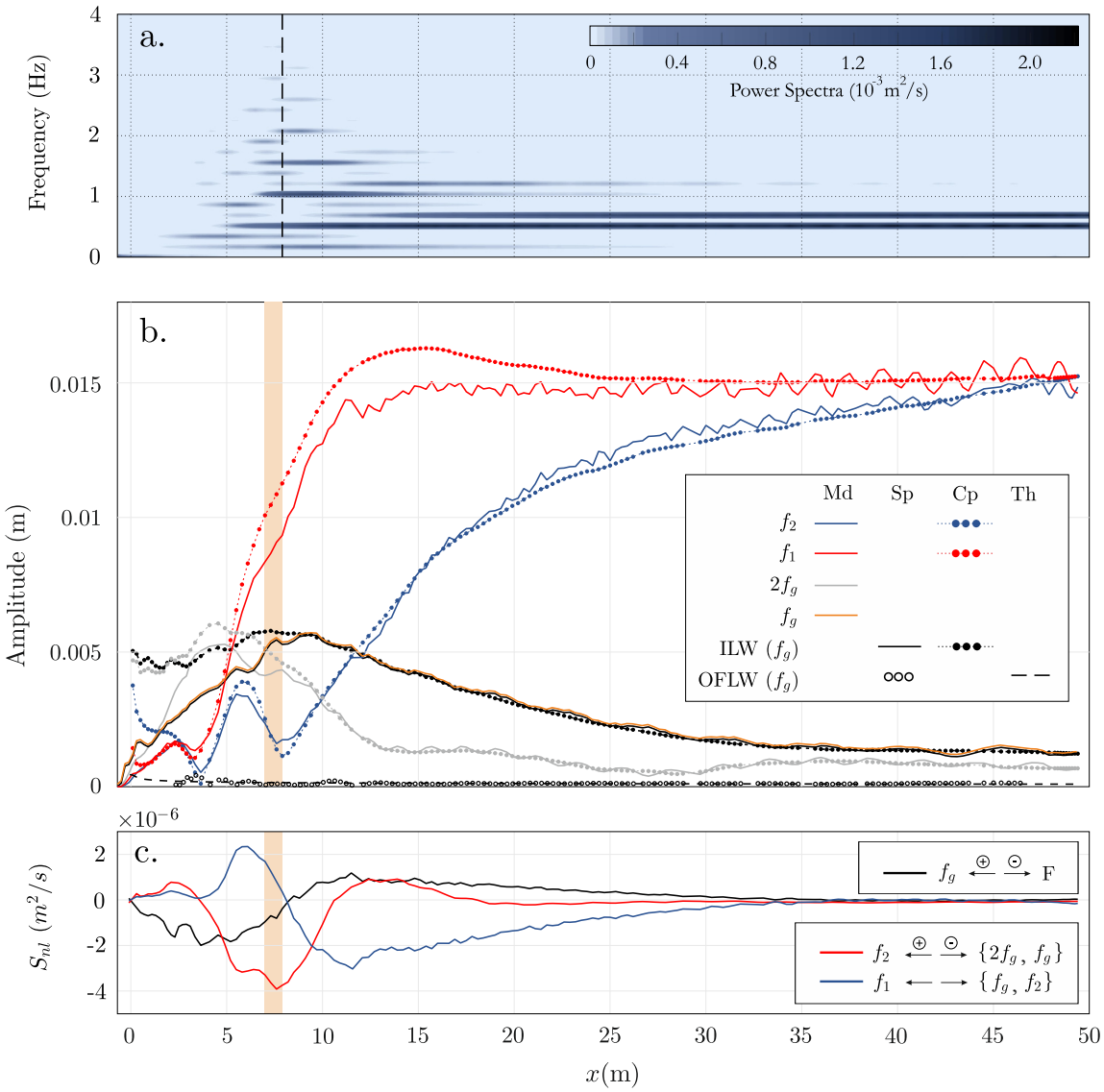

Figure 6.3: Plot a shows the cross-shore distribution of power spectra density at different frequency components for the case *C-1* ($[f_1,f_2]$ = [0.686 Hz, 0.514 Hz]). The black dashed line denote the breaking onset. Plot b gather the measured (Md), computed (Cp), separated (Sp) and theoretical (Th) wave components at f_1, f_2, $2f_g$ and f_g. Plot c illustrates certain energy flux gradients (S_{nl}), where the sign indicates the direction of the energy transfer within the triad. The brown shaded region represents the breakpoint excursion. $\beta_b = 0.104$ for this case.

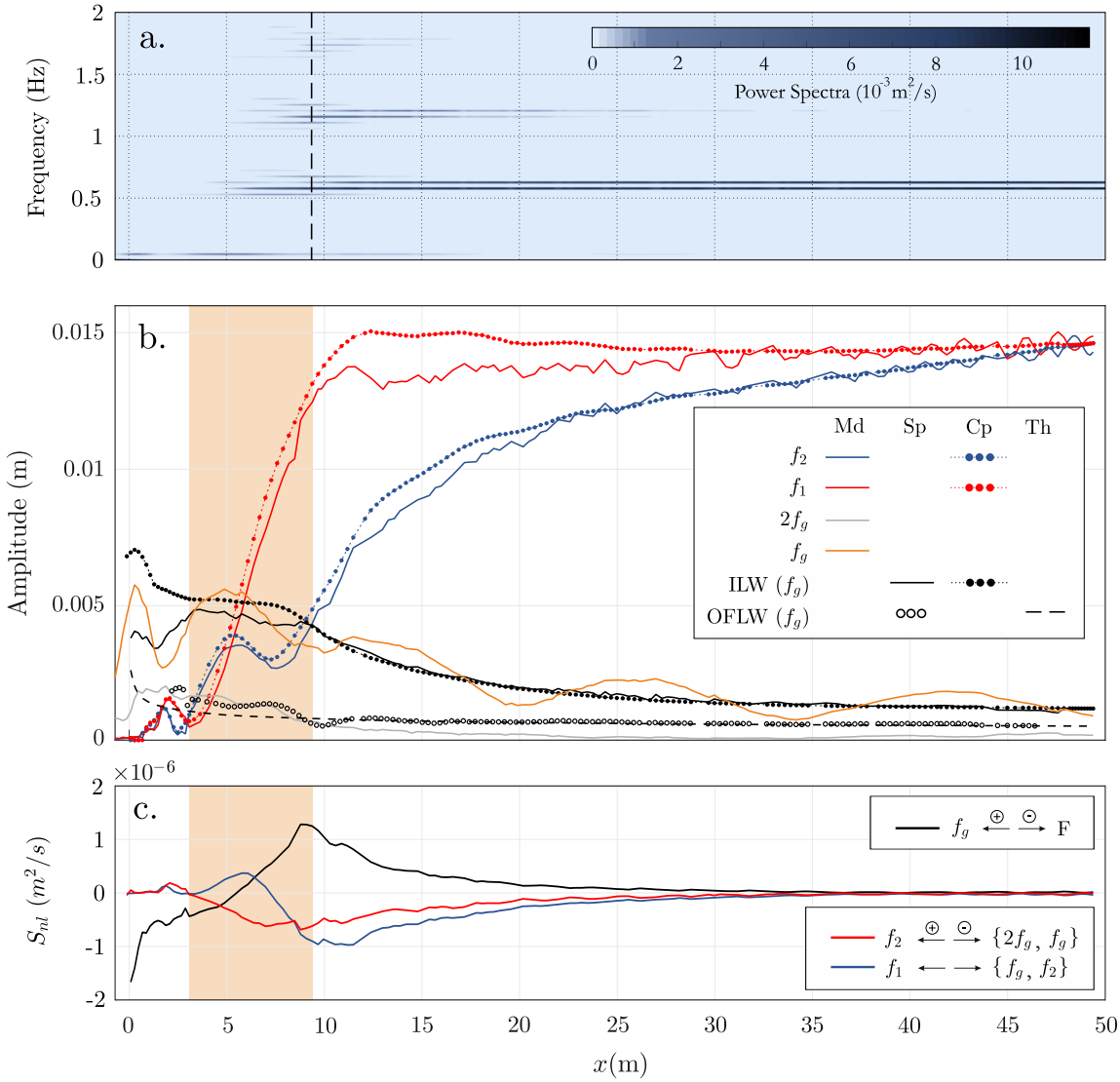

Figure 6.4: Plot a shows the cross-shore distribution of power spectra density at different frequency components for the case *C-3* ($[f_1,f_2]$ = [0.624 Hz, 0.576 Hz]). The black dashed line denote the breaking onset. Plot b gather the measured (Md), computed (Cp), separated (Sp) and theoretical (Th) wave components at f_1, f_2, $2f_g$ and f_g. Plot c illustrates certain energy flux gradients (S_{nl}), where the sign indicates the direction of the energy transfer within the triad. The brown shaded region represents the breakpoint excursion. $\beta_b = 0.339$ for this case.

For instance, the solid black line, when positive, implies a net energy transfer to f_g from F (F represents all the possible triads where f_g may be involved). For the wave condition *C-1*, f_1 is the main energy supplier to f_g and responsible for the ILW amplitude growth (blue line in Figure 6.3c). The contribution of f_1 to f_g is progressive and the maximum ILW amplitude is reached at the same place where f_1 transfers with higher intensity. In contrast, the contribution of f_2 to lf components is negligible until $x = 10$m, where the large energy transfer from f_2 seems to match with the growth of $2f_g$ near the breakpoint. For the wave condition *C-3* (Figure 6.4c), the contribution of f_2 to the lf wave components is higher than in wave condition C-1. However, f_1 is still the main energy supplier to f_g. Therefore, the differential transfer of energy from the primary frequencies to the lf domain illustrates the selective loss of energy of f_1 compared to f_2 as previously reported by Baldock et al. (2000) and Alsina et al. (2016).

For the wave condition *C-3*, a smaller growth of the ILW is observed in Figure 6.4b consistent with the smaller decay of f_1, as suggested in chapter 5. The ILW does not reach a clear maximum at the breaking location as it does for case *C-1*. Instead, the ILW increases slightly in amplitude across the surf zone and reduces in amplitude after the breaking location of the smallest hf waves indicating the loss of the group modulation. Also for *C-3*, the maximum combined $[f_1, f_2]$ contribution to f_g is again reached at the breaking onset but after that, they still supply energy with a lower rate which explains a gentle ILW growth along the surf zone. In general, throughout the studied cases, the breaking onset is an inflection point in the ILW growth due to the dissipation of primary components by hf wave breaking. Within the surf zone, the ILW may either keep growing with a lower rate for larger wave group periods or just decrease for smaller wave group periods.

6.4.1 Evolution of the ILW amplitude

Figure 6.5 compares the measured ILW amplitude ($A_{x_1}^{ILW}$) with the equilibrium solution over a flat bed ($\tilde{A}_{x_1}^{ILW}$) proposed by Longuet-Higgins & Stewart (1960) (Equation A.8 in Appendix A). This comparison is achieved at x_1 (3 meters away from the wave paddle), in the deepest region where a flat bottom is deployed along 1.5m (see Figure 3.2). Other authors like Baldock et al. (2000) or Alsina et al. (2016) have validated this second-order solution with a satisfactory fit around $\varepsilon = A_{x_1}^{ILW}/\tilde{A}_{x_1}^{ILW} \approx 1$.

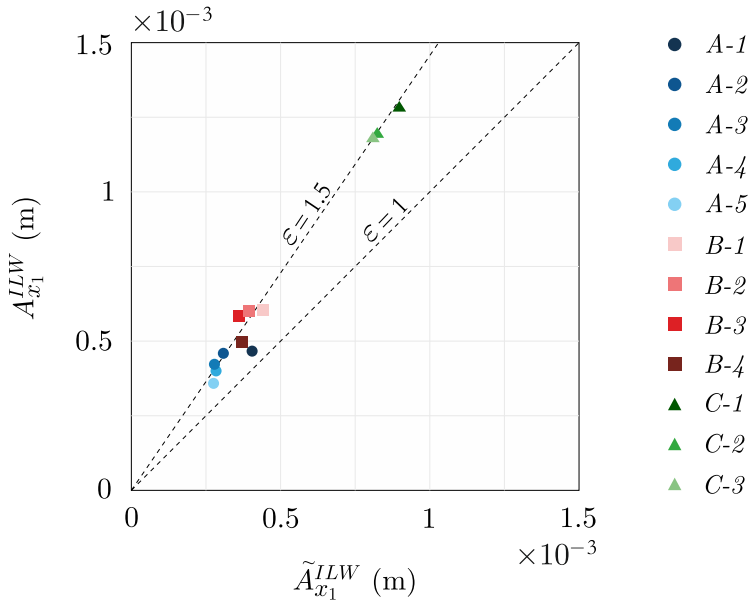

Figure 6.5: Measured ILW amplitude at x_1 ($A_{x_1}^{ILW}$) versus the theoretical equilibrium solution $\tilde{A}_{x_1}^{ILW}$ (Equation A.8 in Appendix A).

However, for the presented experiments, since this flat bottom length represents between 7 to 50% of the running ILW wavelength for the longest and shortest groups, respectively, the equilibrium second-order solution may not be fully developed. Consequently, the theoretical solution underestimates the energy at the group frequency by approximately 33%, or alternatively, ε raises to 1.5.

The overall behaviour of high and low frequency components during wave group propagation is summarized in Figure 6.6 for all tested wave conditions. The cross-shore distribution of the maximum hf wave envelope (max $\hat{\eta}$) and the absolute growth of the ILW ($A^{ILW} - A_{x_1}^{ILW}$) are illustrated for wave series *A* in Figure 6.6 (*a* and *d*), *B* in Figure 6.6 (*b* and *e*); and *C* in Figure 6.6 (*c* and *f*). For a given mean primary frequency f_p, the hf wave envelope maxima show a larger growth as the group frequency decreases (increasing wave groups length). On the contrary, the ILW behaviour shows a larger wave height growth up to the breaking onset as the group frequency increases. This is consistent with the increasing phase-lag between the wave group structure and the ILW for increasing group frequencies as shown in Figure 6.2. After the hf wave breaking onset, an important ILW amplitude decay is observed for high group frequency conditions (short wave groups, see cases *A-1*, *A-2*, *B-1*, *B-2* and *C-1*). For these wave conditions, the wave group modulation is lost over a narrow breaking region due to the small breaking excursion induced by the

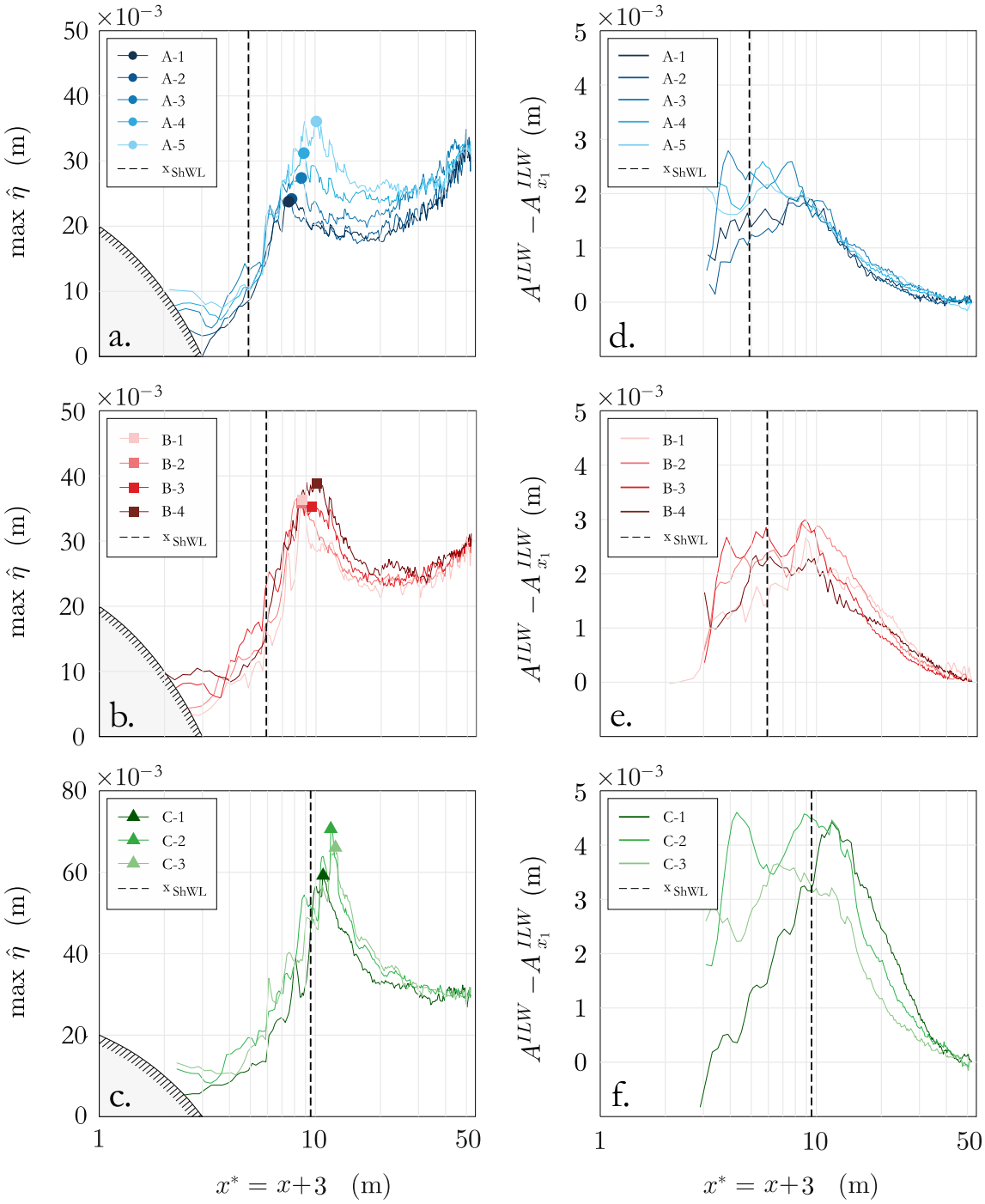

Figure 6.6: Cross-shore distribution of the hf wave envelope maxima (max $\hat{\eta}$) and absolute ILW amplitude growth ($A^{ILW} - A^{ILW}_{x_1}$). The dots indicate the breaking onsets for each wave case, whereas the black dashed line indicates where the shallow water limit is reached. The spatial domain has been plotted in log-scale to highlight the surf-swash region and has also been modified as $x^* = x + 3$ in order to include swash areas beyond the shoreline.

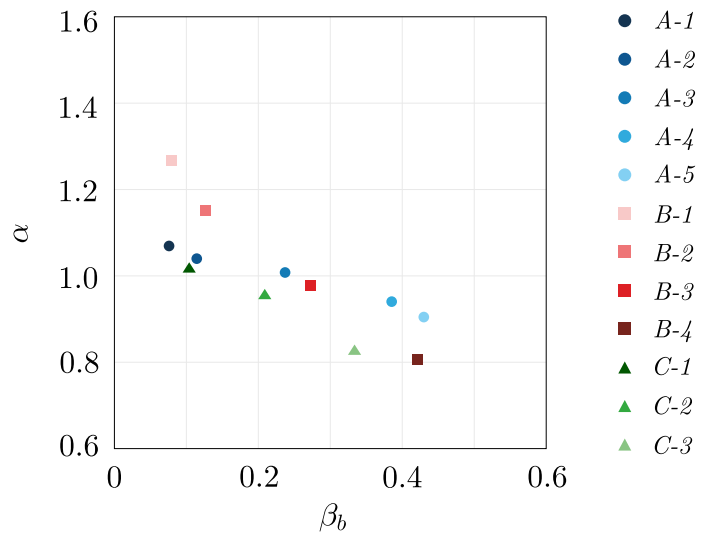

Figure 6.7: ILW growth rate during hf wave shoaling (α) versus the normalized bed parameter β_b.

group modulation. The location of ILW dissipation does not coincide with the onset of hf breaking, but rather occurs close to the shoreline, after the breaking of the smallest hf waves in the group. The long wave amplitude at the shoreline is minimal for these wave conditions. In contrast, for wave conditions with low group frequency (long wave groups) the ILW demonstrates a limited growth after the hf breaking. This is associated to a larger breaking area, a progressive reduction in the wave group modulation, and the progressive reduction in the primary waves contribution to the group frequency.

The growth rate of the ILW amplitude is expressed as a function of local depth with an unknown power α of the water depth, as $A^{ILW} \propto h^{-\alpha}$ (Van Dongeren et al., 2007). They observed numerically and experimentally this α-parameter always to be below 2.5, defined as the theoretical "shoaling" law for bound waves over a very gentle sloping bottom when a dynamic equilibrium is achieved (Longuet-Higgins & Stewart, 1962), and above 0.25 (Green's law), typical for free waves during shoaling. The observed α parameter in the present experiments is displayed in Figure 6.7. Overall, Figure 6.7 confirms that the ILW amplitude growth increases with the group frequency for the gentle slope tested in the present experiments. Extending this finding to a larger range of wave group frequencies, the results agree with the α values presented by Van Dongeren et al. (2007), where the growth rate becomes weaker for increasing β_b.

6.5 Low frequency energy dissipation after hf wave breaking

From Figures 6.3 and 6.4 (plots *b*) and Figure 6.6, the ILW energy is observed to decay strongly in the nearshore areas for the wave conditions with higher group frequency, whereas for the cases with lower group frequency, a remarkable percentage of the ILW energy is conserved and reflects at the shore travelling seaward as an outgoing free long wave (OFLW). Consequently, the reflected OFLW is more energetic as the group frequency decreases since the amplitude of the ILW and OFLW are very similar around $x = 0$ (Figure 6.4-*b*). As the definition of the reflection coefficient R is influenced by the location at which it is defined because of the spatial evolution of the ILW and OFLW, a more convenient variable D is defined in this work. This accounts for the ratio of ILW dissipation across the surf zone and reflection at the shoreline as:

$$D = \Delta A^{ILW} / A^{ILW}_{x_{ob}}, \tag{6.2}$$

where ΔA^{ILW} is the difference between A^{ILW} at the breaking onset x_{ob} and A^{ILW} at the shoreline. This variable may be easily related to the reflection coefficient used in previous works (Battjes et al., 2004, Van Dongeren et al., 2007, De Bakker et al., 2014) as $D = 1 - R$. Accordingly, similar results are achieved in Figure 6.8 compared to the presented ones in Van Dongeren et al. (2007). Figure 6.8 gathers the reflection coefficient for the tested cases compared to the non-dimensional parameter β_H (Equation 2.30) in deep water that accounts for the steepness of the beach (slope) relative to the initial steepness of the ILW. Figure 6.8 confirms that shorter groups (groups with the lower number of constituent crests) undergo a lower reflection, or alternatively, higher lf dissipation across the surf zone. The reflection coefficient is almost null ($R \approx 0$) for the cases with higher group frequency and increases to about 1 for those with lower group frequency. The data tends to follow the relation between the reflection coefficient and the surf similarity parameter $R = 0.1\xi^2$, found by Battjes (1974) and plotted in solid blue line. Actually, our data agrees with Battjes (1974) and Van Dongeren et al. (2007) yielding a transition point at $\beta_H \approx 1.25$, where dissipation is no longer expected for longer groups.

The analysis of the lf energy dissipation close to the shoreline for wave conditions

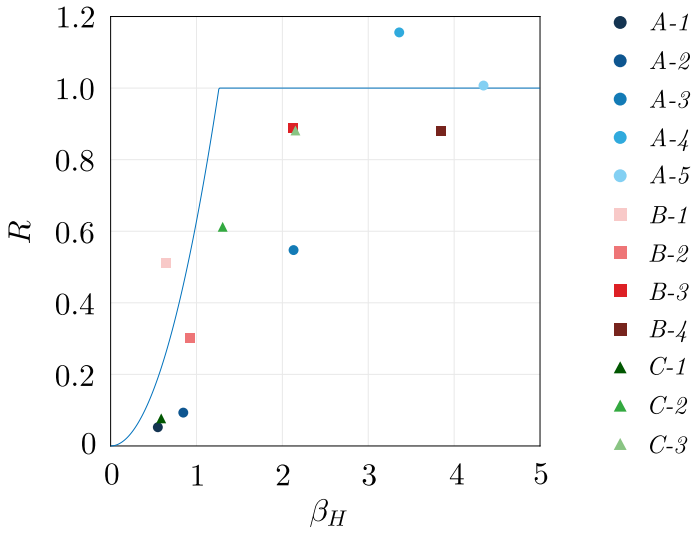

Figure 6.8: ILW reflection rate (R) in the nearshore areas versus β_H. The empirical relationship $R = 0.1\xi^2$ is displayed in solid blue line.

with higher group frequency shows a growing importance of the self-self interaction of the wave group frequency component (See Figure 6.3-*b*). For the case *C-1*, the component $2f_g$ exhibits a larger energy growth of around 3 times higher than in case *C-3*. When the group is composed of 3 short waves only, it is observed that $2f_g = f_2 - f_g$. This implies that $2f_g$ is at the same time a superharmonic of f_g and subharmonic of the triad interaction composed by f_2, f_g. Therefore, its energy gain is larger. This statement may be analytically proven using the definition of f_2 in terms of the group frequency, f_g:

$$f_2 = f_p - f_g/2, \tag{6.3}$$

and using Equation (3.1) to replace $f_p = f_g\,(n + 1/2)$. As a result,

$$f_2 = n \cdot f_g, \tag{6.4}$$

and particularly for $n = 3$, $f_2 = 2f_g + f_g$. In Figure 6.3-*b* (*C-1*), the amplitudes of f_g (black) and $2f_g$ (grey) reach a similar maximum value, which is not the case for *C-3* (Figure 6.4-*b*). Van Dongeren et al. (2007) roughly mentioned the importance of $f_2 - f_g$ in the lee side of lf waves. With the present data, the fact that $2f_g = f_2 - f_g$ shows a direct implication of the interaction between primary wave components and lf components in the increasing lf wave steepness, such that, this ILW becomes unstable and eventually break as Van Dongeren et al. (2007) suggested.

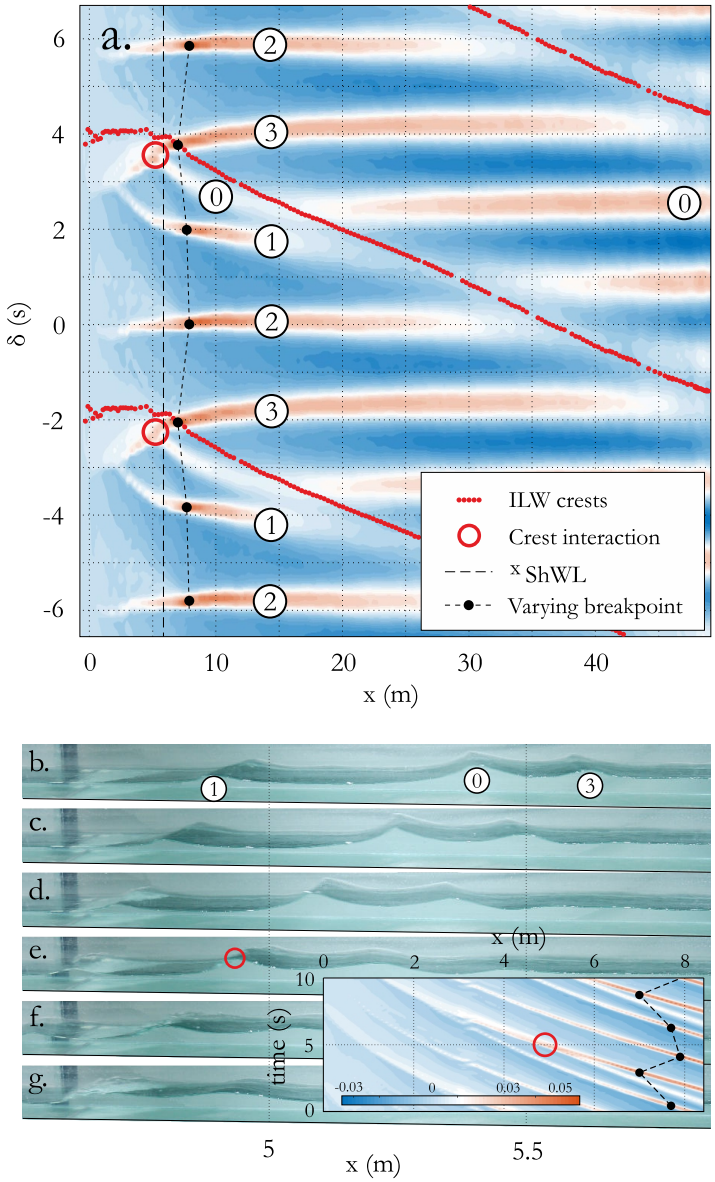

Figure 6.9: Identification of the additional breaking event (red circle) not belonging to the varying crest-breaking points (black dots) for the case *C-1*. Panel *a* shows the water surface elevation contour plot in terms of the relative time delay δ among crests, where the wave convergence in the limit between consecutive groups is evident. The wave belonging to the front side of the group (3) speeds up chasing (0) in the surroundings of the ILW crest (red dots). Panels *b-g* present the sequence of lab-pictures that record the process.

For case *C-1*, Figure 6.9 presents the water surface contour plot distribution with the cross-shore location and time-lag with respect to a central grouping crest $n = 2$ and an isolated lf wave breaking event (at the red circle). This wave condition is initially characterized by 3-4 individual waves per wave group. The wave crest $n = 3$ travelling nearly at the crest of the lf motion when arriving to shallow water conditions is shown to accelerate while wave crests $n = 0$ and $n = 1$, travelling with the trough of the lf motion are shown to decelerate. Wave crest $n = 3$ reaches wave crest $n = 0$ at the location marked with the red circle, focusing in the vicinity of the crest of lf components (ILW and $2f_g$). As a result, an isolated lf wave breaking event is illustrated at the area marked with a red circle at approximately $x = 5.5$m. The sequence *b-g* shows the individual wave crests while focusing. Immediately after, the lf wave is shown to break (Figure 6.9-g). This latter lf breaking point is consistent with the $2f_g$ decay after reaching a maximum around $x = 5$ m as illustrated in Figure 6.3-*b*.

6.6 Discussion

Nonlinear energy transfer between frequency components in the form of second-order triad interactions causes the growth of both superharmonics and subharmonics of the primary components. In the hf domain (addressed in chapter 5), the group frequency has been shown to influence the behaviour of the primary components and their superhamonics. In the lf domain, the presented influence of the wave group frequency on the growth of the ILW (which travels bound to the group structure before hf wave breaking) is consistent with previous works (Battjes et al., 2004, Van Dongeren et al., 2007), showing a clear growth dependence on the parameter β_b when the primary wave forcing is non-resonant (as in the present study). In this chapter, f_1 has been confirmed as the main energy supplier to f_g. Therefore a larger decay of f_1 for large group frequency wave conditions (low values of β_b) is likely to have a larger contribution to the growth of the ILW. Since the ILW growth and its time-lag behind the hf wave structure are physically related, the influence of the group frequency on $\Delta\psi$ has been illustrated. Increasing the difference frequency (decreasing β_b for the given beach slope) results in larger phase lags, consequently associated to a larger ILW growth.

In the surf zone, hf wave modulation is reduced due to short-wave breaking and, therefore, the primary wave forcing is reduced. For wave cases of low group frequency (long groups), this results in only a slight reduction in lf wave amplitude as a consequence of, both, the progressive reduction of the forcing from primary waves components, and nonlinear energy transfer from the group frequency to hf components. The remaining lf energy is reflected at the shore and a fairly good correlation between the incident and outgoing lf energy at the shoreline has been observed. The nonlinear energy transfer model seems to reproduce part of this behaviour of energy transfer from lf components to superharmonics, at least within the surf zone. This is consistent with the works of Thomson et al. (2006) and Henderson et al. (2006). Their finding of full reflection from the shoreline is consistent with our observations for the low group frequency (long wave groups) wave conditions. In contrast, for the high group frequency conditions, a considerably larger reduction in lf amplitude has been observed, which is not explained by nonlinear energy transfer to higher frequencies.

The analysis presented in this paper is therefore consistent with previous studies (Battjes et al., 2004, Van Dongeren et al., 2007, De Bakker et al., 2014, 2015, 2016) suggesting lf wave breaking as the mechanism behind the sharp reduction in ILW amplitude. In Van Dongeren et al. (2007) and De Bakker et al. (2016), they attributed the lf wave breaking to the growth in asymmetry of the lf wave due to self-self interaction ($\{f_g, f_g\} \rightarrow 2f_g$). However, the results presented in this paper suggest that for a decreasing number n of short waves forming the group, the component $2f_g$ also becomes a subharmonic of the coupling between primary wave and the wave group components. Therefore, the growth of lf wave height and asymmetry in the nearshore areas (surf zone) is partly explained by wave group frequency self-self interaction ($\{f_g, f_g\} \rightarrow 2f_g$), and partly by nonlinear coupling between primary wave components and the wave group frequency ($f_2 \rightarrow \{f_g, 2f_g\}$). Visually, this is explained as hf broken waves focussing at the crest of the lf wave motion destabilizing the lf wave and eventually breaking. This physical mechanism as been previously reported as bore-bore capture of short waves (Sénéchal et al., 2001a, Van Dongeren et al., 2007) or bore merging (Tissier et al., 2015). The probability of this lf breaking happening, as described in this paper for the particular case $n = 3$, tends to be reduced in groups composed of an increasing number n of short-waves. This behaviour

is consistent with the influence of β_H in the shoreline reflection coefficient R (Battjes et al., 2004, Van Dongeren et al., 2007) and with the ILW dissipation at the shoreline (represented by D).

6.7 Concluding remarks

The use of the *IBIMS-ILC* data set (section 3.3) provides a detailed analysis of the influence of the group modulation on lf wave dynamics during shoreward wave-group propagation.

The analysis of the energy transfers between the primary components (f_1 and f_2) and the lf components (f_g and $2f_g$) has confirmed that f_1 is the main energy supplier to lf components, whereas the contribution of f_2 is just local and nearby the breaking onset. This differential energy transfer to lf components explains the different amplitude decays undergone by f_1 and f_2 observed during wave-group shoaling. Moreover, the growth of the ILW in the shoaling region has confirmed previous studies in terms of amplitude and phase evolution (Janssen et al., 2003, Battjes et al., 2004, Van Dongeren et al., 2007). An accurate measurement of the phase shift $\Delta\psi$, of the ILW lagging behind the hf wave structure in the nearshore areas has been achieved. The increasing phase-lag $\Delta\psi$, as the wave group frequency f_g increases, matches the ILW growth under the same conditions.

After hf wave breaking, the wave group frequency is shown to have a large impact on the lf wave dissipation. For low group frequency conditions, the hf wave modulation decay occurs over a wider surf zone, primary wave forcing still persists in the surf zone and the lf wave decay is small and caused by nonlinear energy transfer from the wave group frequency to higher frequencies. The remaining lf energy reflects at the shoreline. However, for large group frequency wave conditions, the lf wave decay is stronger and cannot be explained by energy transfer to higher frequencies. In this case, the lf wave turns unstable in the inner surf zone due to the enhancement of lf components that are simultaneously superharmonics of f_g (self-self interaction) and subharmonics of triad interactions between the primary waves and the wave group frequency ($2f_g = f_2 - f_g$). In the latter case, lf wave breaking has been observed.

7

Long wave generation induced by differences in the wave-group structure

Author's Note: The results of this chapter have been published in Padilla & Alsina (2018).

7.1 Chapter overview

The propagation of bichromatic wave groups with the wave-group structure repeating periodically in time and its influence in long wave generation at the group frequency and subharmonics are investigated. The wave-group structure is controlled by the number of wave-groups (Rp) within a repetition period. Consequently, an important energy content is measured at lower frequencies than the group frequency f_g, in particular, at the repetition frequency f_r.

This chapter begins with a theoretical description of the breakpoint generated surf beat (Symonds et al. (1982) mechanism) and its expected behaviour when nonlinear energy transfers from the primary frequencies to lf components are negligible. In this context, a new methodology is proposed to identify the amplitude and phase cross-shore evolution of the radiated and reflected components. Then, the cross-shore evolution of the energy at f_r is partly explained by nonlinear energy transfers

from the primary frequencies, and partly by a breakpoint forcing. In particular, when Rp increases, the energy transfer to f_r during wave group shoaling reduces, and when $Rp \geq 3$, the amplitude of f_r suddenly grows at the breakpoint displaying a node-antinode pattern within the surf zone. In this case, the observed dominance of the breakpoint forcing over the energy transfers is justified by the combination of a *steep-slope* regime and *steep-wave* conditions. Finally, the shoreline oscillation is analysed under different wave conditions. Due to energy dissipation of short waves and long waves at f_g, the swash zone motion can be dominated by wave motions occurring at f_r.

7.2 Introduction

In random sea states, the low frequency energy distributes over a relatively wide range of low frequencies, usually called ingragravity band (Holman & Bowen, 1982, Guza & Thornton, 1985). The generation and dynamics of these long waves at lower frequencies than the characteristic group frequency has not been studied in detail in previous works (with the exceptions of Baldock et al. (2000) and Moura & Baldock (2018)), although lower frequency components than f_g can be an important source of energy at the shoreline when saturation of the group frequency occurs (Ruessink et al., 1998a, Ruggiero et al., 2004, Sénéchal et al., 2011). Two mechanisms are widely accepted to be responsible for the generation of these long waves. One is the difference interaction among pairs of closely neighbouring primary waves (Longuet-Higgins & Stewart, 1962). This interaction results in group-bound Incoming Long Waves (ILWs), whose reflected waves at the shoreline travel seaward as free long waves. The second mechanism, proposed by Symonds et al. (1982) (henceforth Sym82), is the radiation of shoreward and seaward long waves as a consequence of variations in the radiation stresses induced by a moving breakpoint.

During wave group propagation to the shoreline, nonlinear coupling of incident frequency components results in a net energy transfer from the primary frequencies to low frequency (lf) components (Phillips, 1960, Hasselmann et al., 1963). Using the normalized bed slope parameter β (Equation (2.16)), Van Dongeren et al. (2007) identified a *mild-slope* regime when $\beta < 0.1$, whereas a *steep-slope* regime exists when $\beta > 0.45$. On mild-slope regimes, the energy transfer to low frequency motions is

more intense than on relatively steep slopes, and the growth rate of long waves, i.e. the group-bound ILW, is larger than on steep-slope regimes (Battjes et al., 2004, Van Dongeren et al., 2007). As a result, in the mild-slope regime, the importance of long waves radiated at f_g from the moving breakpoint (Sym82 mechanism) is secondary (List, 1992, Van Dongeren et al., 2003). This fact justifies why previous authors (i.e. Janssen et al. (2003), Van Dongeren et al. (2007), among others) did not found any evidence of that mechanism in experiments performed over relatively mild slopes. Conversely, on relatively steep slopes (Kostense, 1985, List, 1992, Baldock et al., 2000, Baldock & Huntley, 2002, Contardo & Symonds, 2013), the cross-shore structure of the long-wave motion seems to be in agreement with the Sym82 mechanism. In these cases, the long waves radiated by the Sym82 mechanism and reflected at the shoreline dominates over the group-bound ILW at f_g.

The relative importance of the breakpoint generation mechanism has been also related to the short wave steepness (Baldock & Huntley, 2002, Baldock, 2012, Contardo & Symonds, 2013). The wave steepness indicates whether short wave breaking occurs in shallow water. Short wave breaking before the shallow water condition typically occurs by *steep-wave* conditions (high short wave steepness). In this case, the ILW may decay to a smaller amplitude inside the surf zone as the primary wave forcing is reduced after breaking, and the breakpoint forcing becomes dominant (Baldock & Huntley, 2002, Baldock, 2012, Contardo & Symonds, 2013). Conversely, for *mild-wave* conditions (low short wave steepness), short wave breaking occurs in shallow water and the ILW satisfies the wave dispersion relationship, being progressively "released" from the hf wave groups, and the breakpoint forcing is weak (Elgar et al., 1992, Herbers et al., 1995, Baldock & Huntley, 2002, Baldock, 2012). To quantify the long wave generation due to nonlinear energy gain of the ILWs (Longuet-Higgins & Stewart, 1962) or breakpoint forcing leading to long wave radiation (Sym82), Baldock (2012) proposed a surf beat similarity parameter $\xi_{surfbeat}$ (Equation 2.17). High $\xi_{surfbeat}$ values are associated to steep-wave conditions (high H_{OS}/L_{OS}) travelling on a steep-slope regime (high β). In these conditions, the breakpoint generated surf beat is dominant.

In dissipative beach conditions, energy saturation is observed at the incident primary components and the energy close to the shoreline can be dominated by infragravity components (Guza & Thornton, 1982, Holman & Bowen, 1984, Holland

et al., 1995, Raubenheimer et al., 1995, Ruessink et al., 1998a, Ruggiero et al., 2004, Sénéchal et al., 2011, Guedes et al., 2013). However, saturation of the infragravity energy close to the shoreline have been also reported (Battjes et al., 2004, Van Dongeren et al., 2007) especially for relatively high values of low frequency components (Guedes et al., 2013). Low frequency energy reduction can be also observed as a consequence of the dissipation of the primary forcing components after high frequency waves breaking (Baldock, 2012). In these gentle slope conditions, the swash motion might be dominated by the lower infragravity frequency range, particularly when dissipation of the higher infragravity components occurs (Ruggiero et al., 2004, Guedes et al., 2013).

7.2.1 Breakpoint generated surf beat

When a wave-group propagates on a plane beach slope, the sequence of individual wave-breaking defines an oscillatory breakpoint. The smaller waves break further shoreward, defining the inner breaking location x_{ib}, whereas the higher waves push the breakpoint seaward, defining the outer breaking location x_{ob} (see Figure 7.1). Using a parametrization of the time modulated surf zone, Sym82 modelled the generation of long waves at the breakpoint, freely propagating shoreward and seaward. These long waves radiated from the breakpoint are henceforth called RI (Radiated Incoming, towards the shoreline) and RO (Radiated Outgoing).

In Figure 7.1, a wave group propagating on a plane bed with the ILW in antiphase with the group envelope is illustrated at t_0. As the wave-group sequentially breaks (t_0 to t_1), incoming and outgoing long waves, RI and RO, are radiated from the breakpoint. From t_1 to t_2, the ILW and RI travel shoreward and reflect at the shoreline, subsequently travelling seaward as free waves, Rf. The combination of ILW, RO and Rf outside the surf zone defines the Total Ingoing and Outgoing Long Wave TIOLW. This describes a situation where the nonlinear energy transfer and breakpoint mechanisms (Longuet-Higgins & Stewart (1962) and Sym82, respectively) are comparable and define a complicated cross-shore pattern (Schäffer, 1993). Assuming a negligible contribution of the ILW, the resulting cross-shore structure is the following: within the surf zone, RI and Rf travel in opposite directions, and their amplitude relationship is expected to be $A^{RI} > A^{Rf}$ due to some energy dissipation at the shoreline. Consequently, RI and Rf develop a quasi-standing pattern with antinodes, when RI

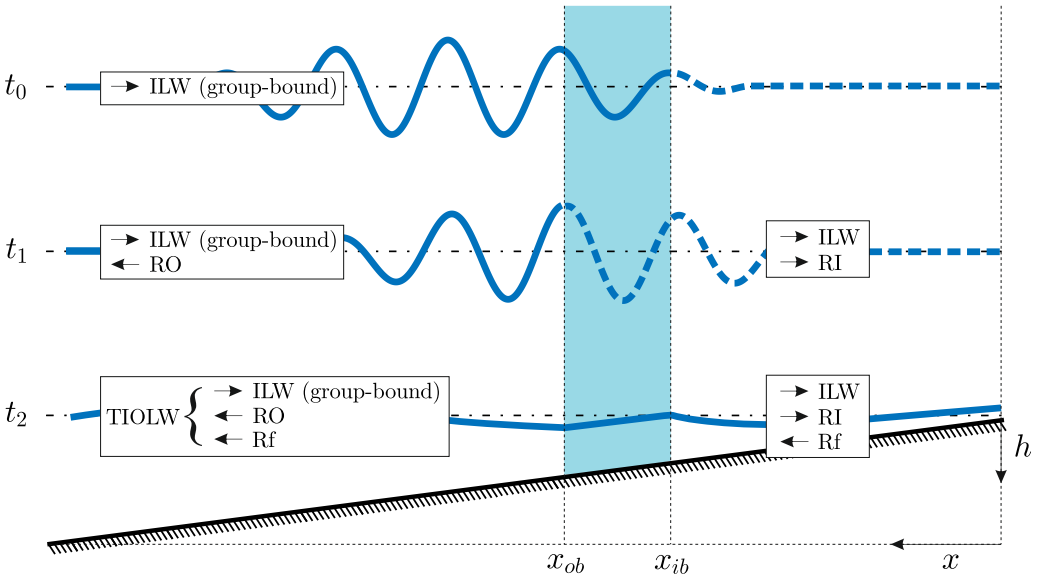

Figure 7.1: Schematic representation of the breakpoint long wave generation. t_0, t_1 and t_2 are three different time instants: In t_0, the wave-group travels shoreward with the ILW, which is group-bound in antiphase with the group envelope. Between t_0 and t_1, the smaller and higher waves forming the group break defining the inner (x_{ib}) and outer (x_{ob}) breaking locations. At this stage, the moving breakpoint radiates RI and RO shoreward and seaward, respectively. In t_2, the ILW and RI reach the shoreline and reflect back as free long waves Rf. Outside the surf zone, the combination of ILW, RO and Rf define the total ingoing and outgoing long wave TIOLW (adapted from Moura & Baldock (2017)).

and Rf are in phase, and nodes, when RI and Rf are in antiphase. Outside the surf zone, Rf and RO travel in the same direction. They combine and become TO (Total Outgoing long wave), which is equal to TIOLW when ILW is negligible. As a result of this combination, TO lays between a maximum amplitude ($A^{Rf} + A^{RO}$) if Rf and RO travel seaward in phase and a minimal amplitude ($|A^{Rf} - A^{RO}|$) when Rf and RO travel seaward in antiphase. In order to clarify, note that TO is the OFLW used in previous chapters and the name change obeys to the need to distinguish the origin of the total free outgoing long wave (reflected and radiated).

The contribution of the breakpoint forcing to generate surf beat results in a maximum outgoing amplitude A^{TO} when $\Delta\Phi = \phi^{RO} - \phi^{Rf} = 0$ rad and consequently, the linear superposition of Rf and RO creates a maximum constructive wave interference. In this case, it is said that the response of the system is maximum (Symonds et al., 1982, Kostense, 1985, Baldock et al., 2000). Conversely, when $\Delta\Phi = \pi$ rad, Rf and RO result in a maximum destructive wave interference where the response of the system is minimal. A nondimensional measure of A^{TO} is typically a function of

the relative phase $\Delta\Phi$, which is not usually known. Sym82 showed that the nondimensional parameter χ (Equation 2.13) accounts reasonably well for $\Delta\Phi$ in relative steep slopes, where a wide consensus supports that maximum response is expected at $\chi \approx 1.2$, whereas minimal response at $\chi \approx 3.7$.

7.2.2 Experimental data

The experiments used in this chapter belong to *DIFFREP-ILC* data set, whose wave conditions design, measuring process and signal post-processing can be found in section 3.4. These experiments were carried out in the Wave Evolution Flume at Imperial College London. The description of the facilities, instrumentation and experimental setup can be found in section 3.2.

The wave conditions used in this analysis correspond to 10 bichromatic wave cases where fully-modulated wave groups and their propagation on a 1:100 beach slope are measured with a dense spatial resolution of wave gauges. The wave group repetition frequency, f_r, is controlled and the long wave generation at f_r is investigated. Table 3.2 summarises the information about the wave conditions used in this chapter.

7.3 Identification of breakpoint forced long wave components

At a certain low frequency f (i.e. subharmonic of the primary frequencies), the water surface elevation filtered at f is η_f. Assuming the presence of breakpoint generated long waves, η_f is the result of the combined components RI, RO and Rf (see Figure 7.2). RI and RO are the ingoing and outgoing, respectively, radiated long waves at the breakpoint, whereas Rf is the reflected wave at the shoreline. The combination of RO and Rf from the breakpoint seaward is the total outgoing long wave TO. The cross-shore amplitude and phase evolution for RI, RO and Rf are:

$$RI(X,t) = \begin{cases} 0 & \text{if } X \leq X_{ob} \\ \text{Linear transition} & \text{if } X_{ob} \leq X \leq X_{ib} \\ A_0^{RI}\ Sh_X^{RI}\ \cos(2\pi f t - |\widetilde{k_X^{RI}}|\, X + \phi_0^{RI}) & \text{if } X_{ib} \leq X, \end{cases} \tag{7.1}$$

$$RO(X,t) = \begin{cases} A_0^{RO}\ Sh_X^{RO}\ \cos(2\pi ft + |\widetilde{k_X^{RO}}|\, X + \phi_0^{RO}) & \text{if } X \le X_{ob} \\ \text{Linear transition} & \text{if } X_{ob} \le X \le X_{ib} \\ 0 & \text{if } X_{ib} \le X, \end{cases} \tag{7.2}$$

$$Rf(X,t) = A_0^{Rf}\ Sh_X^{Rf}\ \cos(2\pi ft + |\widetilde{k_X^{Rf}}|\, X + \phi_0^{Rf}), \tag{7.3}$$

where $[A_0^{RI},\ A_0^{RO},\ A_0^{Rf}]$ and $[\phi_0^{RI},\ \phi_0^{RO},\ \phi_0^{Rf}]$ are the initial amplitudes and phases of the radiated ingoing, outgoing and reflected long waves respectively (unknown); X is the distance from the wave paddle; X_{ib} and X_{ob} are the inner and outer breakpoint locations, respectively; and

$$\widetilde{k_X^j} = \frac{2\pi f}{X} \int_0^X \frac{1}{c^j}\, dX \tag{7.4}$$

is the average wavenumber that accounts for a wave train j, propagating with phase celerity c^j, travelling a distance X from the wave paddle ($X = 0$). The superscripts j denote the RI, RO and Rf wave components because, in general, they might travel with different phase celerities (this will be discussed in Section 7.6). Assuming that radiated and reflected components propagate as free waves, the flux of energy is conserved during propagation and, consequently, the cross-shore amplitude evolves due to the shoaling coefficient

$$Sh_X^j = \sqrt{\frac{c_{g,0}^j}{c_{g,X}^j}}, \tag{7.5}$$

where c_g^j is the group celerity.

For the present study, the identification of RI, RO and Rf requires computation of Equations (7.1 – 7.3) obtaining their amplitudes $[A_0^{RI},\ A_0^{RO}$ and $A_0^{Rf}]$ and initial phases $[\phi_0^{RI},\ \phi_0^{RO}$ and $\phi_0^{Rf}]$. This computation is described as the following procedure where the ILW is assumed to be negligible. This is an important assumption, whose validity at f_r will be discussed in Section 7.5.

7.3.1 Computation of TO

Assuming the group-bound ILW to be negligible compared with the radiated components, Rf and RO are the only two energetic long wave components from X_{ob}

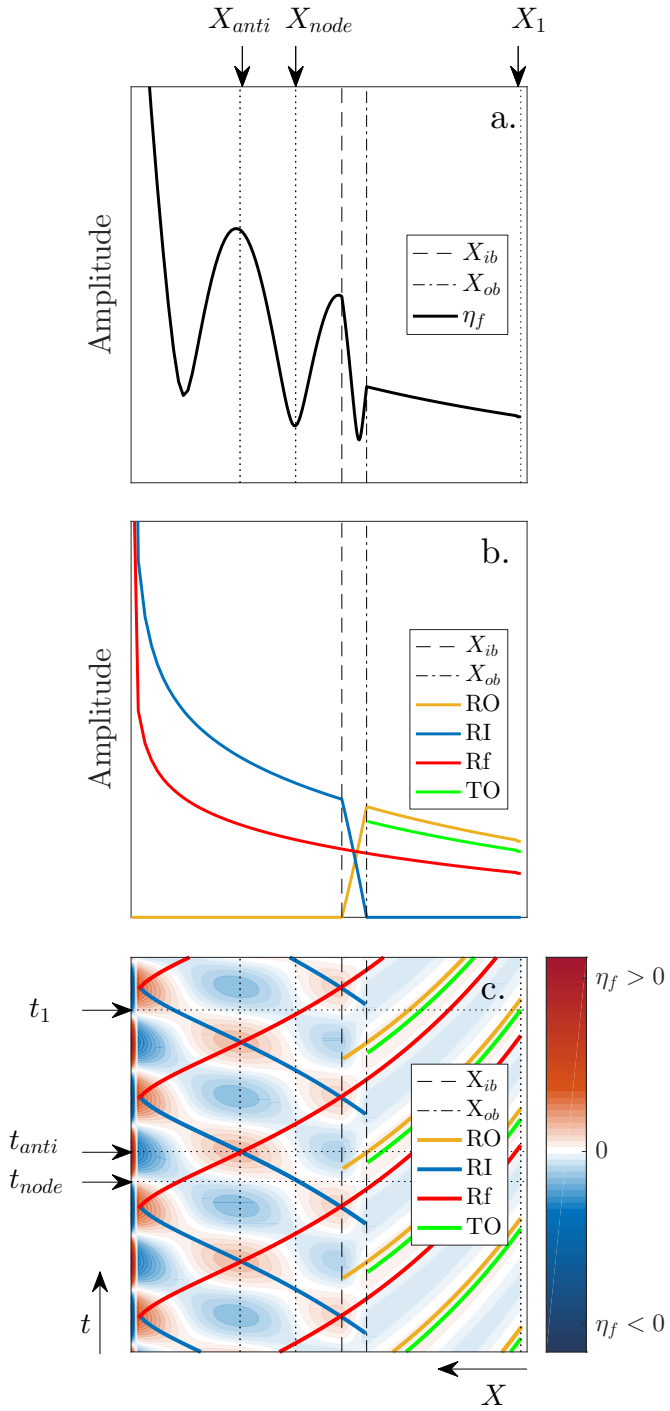

Figure 7.2: Theoretical example of breakpoint forced long waves where the Dispersion Equation is imposed for RI, RO and Rf at all times. Plot *a* shows the cross-shore evolution of the amplitude at the frequency f. Plot *b* and *c* gather the cross-shore evolution of the amplitude and phase of RI, RO, Rf and TO, respectively. The space domain X is referred to the wave generation and the limits of the moving break point are X_{ib} (inner) and X_{ob} (outer). Three points are highlighted in plot *c*: $[X_1, t_1]$ is the location and instant of a wave crest within the shoaling region; $[X_{node}, t_{node}]$ is the location of a node at the instant of maximum constructive interference between RI and Rf. $[X_{anti}, t_{anti}]$ is the location of an antinode at the instant of maximum constructive interference between RI and Rf.

seaward. Since TO is the combination of Rf and RO, the amplitude and phase at $X = 0$ are directly computed at the crest of η_f (point $[X_1, t_1]$ in Figure 7.2-*c*):

$$A_0^{TO} = \frac{\eta_f(X_1, t_1)}{Sh_{X_1}^{TO}} \tag{7.6}$$

and

$$\phi_0^{TO} = -\widetilde{|k_{X_1}^{TO}|}\, X_1 - 2\pi f t_1. \tag{7.7}$$

7.3.2 Computation of RI and Rf

From X_{ib} shoreward, RI and Rf are travelling in opposite directions. Consequently, they build a quasi standing pattern where the η_f motion is minimum at nodes (X_{node}) and maximum at antinodes (X_{anti}). By definition, RI and Rf share the same phase at the antinodes. Therefore, at the maximum constructive interference between RI and Rf (point $[X_{anti}, t_{anti}]$ in Figure 7.2-*c*), ϕ_0^{Rf} and ϕ_0^{RI} satisfies:

$$\phi_0^{Rf} = -\widetilde{|k_{X_{anti}}^{Rf}|}\, X_{anti} - 2\pi f\, t_{anti}, \tag{7.8}$$

$$\phi_0^{RI} = \widetilde{|k_{X_{anti}}^{RI}|}\, X_{anti} - 2\pi f\, t_{anti}. \tag{7.9}$$

As seen, RI and Rf are in phase at (X_{anti}, t_{anti}), whereas RI and Rf are out of phase at (X_{node}, t_{node}). Therefore, the amplitudes of RI and Rf satisfy the following linear system:

$$A_0^{RI} \cdot Sh_{X_{anti}}^{RI} + A_0^{Rf} \cdot Sh_{X_{anti}}^{Rf} = \eta_f(X_{anti}, t_{anti}), \tag{7.10}$$

$$A_0^{RI} \cdot Sh_{X_{node}}^{RI} - A_0^{Rf} \cdot Sh_{X_{node}}^{Rf} = \eta_f(X_{node}, t_{node}). \tag{7.11}$$

7.3.3 Computation of RO

From X_{ob} seaward, RO must satisfy the condition $TO = Rf + RO$, which performs the following nonlinear system:

$$A_0^{RO} \cos(\phi_0^{RO}) = A_0^{TO} \cos(\phi_0^{TO}) - A_0^{Rf} \cos(\phi_0^{Rf}), \tag{7.12}$$

$$A_0^{RO} \sin(\phi_0^{RO}) = A_0^{TO} \sin(\phi_0^{TO}) - A_0^{Rf} \sin(\phi_0^{Rf}). \tag{7.13}$$

Solving Equations (7.12) and (7.13), the amplitude and initial phase of RO at

$X = 0$ are:

$$A_0^{RO} = \frac{A_0^{TO}\ \cos(\phi_0^{TO}) - A_0^{Rf}\ \cos(\phi_0^{Rf})}{\cos(\phi_0^{Rf})} \tag{7.14}$$

and

$$\phi_0^{RO} = \arctan\left(\frac{A_0^{TO}\ \sin(\phi_0^{TO}) - A_0^{Rf}\ \sin(\phi_0^{Rf})}{A_0^{TO}\ \cos(\phi_0^{TO}) - A_0^{Rf}\ \cos(\phi_0^{Rf})}\right). \tag{7.15}$$

Equations (7.6 – 7.15) are solved for the present experimental observations to obtain the RI, RO and TO components. The solving scheme is the following:

1. Assuming the ILW to be negligible, the total outgoing TO amplitude and phase are obtained at any cross-shore location in the shoaling region by solving Equations (7.6) and (7.7). The assumption of negligible ILW is valid at the repetition frequency f_r as it will be discussed below.

2. Within the surf zone, the phase and amplitude of the ingoing breakpoint radiated long wave (RI) and the shoreline reflected long wave (Rf) are obtained at the nodes and antinodes by solving Equations (7.8–7.11). Then, the phase and amplitude at any cross-shore locations within the surf zone are obtained by linear wave propagation.

3. Finally, the breakpoint radiated outgoing long wave (RO) is obtained outside the surf zone using Equations (7.14) and (7.15) knowing the amplitude and phase of TO and Rf from steps 1 and 2.

The obtained results will be presented in Section 7.6.

7.4 Wave group and long wave propagation at the group frequency

During shoreward propagation of the wave groups, nonlinear coupling of the primary wave components [f_1, f_2] induces energy transfers to components resultant of the sum ($f_1 + f_2$) and difference ($f_1 - f_2$) of interacting frequencies. The difference frequency is the group frequency f_g and its gain of energy is visible as the growth of the group-bound ILW during shoaling. Figures 7.3 and 7.4 show the cross-shore distribution of wave amplitude at different frequency components (i.e., f_1, f_2, f_g and f_r) where wave conditions with similar f_g but different Rp are displayed in Figure 7.3, and

wave conditions with different f_g but same Rp are displayed in Figure 7.4. In plots a to c of Figures 7.3 and 7.4, the amplitude reduction of f_1 and f_2 is mainly explained by energy transfers to super- and sub-harmonics, although side-friction loses are not negligible as seen in chapter 6. In chapter 6, it has been described that, in general, f_1 contributes to the growth of f_g more than f_2, which explains why f_1 decreases before f_2. The nonlinear triad interaction $[f_1,\ f_2] \rightarrow f_g$ results in an important growth of energy at f_g, and consequently, f_g becomes the dominant lf component during shoaling (see plots a to c).

During wave-group propagation onto a beach, the short waves forming the wave groups undergo substantial nonlinear transformations due to energy transfers to hf components. The short waves become more asymmetric progressively and eventually break (shaded region in Figures 7.3 and 7.4). As a result, the energy content of hf components (f_1, f_2 and higher) is mostly dissipated and lf components become the dominant features along the surf zone. Actually, the dominance of f_g is very clear just few meters after the inner breakpoint and shoreward (see plots a to c in Figures 7.3 and 7.4). Shoreward of the short wave breakpoint, the amplitude of f_g progressively reduces due to the reduction of the primary waves energy forcing the long wave at f_g (Baldock, 2012) until the remaining energy reflects at the shoreline. In shallow water, the nonlinear triad interaction between primary components and the group frequency becomes resonant and the resultant long wave might propagate as a free wave.

Previous works (Battjes et al., 2004, Van Dongeren et al., 2007, De Bakker et al., 2014) have related the reflection coefficient at f_g with the parameter β that, for a constant beach slope and short wave breaking location, depends solely on the wave group frequency. Chapter 6 revealed that for wave condition MR-01 (C-1) the reflected wave at f_g is almost negligible due to dissipation of wave energy at f_g induced by long wave breaking. This is also confirmed in the present data by the tiny undulation of the cross-shore amplitude at f_g in plots a to c (Figure 7.3), indicating that the ILW is dominant. Alternatively, when f_g decreases (i.e., n increases from 3 to 8), no long wave breaking is expected and the magnitude of the reflected wave increases. This is confirmed by the rising amplitude of the undulations of the cross-shore ILW at f_g from plots a to c (Figure 7.4), indicating the superposition of Rf and ILW.

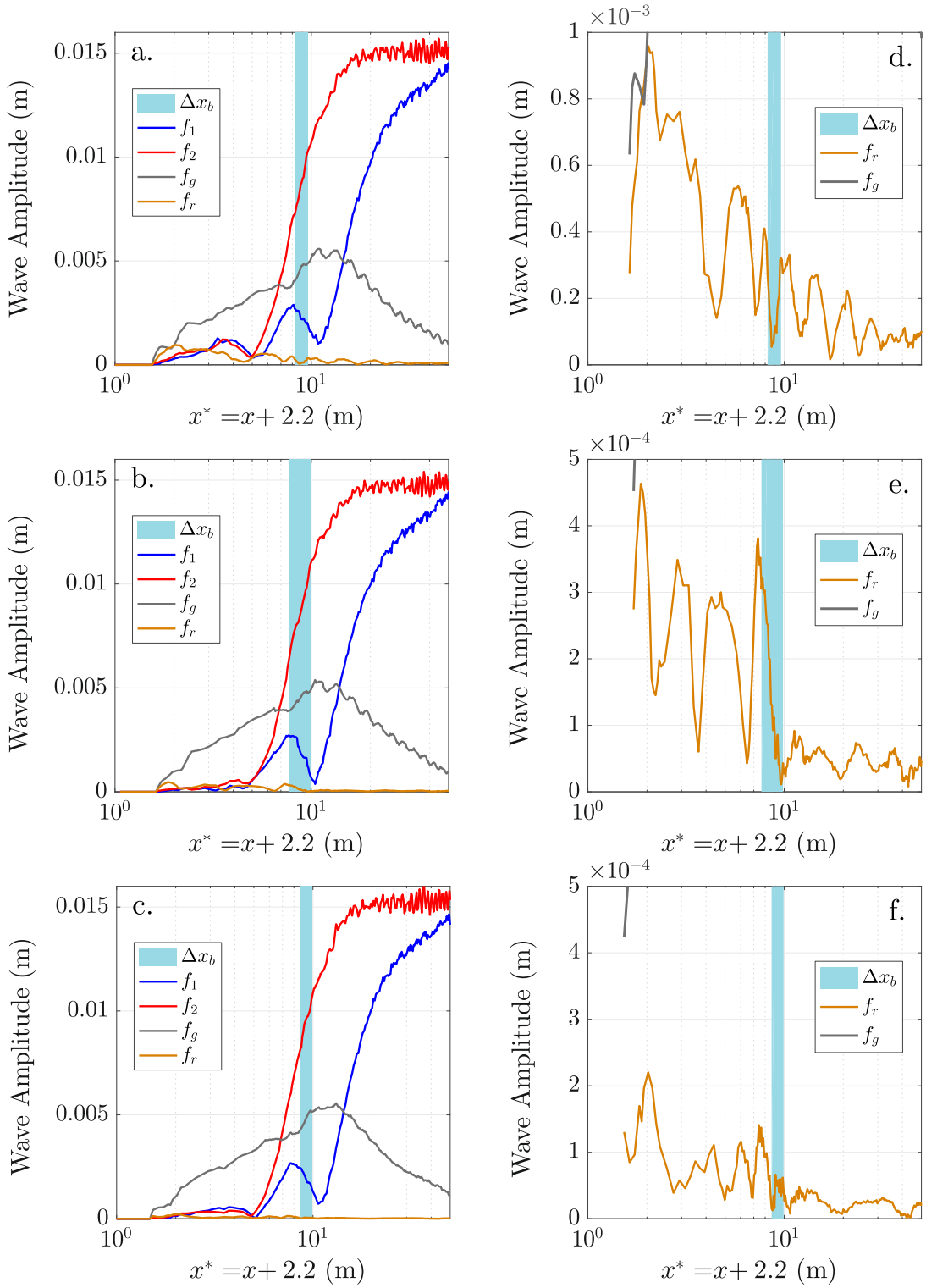

Figure 7.3: Cross-shore amplitude evolution at f_1, f_2, f_g and f_r for cases with different Rp and similar f_g: *MR-02*, $Rp = 2$ (a and d), *MR-03*, $Rp = 3$ (b and e) and *MR-06*, $Rp = 5$ (c and f). The light blue area is the breaking excursion (Δx_b) of the crests forming the groups. Note that the x-axis is in log-scale and it has been displaced +2.2m.

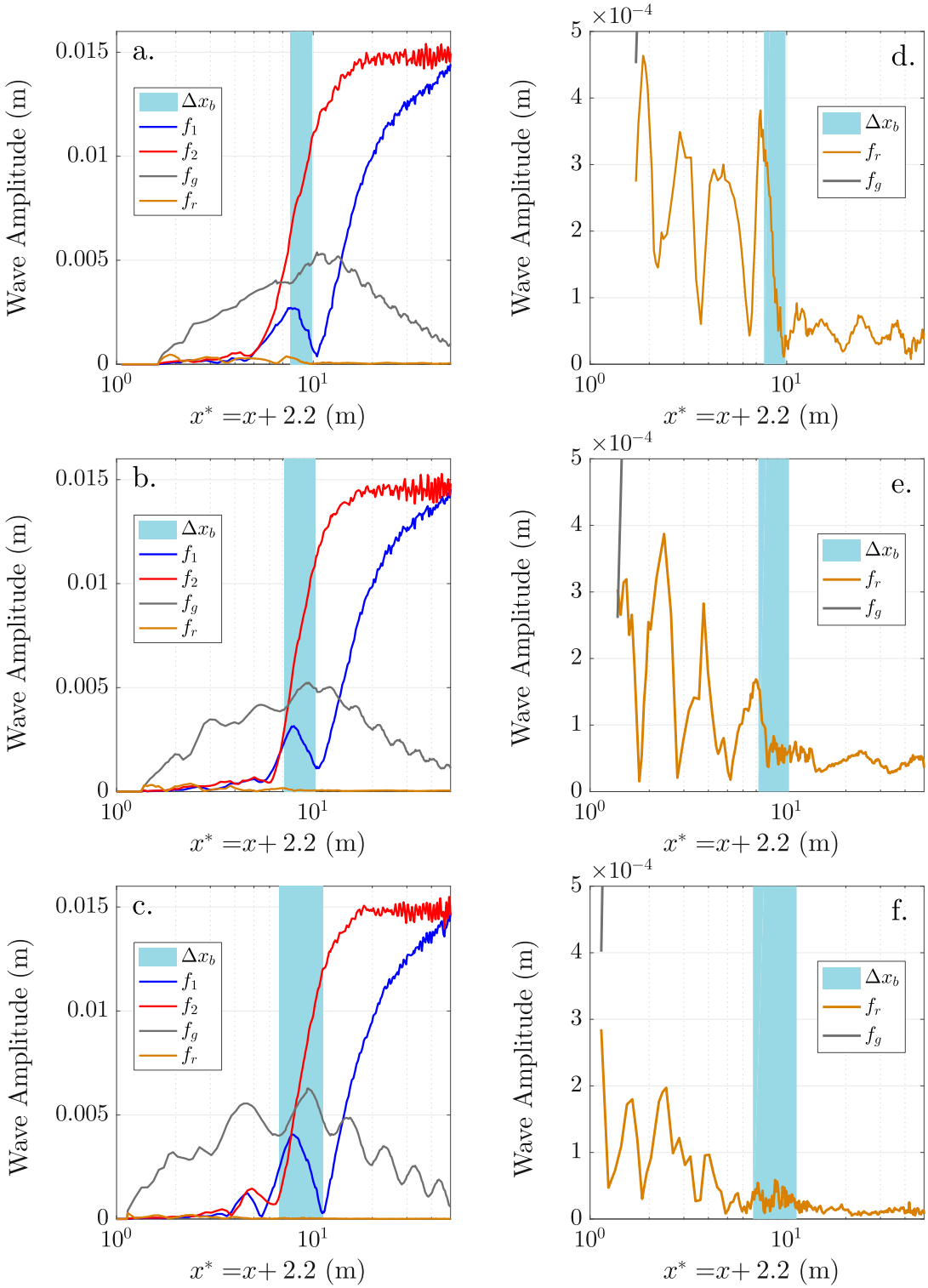

Figure 7.4: Cross-shore amplitude evolution at f_1, f_2, f_g and f_r for cases with different f_g and same $Rp = 3$: *MR-03*, $fg = 0.189$Hz (*a* and *d*), *MR-05*, $fg = 0.116$Hz (*b* and *e*) and *MR-10*, $fg = 0.074$Hz (*c* and *f*). The light blue area is the breaking excursion (Δx_b) of the crests forming the groups. Note that the x-axis is in log-scale and it has been displaced +2.2m.

7.5 Nonlinear interactions and energy transfer to f_r during wave group shoaling

As seen in Figure 3.5, Rp and f_r are closely related in the way $f_r = f_g/Rp$. This implies that f_r is a subharmonic of f_g. The value of Rp, then, plays an important role in the nonlinear energy transfer to the f_r component. For instance, when $Rp = 1$, f_r receives energy as a result of the nonlinear triad interaction $[f_1,\, f_2] \rightarrow f_r$ because $f_r = f_g$. An extensive discussion about the energy transfers when $Rp = 1$ is found in chapter 6.

When $Rp = 2$, the group frequency receives energy during shoaling as $[f_1,\, f_2] \rightarrow f_g$, however, a more detailed study of the energy transfers to f_r is required. These transfers are computed using bispectral analysis over time series resampled to 10Hz with a frequency resolution of 0.001Hz. Figure 7.5-*a* and -*c* show the superimposed energy density spectra of the water surface elevation ($S_{\eta\eta}$) at every cross-shore location. For the case *MR-02* ($Rp = 2$) in plot *a*, the most relevant energetic frequency components below the primary frequencies are highlighted. According to these frequency components, plots *b* illustrates the cumulative cross-shore energy fluxes due to nonlinear energy exchanges only ($\int_{x_1}^{x} S_{nl}\, dx$) for the most relevant triads involving f_r. For instance, blue line in Figure 7.5-*b* refers to the balance of energy exchange between f_r and the rest of energetic wave components. Therefore, negative values means a net energy transfer to f_r ($f_r \leftarrow F$). Figure 7.5-*b* shows that the net energy flux to f_r ($\mathcal{O}(10^{-7})$ m^3/s) is mainly due to contributions from the component f_1 ($[f_r,\, f_1 - f_r] \leftarrow f_1$), whereas the contribution from the remaining triads is negligible.

The same analysis about the energy transfers to f_r is illustrated in Figure 7.5-*c* and -*d* for case *MR-03* ($Rp = 3$). In this case, the net energy flux to f_r when $Rp = 3$, compared to the case with $Rp = 2$, is an order of magnitude lower ($\mathcal{O}(10^{-8})$ m^3/s). Furthermore, f_1 is the main energy supplier to f_r, followed by f_2, whereas the contribution of the remaining triads is again negligible. In general, this important reduction in the energy flux from f_1 to f_r is seen when $Rp > 2$. Consequently, there is no noticeable amplitude growth of f_r during shoaling, as seen in Figure 7.3-*e* and -*f* where no energy growth at f_r is observed before the breakpoint location.

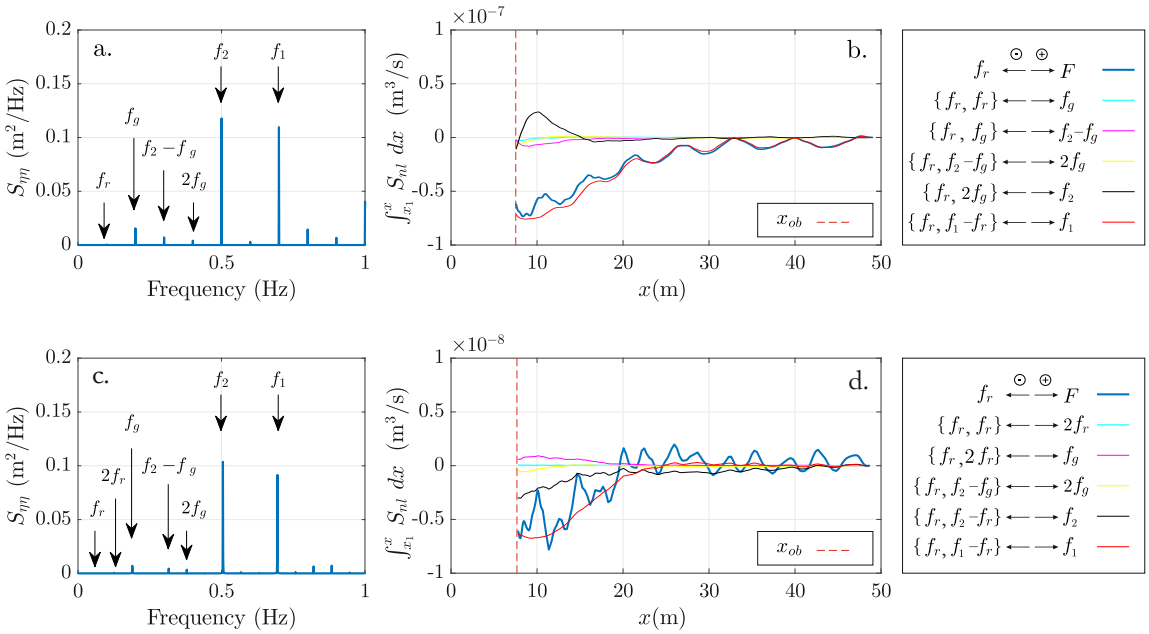

FIGURE 7.5: Plots *a*-*b* and *c*-*d* illustrates the wave cases *MR-02* and *MR-03*, respectively. The energy density spectra of the water surface elevation ($S_{\eta\eta}$) at every cross-shore location is superimposed in plots *a* and *c* in order to highlight the most relevant energetic wave frequencies below f_1 and f_2. Plots *b* and *d* show the cumulative cross-shore energy fluxes due to the triads in the legend. The red dashed line is the breaking onset x_{ob}.

7.6 Breakpoint generated long wave at f_r

The long wave behaviour at f_r within the surf zone is very different compared to f_g when $Rp \geq 3$. From the breakpoint shoreward, the amplitude of f_r suddenly grows displaying a node-antinode pattern. This is clearly observed in Figures 7.3-*e* to -*f* and 7.4-*d* to -*f*. As a consequence of this growth in f_r within the surf zone, the amplitudes of f_g and f_r are comparable in the vicinity of the shoreline.

The sudden amplitude growth at the breakpoint undergone by f_r in Figure 7.4-*d* (case *MR-03*) cannot be explained by the nonlinear energy exchanges between frequency components. In contrast, the long waves radiated by the moving breakpoint, RI and RO, and the associated reflected wave at the shoreline Rf do explain this sudden growth. Figure 7.6 gathers the measured surface elevation at f_r and the computed features RI, RO and Rf for case *MR-03*, based on the methodology proposed in Section 7.3. In plot *a*, the sum of RI, RO and Rf provides a theoretical cross-shore amplitude (Th) that is in very good agreement with the measured cross-shore amplitude (Md) at f_r. The existence of Rf and RI propagating in opposite direction develops a quasi standing pattern that explains the node-antinode

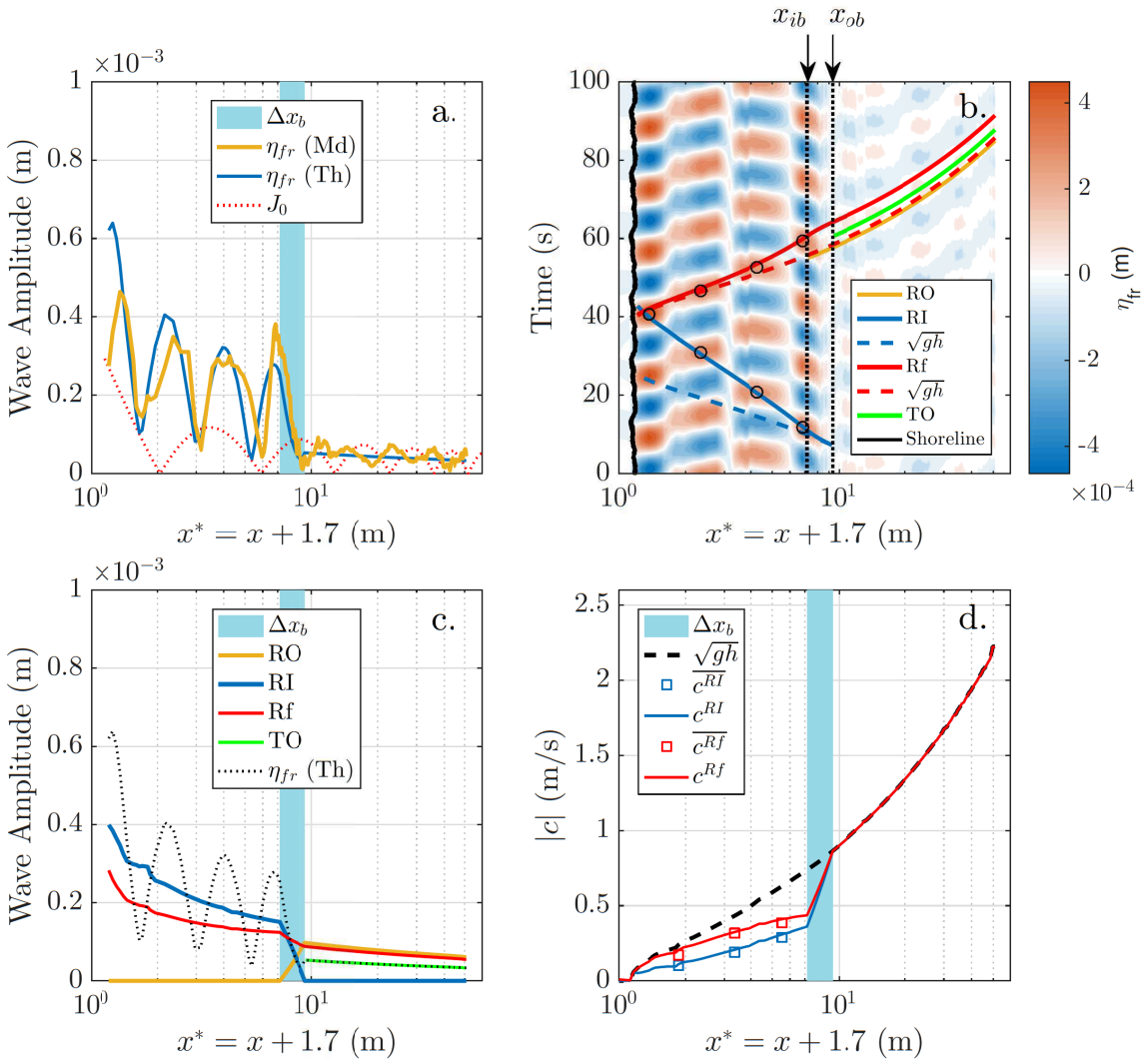

Figure 7.6: Plot *a* shows the cross-shore amplitude at the repetition frequency f_r, measured (Md) and theoretical (Th) for case *MR-03* ($Rp = 3$). Additionally, the zeroth order Bessel function (J_0) is included. Plots *b* and *c* show the cross-shore evolution of the phase and amplitude of RI, RO, Rf and TO. Plot *d* shows the actual phase velocities c^{RI} and c^{Rf} compared to the depth-induced phase velocity ($\sqrt{gh}$). In this case, $\zeta^{RI} = 5.9\text{s}^{-1}$ and $\zeta^{Rf} = 5.1\text{s}^{-1}$ (Equation (7.17)), which means $|c^{RI}| < |c^{Rf}|$ within the surf zone. The light blue area is the breaking excursion (Δx_b), delimited by $[x_{ib}, x_{ob}]$. Note that the x-axis is in log-scale and it has been displaced +1.7m.

pattern observed in the surf zone. The perfect match in the location of the nodes and antinodes validates the estimation of the phase velocities of RI (c^{RI}) and Rf (c^{Rf}). However, the zeroth order Bessel function J_0 (Lamb (1932), art. 186) is unable to correctly reproduce the standing pattern. This is partly due to the fact that the phase velocities of Rf and RI within the surf zone are no longer equal to $\sqrt{gh}$, but slower (see Fig. 7.6-*d*). Note that the surf zone is shallow water ($kd \ll \pi/10$) for f_r and, overall, $c = \sqrt{gh}$ is a valid simplification of the Linear Dispersion Equation along the flume.

RI and Rf travelling within the surf zone slower than $\sqrt{gh}$ has already been pointed out by Baldock & Huntley (2002) and Contardo & Symonds (2013). In the theoretical solution (Th) displayed in Figure 7.6-*a* the free long wave celerity within the surf zone has been obtained experimentally by using the average long wave celerity between antinodes. As the experimental velocity between antinodes provides only a local estimation but not a continuous velocity c^j, a depth-induced slow-down factor Δc is proposed to account for potential velocity reductions below $\sqrt{gh}$ within the surf zone:

$$c^j = \pm(\sqrt{gh^*} - \Delta c^j), \tag{7.16}$$

where j refers to the long wave components RI (sign -) and Rf (sign +). Experimentally, the depth-induced slow-down factor Δc is computed as:

$$\Delta c = \begin{cases} \zeta\, h^* & \text{if } x \leq x_{ib} \\ \text{Linear transition} & \text{if } x_{ib} \leq x \leq x_{ob} \\ 0 & \text{if } x_{ob} \leq x. \end{cases} \tag{7.17}$$

where ζ^j is a best fit parameter obtained by fitting Equation (7.16) to the averaged measured celerities between antinodes for RI ($\overline{c^{RI}}$) and Rf ($\overline{c^{Rf}}$), respectively (see plots *b* and *d*).

This slow down of RI and Rf is clearly seen in Figure 7.6-*b*. Solid lines show the actual phase propagation for RO, RI, Rf and TO by tracking the time-space evolution of their crests. Figure 7.6-*b* confirms that RI and Rf travel slower than the depth-induced phase velocity $\sqrt{gh}$ (dashed lines) within the surf zone. $\sqrt{gh}$ estimates around 18s to travel from the breaking onset to the shoreline, whereas RI effectively takes about 34s, which is nearly 90% more. In contrast, this percentage reduces to 43% for Rf. Outside the surf zone, $\sqrt{gh}$ reproduces quite well the phase velocity, as

it is clearly seen with TO travelling offshore. Actually, Figure 7.6-*b* suggests that the mechanism causing the slow down in RI and Rf, is no longer acting outside the surf zone since Rf and RO travel seaward with the same phase velocity (parallel lines in plot *b*).

Within the surf zone, RI and Rf travel in shallow water and the slow down in the actual phase velocity (equal to the group velocity in shallow water) compared to the $\sqrt{gh}$ estimation implies an amplitude growth for RI and Rf different from the theoretical linear shoaling. In order to preserve the energy flux conservation, the actual wave phase velocity computed in Figure 7.6-*d* is used to compute the shoaling coefficient Sh in Equation (7.5). Consequently, since the ingoing and outgoing phase velocities are remarkably different, RI and Rf have different shoaling coefficients and their cross-shore amplitudes grow differently. That explains why, in Figure 7.6-*c*, RI is slightly larger than Rf along the surf zone, suggesting small energy dissipation at the shoreline, although RI and Rf are similar at the moving breakpoint.

The case *MR-03* presented in Figure 7.6-*a* illustrates a practically minimal response scenario, in which RO and Rf are about π rad shifted at the outer breaking location. In general, a minimal response scenario does not imply almost null energy content for TO, but it does for case *MR-03* since $A^{Rf} \approx A^{RO}$ in the shoaling region. Furthermore, the linear long wave amplitude transition within the breaking excursion for RI and RO seems to reproduce the sudden amplitude growth fairly well (Figure 7.6-*a* and -*c*).

Figure 7.7 presents phase relationships for the wave cases where the breakpoint generated surf beat at f_r was clear. Figure 7.7-*a* shows the phase of the RO versus RI at the mean breakpoint location ($x_{mb} = (x_{ib} + x_{ob})/2$), where RI and RO seem to share the same phase at the mean breakpoint. This is physically consistent with radiated waves by a moving breakpoint that acts as a wave-maker. Likewise, Figure 7.7-*b* shows the phase lag between RO and Rf at the outer breakpoint location ($\Delta\Phi = \phi^{RO} - \phi^{Rf}$) against the normalized A^{TO} at x_{ob}. This amplitude is normalized by half the difference in shoreline set-up in order to be consistent with the model of Sym82. The results confirm the minimal response ($\Delta\Phi \approx \pi$) suggested for the case *MR-03*. In fact, all the tested wave cases represent a practically minimal response. Figure 7.7-*c* shows the normalized surf zone width χ against the normalized A^{TO} at x_{ob}, where $\chi \approx 3.7$ should be expected for wave conditions with a minimal response.

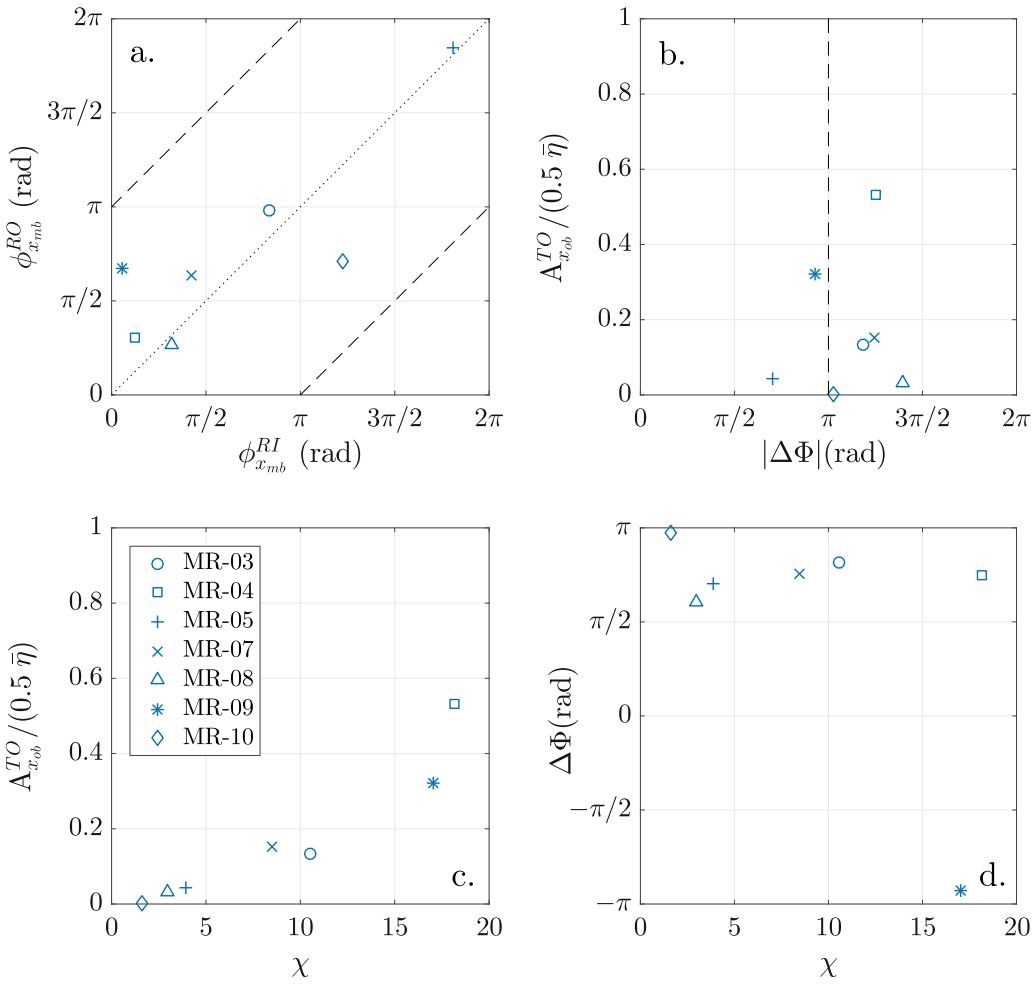

Figure 7.7: Plot a gathers the phases associated to RI and RO at the mean breakpoint (x_{mb}). Plot b and plot c compare the normalized A_{TO} at x_{ob} with $\Delta\Phi$ and χ, respectively, whereas plot d shows $\Delta\Phi$ against χ. A_{TO} is normalized by half the difference in shoreline set-up $\bar{\eta}$.

Instead, the present cases correspond to a range of χ values from 1.6 to 18.1 (see Table 7.1). These results suggest that in mild slopes $\Delta\Phi \approx \pi$ regardless χ (Figure 7.7-*d*), but the nondimensional amplitude of TO at minimal response seems to increase with χ (Figure 7.7-*c*). Note that plots *a* and *b* support the statement from Baldock et al. (2000) that in a minimal response scenario, the mean breakpoint does correspond with an antinode of the free standing wave.

7.7 Low frequency energy at the shoreline

Due to hf wave breaking and the strong short wave energy dissipation over the gentle beach slope (1:100), the remaining wave energy in the inner surf zone is mainly driven by lf components (see Figures 7.4 and 7.6). Eventually, these lf components are responsible for the uprush and backwash events that define a moving shoreline and the swash dynamics. The maximum cross-shore length of the uprush is the run-up excursion.

Figure 7.8 (plots *a*, *c*, *e* and *g*) shows the horizontal shoreline location (x_s) normalized by the run-up for the wave cases presented in Figure 3.5. Note that, x_s is measured from the shoreline at still water conditions and positive landward. As expected, the shoreline signal is, in general, dominated by large wave periods (T_g and T_r), whereas the shorter waves (T_p) are negligible. That is, lf components (f_g and f_r) are far more energetic than hf components. In fact, the frequency threshold below 0.4Hz gathers about 90% of the energy content of the shoreline signal (plots *b*, *d*, *f* and *h*).

For wave groups satisfying $Rp = 1$, f_g is the only energetic lf component. In this case, the ILW at f_g becomes the most energetic feature at the shoreline. Consequently, the moving shoreline presents a very well defined oscillation at the time scale of T_g (case *MR-01* in Figure 7.8-*a*). In contrast, cases *MR-02* ($Rp = 2$) and *MR-03* ($Rp = 3$) show a longer uprush duration (time scale of T_r), comprising 2 (plot *c*) and 3 (plot *e*) grouping structures, respectively. For the later cases, it is clear that the energy content at f_r dominates over the one at f_g in the shoreline. This loss of relative importance of f_g compared to f_r is consistent with the long wave breaking of the ILW at f_g suggested in chapter 6. However, the energy content at f_r in the swash zone progressively decreases when Rp increases, in agreement with

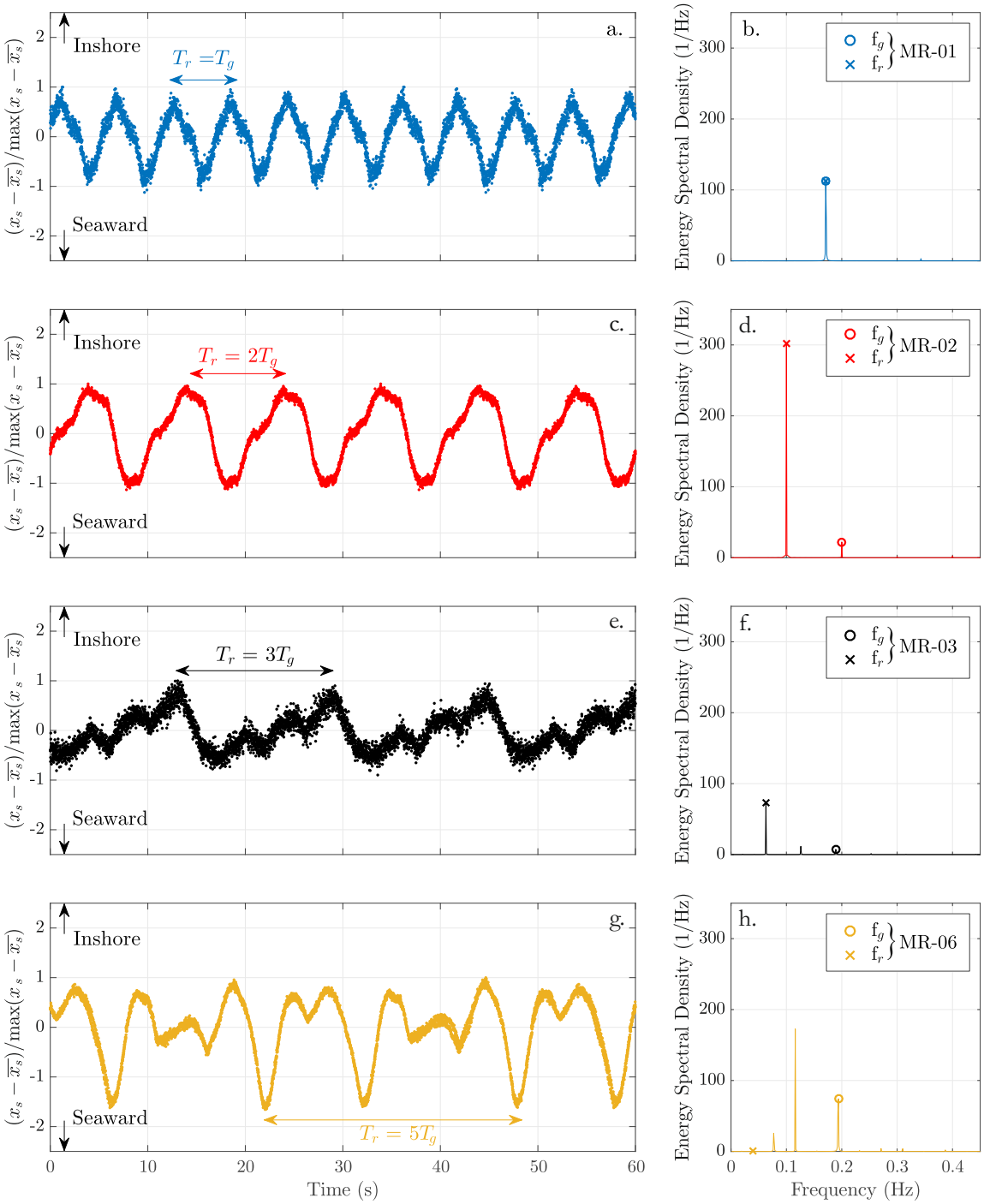

Figure 7.8: Time series of normalized horizontal shoreline location (plots *a*, *c*, *e* and *g*) and their energy spectral densities (plots *b*, *d*, *f* and *h*) for cases with *Rp* varying from 1 to 5: *MR-01* (plots *a* and *b*), *MR-02* (plots *c* and *d*), *MR-03* (plots *e* and *f*) and *MR-06* (plots *g* and *h*). The time scale of the features at T_g and T_r is highlighted and their corresponding frequencies identified and marked in the power spectrum. Note that units of the power spectrum are $1/Hz$ because the time series is non-dimensional.

Figure 7.3-*d* and -*f*.

In order to quantify the relative importance between f_g and f_r at the shoreline, Figure 7.8 (plots *b*, *d*, *f* and *h*) gathers the energy spectral density of the previously mentioned moving shoreline signals. In general, the energy content at f_r is equal or higher than the one at f_g when $Rp \leq 3$. In particular, f_r represents 91.4% of the total shoreline signal energy content for case *MR-02*, which is far higher than the 6.6% at f_g. The magnitude differences between f_r and f_g reduce for *MR-03* (f_r gather 59.9% compared to the 12.5% associated to f_g). The reduction in the relative importance of f_r turns evident for case *MR-06*, where the energy content associated to f_r (0.4%) is negligible compared to the one at f_g (39%).

7.8 Discussion

The long wave breakpoint generation has been clearly identified for frequencies lower than the wave group frequency (Figures 7.3-*d* and -*f* and Figure 7.4-*d*, and -*f*) as previously reported by Baldock et al. (2000) and Moura & Baldock (2018), among others. The fact that the moving breakpoint may radiate waves at further frequencies than just f_g has been proposed by Baldock et al. (2000) and Moura & Baldock (2018). However, most of the existing works have traditionally addressed the breakpoint generated surf beat at f_g (Kostense, 1985, List, 1992, Baldock et al., 2000, Contardo & Symonds, 2013, among others). Long waves radiated from the moving breakpoint at f_g coexist with existing ILWs which grow in amplitude during wave group shoaling. The separation of both waves (the ones due to breakpoint forcing and the ones due to nonlinear interactions) is complex at f_g. This is not the case at f_r when $Rp \geq 3$. The increase in the repetition number Rp reduces the nonlinear energy transfer to f_r as the energy flux from f_1 to f_r reduces (see Figure 7.5). The implications of this energy flux reduction have been clearly illustrated in Figure 7.3 where the amplitude at f_r in the shoaling region decreases when Rp increases. In this context, if the breakpoint generated surf beat is relevant enough, it dominates over energy transfers as seen in Figure 7.3-*d* and -*f*, and Figure 7.4-*d* and -*f*.

The present dataset is in agreement with Baldock (2012) showing that the breakpoint generated surf beat is dominant for *steep-wave* conditions over a *steep-slope* regime. Concerning the slope regime, Battjes et al. (2004) and Van Dongeren et al.

(2007) used the normalized bed slope parameter β, to identify the mild-slope regime (when $\beta < 0.1$) and the steep-slope regime ($\beta > 0.45$). Case *MR-01* ($Rp = 1$) represents a mild-slope regime ($\beta = 0.106$) where $f_r = f_g$ and the amplitude growth due to energy transfers dominates over the breakpoint generated surf beat. In contrast, if wave steepness keeps the same but Rp increases to 3 (case *MR-03*), then this case now performs a near steep-slope regime ($\beta = 0.308$) where the breakpoint generated surf beat dominates over energy transfers. Overall, β at f_r is above 0.3 for the waves cases where the breakpoint generated surf beat is identified (Table 7.1). These wave cases are in nearly steep-slope regime in agreement with List (1992), Van Dongeren et al. (2003) and Battjes et al. (2004), who observed that the breakpoint generated surf beat becomes more important with steeper slopes. The slope gradient in this study (1:100) is an order or magnitude lower than the usual one of previous experiments where the breakpoint generated surf beat has been identified (e.g., 1:20 in Kostense (1985)). However, both are comparable and perform steep-slope regimes because low frequency waves f_r over mild slopes behave similarly to higher frequency waves over steep slopes (Schäffer, 1993).

Concerning the short wave steepness, Baldock & Huntley (2002), Baldock (2012) and Contardo & Symonds (2013) showed that the breakpoint generated surf beat may be still weak if the wave conditions are mild (low wave steepness) even within

Table 7.1: Resume of different measured variables. The location where the waves forming the groups are shallow water waves is x_{ShWL}. x_{ob} is the breaking onset or outer breaking location. $\beta(f_r)$ is the normalized bed slope for f_r. $H_{s,X_1}/L_{p,X_1}$ is the initial short wave steepness. $\xi_{surfbeat}(f_r)$ is the surf beat similarity parameter for f_r. $\Delta x_b/L_{f_r}$ is the ratio between the breaking excursion and the wavelength of the long waves at f_r at the breakpoint. $\chi(f_r)$ is the normalized surf zone width at f_r.

Case	x_{ShWL} (m)	x_{ob} (m)	$\beta(f_r)$	$H_{s,X_1}/L_{p,X_1}$	$\xi_{surfbeat}(f_r)$	$\Delta x_b/L_{f_r}$	$\chi(f_r)$
MR-01	6.55	7.90	0.106	0.184	0.014	0.175	88.7
MR-02	6.63	7.43	0.192	0.019	0.026	0.165	27.1
MR-03	6.56	7.66	0.308	0.018	0.042	0.161	10.5
MR-04	6.50	12.5	0.234	0.033	0.043	0.138	18.1
MR-05	6.58	8.08	0.505	0.018	0.068	0.135	3.9
MR-06	6.63	7.73	0.485	0.019	0.066	0.058	4.3
MR-07	9.40	8.60	0.343	0.015	0.042	0.115	8.5
MR-08	26.32	8.72	0.582	0.006	0.044	0.096	2.9
MR-09	2.92	5.22	0.242	0.031	0.043	0.119	17.2
MR-10	6.64	9.04	0.782	0.019	0.108	0.117	1.6

a steep-slope regime. Most of the presented cases perform steep-wave conditions since the short waves mostly break before shallow water conditions ($x_{ob} > x_{ShWL}$ in Table 7.1). Consequently, the breakpoint generated surf beat effectively dominates. In summary, both factors (wave conditions and slope regime) are included in the surf beat similarity parameter $\xi_{surfbeat}$, Equation (2.17), proposed by Baldock (2012). This parameter indicates whether the breakpoint generated surf beat dominates (large values of $\xi_{surfbeat}$) over the energy transfers (small values of $\xi_{surfbeat}$). In the present experiments, low values of $\xi_{surfbeat}$(Table 7.1) indicates a dominance of energy transfers ($\xi_{surfbeat} \approx 0.01$), whereas higher values ($\xi_{surfbeat} > 0.04$) indicate the dominance of the breakpoint generated surf beat.

So far, we have discussed the relative importance between the breakpoint generated surf beat and the nonlinear energy transfers, assuming an existing breakpoint generated surf beat. In order to asses if the breakpoint generated surf beat may potentially exist at a certain frequency f, Baldock et al. (2000) concluded that the ratio between the length of the breaking excursion (Δx_b) and the wavelength of the free long wave at the frequency f (L_f) must be at most in the range 0.2-0.3. Certainly, this is the case since $\Delta x_b/L_{f_r} < 0.2$ for any long wave case at f_r presented in this work (see Table 7.1). Note that the limiting value (0.2-0.3) proposed by Baldock et al. (2000) is based on results at the grouping frequency f_g, but the same physical reasoning seems to be applicable to further frequencies, like f_r.

In comparison, f_g overall performs a clear mild-slope regime with $\beta \approx 0.1$ (not shown). Although the short wave steepness is high, the breakpoint forcing at f_g remains weak under a mild-slope regime with $\xi_{surfbeat}$ values importantly lower than the ones for f_r. This is consistent with a dominant ILW at f_g growing due to nonlinear energy transfers (Figure 7.3-*a* to -*c*, and Figure 7.4-*a* to -*c*). On top of that, even assuming nonlinear energy transfers to be negligible, the development of the Sym82 mechanism at f_g seems to be unlikely according to Baldock et al. (2000) since overall $\Delta x_b/L_{f_g} > 0.3$.

As expected from Baldock et al. (2000), the radiated waves RO and RI are in phase at the mean breakpoint for minimal response scenarios (Figure 7.7-*a*). In the design of the experiments for the present dataset, the aim was to cover a range of wave cases comprising maximum and minimal response at f_r. This range is achieved when $\Delta\Phi$, the relative phase between RO and Rf at the breakpoint, goes from 0 to π

radians. The easiest way to modify $\Delta\Phi$ is modifying the location of the breakpoint. To do so, the present dataset comprises wave cases modifying (1) the initial amplitude of the primary frequencies [a_1, a_2]; (2) the mean primary frequency f_p; (3) the repetition of the wave groups Rp; and (4) the number of crest forming the wave groups n. However, the combination of low frequencies (f_r) and mild slope (1:100) seems to prevent the development of any scenario different from a nearly minimal response. The values for $\Delta\Phi$ vary around π regardless the normalized surf zone width χ (Figure 7.7-*b* and -*d*), which traditionally should correspond to values of $\chi \approx 3.7$ (Symonds et al., 1982, Baldock et al., 2000, Contardo et al., 2018). The computed values of χ goes from 1.6 to 18.1 instead (Figure 7.7-*c* and -*d*), performing always a nearly minimal response.

The measured slow down detected for the RI and Rf within the surf zone has been previously reported, at least, by Baldock & Huntley (2002) and Contardo & Symonds (2013). In both cases, the steeper slope induces a shorter surf zone and the resulting slow down is an order or magnitude lower than the one in Figure 7.6. Contardo & Symonds (2013) suggest that the slow down might be due to inaccuracies measuring the bathymetry or allocating the shoreline. However, the high level of spatial resolution achieved by the present dataset excludes this possibility.

The importance of long waves at lower frequencies is clearly seen in mild-slope conditions due to the possible saturation of higher low frequency energy close to the shoreline and the increasing importance of lower frequency components. Energy dissipation of the wave group long wave has been found, and consequently the run-up is dominated by f_r. Previous works have already reported the saturation of long wave energy at f_g close to the shoreline (Van Dongeren et al., 2007, Sénéchal et al., 2011, Guedes et al., 2013, De Bakker et al., 2014) and a frequency roll off to lower frequencies of the run-up signal (Ruessink et al., 1998a, Ruggiero et al., 2004).

7.9 Concluding remarks

New laboratory data on surf beat generation induced by bichromatic wave groups propagating on a 1:100 sloping bed have been presented. The investigated wave groups comprise a range of group frequencies (f_g), wave group repetitions (Rp), mean primary frequencies (f_p) and initial amplitudes of the primary components (a_1, a_2) for

fully modulated cases ($a_1 = a_2$). Measurements with high spatial resolution include moving shoreline time series and water surface elevation with clear identification of the breakpoint excursion.

The generation and propagation of long waves at lower frequencies than the group frequency have been investigated. In particular, frequencies associated with the wave group structure beyond the main group, i.e., repetition of the wave group structure at f_r, has been investigated. The long wave generation and growth at f_r is partly due to the breakpoint forcing (breakpoint oscillating by the repetition of the wave group structure) and partly due to the nonlinear energy transfer from primary frequencies. It has been found that the dominance of one or other mechanism (breakpoint forcing, nonlinear energy transfer) depends on the repetition frequency for the given beach slope. For low repetition numbers ($Rp < 3$), the cross-shore amplitude at f_r progressively grows mainly due to nonlinear energy transfers from f_1, whose energy flux depends on the repetition number Rp. When $Rp = 2$, the wave group represents a nearly *mild-slope* regime at f_r ($\beta < 0.2$) and the breakpoint generated surf beat at f_r is negligible compared to the nonlinear energy gain of f_r. In contrast, when the wave group sequence repeats, at least, after 3 groups ($Rp \geq 3$), the nonlinear energy transfer during wave group shoaling is drastically reduced.

The cross-shore amplitude of f_r suddenly grows at the breakpoint and develops a node-antinode pattern along the surf zone. In this case, the wave group performs a *steep-slope* regime at f_r ($\beta > 0.3$) and, consequently, the breakpoint generated surf beat at f_r dominates over the nonlinear energy transfers. With a dominant breakpoint generated surf beat, a new methodology is proposed to compute the actual amplitude and phase evolution of the radiated components by the moving breakpoint (RI and RO) and the reflected wave at the shoreline (Rf).

From the breakpoint shoreward, RI and Rf travel in opposite directions developing a quasi-standing pattern that explains the nodes and antinodes identified along the surf zone. The distance between nodes has confirmed the slow down in the phase velocity of both RI and Rf far below the expected depth-induced velocity $\sqrt{gh}$.

From the breakpoint seaward, TO is the linear combination of RO and Rf. Due to the combination of wave conditions and slope regime for this study, the normalized amplitude of TO suggests a nearly minimal response of the breakpoint generated surf beat for all the tested cases. This minimal response is also confirmed by the

difference phase ($\Delta\Phi \approx \pi$) between RO and Rf. For steeper slopes $1 : \mathcal{O}(10)$, the nondimensional parameter χ has traditionally been a good descriptor of the maximum ($\chi \approx 1.2$) and minimal response ($\chi \approx 3.7$) of the breakpoint generated surf beat. However, this might not be the case for f_r on milder slopes (1:100) because minimal response is performed regardless χ varying from 1.6 to 18.1. Instead, data suggest that the magnitude of the minimal response grows with increasing χ. On top of that, at the mean breakpoint, RI and RO seem to share the same phase at minimal response scenarios.

For the presented beach slope and wave conditions, saturation has been observed at the primary frequencies and group frequency. In this situation, the swash zone is dominated by lower frequencies, i.e., the repetition frequency f_r.

8

Conclusions and further work

8.1 Conclusions

The research questions posed in chapter 1 have been addressed through wave flume experiments divided into 2 data sets: *IBIMS-ICL* and *DIFFREP-ICL*. They comprise a variety of new experimental wave conditions performing fully modulated bichromatic wave groups propagating on a 1:100 sloping bed. *IBIMS-ICL* data set aimed to explore the propagation of identical wave groups and the influence of the wave group period on short wave breaking and long wave dynamics. Alternatively, *DIFFREP-ICL* data set aimed to investigate the generation of longer waves than the group structure due to the periodic repetition of the wave-group structure. Our experimental approach relies in a high spatial resolution and accurate analysis of the wave groups and associated long wave dynamics.

Therefore, answering the research questions posed in chapter 1:

> **How can the limitations of a first-order wave generation be practically overcome in order to properly address the experimental study of propagating long waves?**

A first-order wave generation gives rise to unwanted free waves (spurious waves) due to its incapacity to fully satisfy the second-order boundary condition at the wave paddle. Ideally, the development of a second-order wave generation theory and its implementation in the wave paddle should be the suitable approach to properly

generate second-order long waves. However, in practical terms, the magnitude of this challenge is beyond the purposes of this thesis, and particularly, we do not have access to the commercial software implemented in the wave paddles. Instead, a methodology to correct the generation of wave groups by reducing the presence of spurious waves in the low frequency domain is implemented with successful results.

The proposed methodology is summarized in the following steps:

1. Identification and quantification of the existing spurious wave at the target frequency as a consequence of an initial wave generation based on a first-order input.

2. Back propagation of the quantified spurious-wave amplitude and phase to the wave paddle location.

3. Addition of a correcting wave to the original first-order generation input. The correcting wave is designed to be in antiphase with the spurious wave, sharing the same amplitude. As a result, their destructive interference eliminates the spurious wave.

The application of these steps at every target frequency provides, in practice, similar results than a theoretical second-order generation function. It is important to highlight the identification and quantification of the spurious energy content at the target frequency, as mentioned in step 1:

- Identification. The spurious waves are free waves travelling shoreward and in linear superposition with the existing wave trains at the same frequency. As a result of this superposition, the cross-shore amplitude performs an undulating pattern similar to the quasi-nodes and -antinodes due to the phase relationship between the spurious wave and the existing wave trains.

  A model to estimate the location of these quasi-nodes and -antinodes using linear wave theory is presented and validated with theoretical and experimental data. The analysis of these quasi-node -antinode locations provides qualitative and useful information about the number of existing wave trains at the target frequency, their nature (free or bound) and their relative propagation direction (same or opposite direction).

- Quantification. The identification of the existing wave trains at the target frequency (number, nature and propagation direction) allows improving existing separation procedures whose outcome is the quantification of the existing wave trains, i.e., their amplitude and phase. The separation procedure proposed in this chapter is especially designed to properly separate the group-bound ILWs. The separation procedure is seen to be numerically stable with excellent results due to the high resolution of the experimental conditions.

The analysis of the cross-shore undulating pattern in order to determine the number, nature and propagation direction of existing wave trains at a certain frequency has never been implemented before and offers an useful tool to effectively assess if the generated wave condition is indeed the desired wave field. This analysis might substantially improve existing wave separation techniques locally adapting the particular behaviour of any propagating wave train.

What is the influence of the Group Modulation on the short wave breaking on a mild slope?

The group modulation defines a sorted sequence of short waves with higher waves in the centre of the group and smaller ones at the edges. As the wave-group propagates into shallower water, each wave forming the group breaks at a different location and overall, the sequence of breaking events defines a moving breakpoint. The breakpoint oscillates with the group frequency and its amplitude (breakpoint excursion) defines the surf zone width. Longer wave groups (lower f_g) have shown a longer breakpoint excursion and their breaking onsets move seaward compared to shorter wave groups.

The breaking process starts, as expected, in the centre of the group where the short waves are higher and consequently less stable. Then, the breaking sequence moves to the adjacent waves at both sides with a slight dominance of the wave-group backside. This is explained by the effective depth reduction induced by the existence of a group-bound ILW. The wave-height reduction of the short waves within the surf zone is very well described by the wave-heigth to water-depth ratio (γ), as expected in dissipative conditions where the Iribarren Number is low ($\xi < 0.1$). Indeed, the effect of the group frequency, through effective water depth reduction induced by the ILW, is accounted by the γ-parameter, which is shown to increase with the

group frequency. Traditional models to estimate γ using the Iribarren number (ξ) does not account for the group modulation, however a modified Iribarren number is proposed in this thesis to accounts for the group modulation adding a ratio between the short-waves and the wave-group wavelengths.

During wave-group propagation, the short waves forming the group undergo substantial nonlinear transformations mainly leading to an horizontal symmetry reduction due to the increasing contribution of superharmonics of the primary waves. The influence of the group frequency in the wave skewness is seen crucial on mild slopes, where skewness increases as f_g decreases, whereas vertical asymmetries remains secondary and only relevant from the breaking onset onwards. The wave skewness grows until a limiting value is reached, where the wave becomes unstable and breaks. Therefore, the breaking onset is varied by the group modulation through the wave skewness and it explains why breaking onsets move seaward with longer wave groups.

Finally, the influence of the group modulation in the wave skewness certainly implies an homologous influence in the energy transfer from the primary frequencies to the superharmonics. Overall, the cross-shore evolution of the superharmonics $2f_1$, $2f_2$ and $f_1 + f_2$ is well explained in terms of nonlinear triad-interaction energy exchanges from the primary frequencies. The energy transfer from f_2 to $2f_2$ comprises most of the energy exchanges from f_2 and it is more intense for increasing f_g. Conversely, the energy transfer from f_1 to the superharmonics is negligible and its energy exchanges seem to be more oriented to lf components instead, i.e., the group frequency component. A larger energy transfer from f_1 to f_g as the wave group frequency decreases is translated in a reducing skewness associated to the f_1 contribution. Traditionally, it has been accepted that the growth of lf components by energy transfer from short wave components does not affect to the short wave energy budget. The present experiments show the opposite but an influence on the hf skewness.

What is the influence of the Group Modulation on the long wave propagation?

The growth of the group-bound ILW within the shoaling region has confirmed the relationship between the amplitude and phase evolution. The ILW is seen to lag behind the wave-group structure with an increasing phase-lag as f_g increases. This is in agreement with a higher ILW amplitude growth rate under the same conditions.

This ILW evolution is the results of energy exchanges from the primary frequency components. The analysis of these energy exchanges has confirmed that lower primary frequencies have a larger influence. Particularly, f_1 is the is the main energy supplier to lf components. In contrast, the contribution of f_2 (higher frequency) is secondary and local nearby the breaking onset. This differential energy transfer to lf components provides a reasonable explanation for the different amplitude decay undergone by f_1 and f_2 observed during wave-group shoaling. f_1 decays more than f_2 and this decay increases as the f_g increases, in agreement with an increasing energy transfer from f_1 to f_g.

After the short wave breaking, the group modulation, i.e, the group frequency, have a large impact on the lf wave dissipation. For low group frequency conditions, the short wave modulation decays over a wider surf zone. In these conditions, the primary wave forcing persists, the ILW amplitude decay is moderate and caused by a net energy exchange from f_g to higher frequencies. The remain energy is consequently reflected at the shoreline. In contrast, the ILW decay is stronger for large group frequency conditions and cannot only be explained by energy exchanges between frequency components. Instead, a lf wave breaking event has been observed in nearshore areas partly explained by the enhancement of lf components that are simultaneously superharmonics of f_g and subharmonics of the primary components.

What is the generation mechanism and dynamics of long waves longer than the wave group period?

The group modulation implies a moving breakpoint whose influence generating long waves is secondary in gentle beach slopes compared with nonlinear energy transfers to the group frequency. However, differences in the wave-group structure also implies variations in the breakpoint motion at the repetition frequency f_r that force long waves at f_r and that, under certain conditions may dominate over the energy exchanges. In this case, the long wave generation and growth at f_r is partly explained by the breakpoint forcing and partly by nonlinear energy exchanges from the primary frequencies to f_r. For a beach slope 1:100, a dominance of the breaking forcing over the nonlinear energy exchanges was found when the wave group sequence repeat at least, after 3 groups ($Rp \geq 3$). In these conditions, a drastic reduction in the energy transfer from f_1 to f_r is observed.

At f_r, the dominance of the breaking forcing is illustrated by the sudden amplitude growth at the breakpoint, developing an undulating pattern within the surf zone. This cross-shore behaviour typically belongs to breakpoint generated surf beat where the nonlinear energy trasnfers are negligible. In these conditions, a methodology to compute the actual amplitude and phase evolution of the radiated components (RI and RO) by the moving breakpoint and the reflected wave at the shoreline (Rf) is proposed with excellent results.

From the breakpoint shoreward, RI and Rf travel in opposite directions developing a node-antinode pattern. The analysis of the nodes-antinodes location confirmed a deceleration of the RI and Rf components, showing a phase velocity below the expected $\sqrt{gh}$ within the surf. From the breakpoint seaward, the amplitude of the total outgoing component at f_r (linear superposition of RO and Rf) suggests a nearly minimal response for all the tested cases. This fact was also confirmed by the relative phase between Rf and RO. In contrast to what has been reported in steeper slopes (1:$\mathcal{O}(10)$), the parameter χ was unable to describe the relative phase between RO and Rf, and therefore, the surf-beat response for the tested cases on a milder slope (1:100). Instead, the magnitude of the minimum response tends to grow with increasing χ.

The analysis of the long wave dynamics in the swash zone suggested an energy saturation of the primary waves and the group frequency. Consequently, the swash motion is dominanted by lower frequencies than the group frequency, like f_r.

8.2 Suggestions for further work

- **Long wave breaking.** The long wave breaking is a process with important implications in coastal morphology, swash motions and run-up. Unfortunately, the long wave breaking is not completely understood yet. Therefore, trying to define a long wave breaking criteria similar to the existing ones for hf wave breaking seems a reasonable approach. A long wave breaking event has been reported in detail in this thesis and strong energy dissipations consistent with long wave breaking have been observed in general for the higher lf components. If the long wave breaking is due to its own instability, then homologous monochromatic waves with similar wave height at the breakpoint should also break defining a limiting long wave-height to water-depth ratio. In this case, a saturation of the group frequency might be confirmed.

  If these reasoning were confirmed, then a non-breaking long wave may be compared with a set of homologous monochromatic waves with different wave height. In this case, all the monochromatic waves above a certain wave height will break defining a limiting wave-height to water-depth ratio clearly above the measured ratio of the non-breaking long wave.

  To address this investigation, a new data set has been already measured, but not presented in this thesis. This data set includes a breaking and a non-breaking long wave case (Cases *C-1* and *C-3*, respectively, belonging to *IBIMS-ICL* data set). Furthermore, a set of monochromatic waves with different wave heights was measured associated to C-1 and C-3. The analysis of these data set is in progress and should provide a better understanding about the difference between breaking and non-breaking long waves. In this context, the nondimensional parameter β is a good descriptor of the lf reflection at the shoreline (seen in chapter 6), but might it also be a good descriptor of the long wave breaking?

- **Surf and swash dynamics under extreme dissipative conditions**. A long-time change in the interactions between hydrodynamic, sediment transport and morphological processes is supported by the increasing number of highly energetic storm events every year. This evolution is typically attributed to climate change and will have an important impact in a number of vulnerable

coastal regions in the upcoming years.

During shoreward wave propagation, the incoming energy budget that eventually reach the shoreline is limited. Any excess of energy is dissipated by wave breaking at the surf zone. In nearshore areas, depth-induced wave breaking is a common process among incident short waves where increments in their wave heights do not necessarily implies an increase in the run-up at the shoreline. In this context, the surf zone undergoes saturation of the high frequency components, the short wave progressively dissipates their energy and the mass of water at the shoreline is driven by lf waves (infragravity waves). Under dissipative conditions, saturation of the infragravity energy close to the shoreline may occurs as mentioned in chapter 7, especially for relatively high values of low frequency components. In these conditions, the swash motion might be dominated by the lower infragravity frequency range, i.e., a frequency roll off to lower frequencies of the run-up signal.

Under very dissipative conditions, as performed by highly energetic storm events, this frequency roll off in nearshore areas is expected to be a far more relevant process. In this context, may the high dissipation of the higher lf wave components be attributed to long wave breaking? If this is the case, can we quantify the impact of long wave breaking on the sediment transport? What is the relative impact of the long wave breaking and the infragravity-motion-dominated shoreline over the morphology change during an storm event? The answer to these questions are relatively unknown and the behaviour of very dissipative environment is not completely understood due to the complexity of developing field experiments under very energetic storm events.

- **Numerical validation of the energy exchanges.** Within the influence of the group modulation on hf and lf wave dynamics, this thesis have addressed the energy exchange between the primary components and superharmonics and subharmonics of the primary components on mild-slope conditions from a experimental point of view. The next steep is to assess the influence of the group modulation on steeper slopes and confirm existing findings reported in the literature. In this context, the capacity of existing numerical models, such as Swash or Xbeach, to correctly reproduce the energy exchanges may be properly assess.

- **Numerical validation of the dominating breaking forcing.** It is very interesting to check if the same balance between the nonlinear energy exchange and the breakpoint forcing experimentally observed in this thesis is numerically preserved. In this case, particular attention requires the undulating pattern within the surf zone because a different location of the node-antinodes will imply that the observed slow down of RO and Rf within the surf zone is not numerically explained.

- **The influence of the human and experimental error in performing a proper wave separation.** The existing separation procedures, so as the presented in this thesis, are very sensitive to the noise. This noise is partly due to experimental uncertainties beyond human control, and partly by human error. In order to optimise the wave separation procedure it is very interesting to investigate the impact of human errors, such as the difference between the practical location of the instruments and the theoretical one. In this context, is it possible to estimate the associated error to a certain local array configuration (number and separation of the instruments)?

- **Experimental data interpolation using neural networks.** The key of the excellent results achieved in this thesis is the high resolution of the tested wave conditions. Their proper measuring required an average of 5 hours of full-attention per wave case. In most of the experimental facilities, this level of resolution is not possible. Therefore, the use of neural networks to interpolate data points between measured locations could mean a improvement in existing data sets and a important time saving. The application of neural networks in other disciplines for similar purposes is promising. The application to water surface elevation signals will be easily assessed by the existing *IBIMS-ICL* and *DIFFREP-ICL* data sets

References

Aagaard, T., & Greenwood, B. (2008). Infragravity wave contribution to surf zone sediment transport - the role of advection. *Marine Geology*, *251*(1-2), 1–14. 1, 17

Aknin, D. (2015). Creating a shallow-water experimental wave environment, phd thesis. *Imperial College London*. 44

Alsina, J., & Baldock, T. (2007). Improved representation of breaking wave energy dissipation in parametric wave transformation models. *Coastal Engineering*, *54*(10), 765–769. 82

Alsina, J. M., Padilla, E. M., & Cáceres, I. (2016). Sediment transport and beach profile evolution induced by bi-chromatic wave groups with different group periods. *Coastal Engineering*, *114*, 325–340. 2, 3, 13, 17, 63, 80, 94, 95, 109

Alsina, J. M., van der Zanden, J., Caceres, I., & Ribberink, J. S. (2018). The influence of wave groups and wave-swash interactions on sediment transport and bed evolution in the swash zone. *Coastal engineering*. 1

Babanin, A. (2011). *Breaking and dissipation of ocean surface waves*. Cambridge University Press. vii, 19, 23

Babanin, A., Chalikov, D., Young, I., & Savelyev, I. (2007). Predicting the breaking onset of surface water waves. *Geophysical research letters*, *34*(7). 86, 94

Baldock, T. (2012). Dissipation of incident forced long waves in the surf zone – implications for the concept of "bound" wave release at short wave breaking. *Coastal Engineering*, *60*, 276–285. 18, 25, 26, 95, 101, 121, 122, 129, 140, 141, 142

Baldock, T., & Huntley, D. (2002). Long–wave forcing by the breaking of random gravity waves on a beach. In *Proceedings of the Royal Society of London A: Mathematical, Physical and Engineering Sciences*, vol. 458, (pp. 2177–2201). The Royal Society. 14, 18, 25, 26, 101, 121, 135, 141, 143

Baldock, T., Huntley, D., Bird, P., O'Hare, T., & Bullock, G. (2000). Breakpoint generated surf beat induced by bichromatic wave groups. *Coastal Engineering*, *39*(2), 213–242. 2, 3, 13, 14, 15, 17, 26, 44, 63, 94, 101, 109, 120, 121, 123, 138, 140, 142, 143

Battjes, J., Bakkenes, H., Janssen, T., & Van Dongeren, A. (2004). Shoaling of subharmonic gravity waves. *Journal of Geophysical Research: Oceans*, *109*(C2). 16, 17, 26, 27, 51, 57, 59, 79, 95, 100, 101, 113, 116, 117, 118, 121, 122, 129, 140, 141

Battjes, J., & Stive, M. (1985). Calibration and verification of a dissipation model for random breaking waves. *Journal of Geophysical Research: Oceans*, *90*(C5), 9159–9167. 24, 25

Battjes, J. A. (1974). Surf similarity. In *Coastal Engineering 1974*, (pp. 466–480). 24, 26, 82, 113

Battjes, J. A., & Janssen, J. (1978). Energy loss and set-up due to breaking of random waves. In *Coastal Engineering 1978*, (pp. 569–587). 24

Bertin, X., De Bakker, A., Van Dongeren, A., Coco, G., Andre, G., Ardhuin, F., Bonneton, P., Bouchette, F., Castelle, B., Crawford, W. C., et al. (2018). Infragravity waves: from driving mechanisms to impacts. *Earth-Science Reviews*. 1

Biésel, F. (1952). Équations générales au second ordre de la houle irrégulière. *La Houille Blanche*, (3), 372–376. 2, 12, 13, 72, 100

Bowen, A. J., Inman, D., & Simmons, V. (1968). Wave 'set-down'and set-up. *Journal of Geophysical Research*, *73*(8), 2569–2577. 24, 82

Bowers, E. (1977). Harbour resonance due to set-down beneath wave groups. *Journal of Fluid Mechanics*, *79*(1), 71–92. 1

Brocchini, M., & Baldock, T. (2008). Recent advances in modeling swash zone dynamics: Influence of surf-swash interaction on nearshore hydrodynamics and morphodynamics. *Reviews of Geophysics*, *46*(3). 27

Collis, W., White, P., & Hammond, J. (1998). Higher-order spectra: the bispectrum and trispectrum. *Mechanical systems and signal processing*, *12*(3), 375–394. 20, 21

Contardo, S., & Symonds, G. (2013). Infragravity response to variable wave forcing in the nearshore. *Journal of Geophysical Research: Oceans*, *118*(12), 7095–7106. 18, 121, 135, 140, 141, 143

Contardo, S., Symonds, G., & Dufois, F. (2018). Breakpoint forcing revisited: Phase between forcing and response. *Journal of Geophysical Research: Oceans*. 14, 143

Dally, W. R., Dean, R. G., & Dalrymple, R. A. (1985). Wave height variation across beaches of arbitrary profile. *Journal of Geophysical Research: Oceans*, *90*(C6), 11917–11927. 24

De Bakker, A., Herbers, T., Smit, P., Tissier, M., & Ruessink, B. (2015). Nonlinear infragravity-wave interactions on a gently sloping laboratory beach. *Journal of Physical Oceanography*, *45*(2), 589–605. vii, 3, 20, 21, 22, 72, 117

De Bakker, A., Tissier, M., Marieu, V., Sénéchal, N., Ruju, A., Lara, J., & Ruessink, B. (2013). Infragravity wave propagation and dissipation on a low-sloping laboratory beach. In *Proceedings of the Conference on Coastal Dynamics*, (pp. 443–452). 2, 16

De Bakker, A., Tissier, M., & Ruessink, B. (2014). Shoreline dissipation of infragravity waves. *Continental Shelf Research*, *72*, 73–82. 2, 4, 26, 27, 101, 113, 117, 129, 143

De Bakker, A., Tissier, M., & Ruessink, B. (2016). Beach steepness effects on nonlinear infragravity-wave interactions: A numerical study. *Journal of Geophysical Research: Oceans*, *121*(1), 554–570. 17, 27, 117

De Vries, J. v. T., Van Gent, M., Walstra, D., & Reniers, A. (2008). Analysis of dune erosion processes in large-scale flume experiments. *Coastal Engineering*, *55*(12), 1028–1040. 17

Dean, R. G., & Dalrymple, R. A. (2004). *Coastal processes with engineering applications*. Cambridge University Press. 24

Deigaard, R., Jakobsen, J. B., & Fredsøe, J. (1999). Net sediment transport under wave groups and bound long waves. *Journal of Geophysical Research: Oceans*, *104*(C6), 13559–13575. 17

Doering, J., & Bowen, A. (1987). Shoaling surface gravity waves: A bispectral analysis. In *Coastal Engineering 1986*, (pp. 150–162). 85, 86

Doering, J., & Bowen, A. (1995). Parametrization of orbital velocity asymmetries of shoaling and breaking waves using bispectral analysis. *Coastal Engineering*, *26*(1-2), 15–33. 73, 85, 86

Elgar, S., & Guza, R. (1985). Observations of bispectra of shoaling surface gravity waves. *Journal of Fluid Mechanics*, *161*, 425–448. 2, 18, 19, 20, 73, 86, 93, 94, 95

Elgar, S., & Guza, R. (1986). Nonlinear model predictions of bispectra of shoaling surface gravity waves. *Journal of Fluid Mechanics*, *167*, 1–18. 85, 86

Elgar, S., Herbers, T., & Guza, R. (1994). Reflection of ocean surface gravity waves from a natural beach. *Journal of Physical Oceanography*, *24*(7), 1503–1511. 26

Elgar, S., Herbers, T. H. C., Okihiro, M., Oltman-Shay, J., & Guza, R. T. (1992). Observations of infragravity waves. *Journal of Geophysical Research: Oceans*, *97*(C10), 15573–15577. 2, 25, 101, 121

Goda, Y. (1970). A synthesis of breaker indices. In *Proceedings of the Japan Society of Civil Engineers*, vol. 1970, (pp. 39–49). Japan Society of Civil Engineers. 24

Guedes, R., Bryan, K. R., & Coco, G. (2013). Observations of wave energy fluxes and swash motions on a low-sloping, dissipative beach. *Journal of geophysical research: Oceans*, *118*(7), 3651–3669. 28, 102, 122, 143

Guza, R., & Thornton, E. B. (1982). Swash oscillations on a natural beach. *Journal of Geophysical Research: Oceans*, *87*(C1), 483–491. 18, 28, 73, 93, 121

Guza, R., & Thornton, E. B. (1985). Observations of surf beat. *Journal of Geophysical Research: Oceans*, *90*(C2), 3161–3172. 26, 120

Hansen, N.-E. O., Sand, S. E., Lundgren, H., Sorensen, T., & Gravesen, H. (1980). Correct reproduction of group-induced long waves. In *Coastal Engineering 1980*, (pp. 784–800). 44

Hasselmann, K., Munk, W., & MacDonald, G. (1963). Bispectra of ocean waves, time series analysis m. rosenblatt, 125–139. 19, 20, 21, 72, 120

Henderson, S. M., & Bowen, A. (2002). Observations of surf beat forcing and dissipation. *Journal of Geophysical Research: Oceans*, *107*(C11). 101

Henderson, S. M., Elgar, S., & Bowen, A. (2001). Observations of surf beat propagation and energetics. In *Coastal Engineering 2000*, (pp. 1412–1421). 26

Henderson, S. M., Guza, R., Elgar, S., Herbers, T., & Bowen, A. (2006). Nonlinear generation and loss of infragravity wave energy. *Journal of Geophysical Research: Oceans*, *111*(C12). 23, 26, 101, 117

Herbers, T., & Burton, M. (1997). Nonlinear shoaling of directionally spread waves on a beach. *Journal of Geophysical Research: Oceans*, *102*(C9), 21101–21114. 21, 22

Herbers, T., Elgar, S., & Guza, R. (1995). Generation and propagation of infragravity waves. *Journal of Geophysical Research: Oceans*, *100*(C12), 24863–24872. 2, 25, 101, 121

Herbers, T., Russnogle, N., & Elgar, S. (2000). Spectral energy balance of breaking waves within the surf zone. *Journal of physical oceanography*, *30*(11), 2723–2737. 20, 21

Holland, K., Raubenheimer, B., Guza, R., & Holman, R. A. (1995). Runup kinematics on a natural beach. *Journal of Geophysical Research: Oceans*, *100*(C3), 4985–4993. 121

Holman, R., & Bowen, A. (1982). Bars, bumps, and holes: models for the generation of complex beach topography. *Journal of Geophysical Research: Oceans*, *87*(C1), 457–468. 120

Holman, R., & Bowen, A. (1984). Longshore structure of infragravity wave motions. *Journal of Geophysical Research: Oceans*, *89*(C4), 6446–6452. 121

Holthuijsen, L. H. (2010). *Waves in oceanic and coastal waters*. Cambridge university press. 15

Huntley, D., & Bowen, A. (1975b). Comparison of the hydrodynamics of steep and shallow beaches. *Nearshore sediment dynamics and sedimentation*, (pp. 69–109). 27

Huntley, D. A., & Bowen, A. J. (1975a). Field measurements of nearshore velocities. In *Coastal Engineering 1974*, (pp. 538–557). 27

Janssen, T., Battjes, J., & Van Dongeren, A. (2003). Long waves induced by short-wave groups over a sloping bottom. *Journal of Geophysical Research: Oceans*, *108*(C8). 2, 11, 16, 17, 34, 46, 72, 79, 100, 118, 121, 172

Jonsson, I. G. (1967). Wave boundary layers and friction factors. In *Coastal Engineering 1966*, (pp. 127–148). 23, 106

Kim, Y., & Powers, E. (1978). Digital bispectral analysis of self-excited fluctuation spectra. *The Physics of Fluids*, *21*(8), 1452–1453. 20

Kostense, J. K. (1985). Measurements of surf beat and set-down beneath wave groups. In *Coastal Engineering 1984*, (pp. 724–740). 13, 14, 57, 121, 123, 140, 141

Lamb, H. (1932). *Hydrodynamics 6th ed...* 135

Lara, J. L., Ruju, A., & Losada, I. J. (2011). Reynolds averaged navier–stokes modelling of long waves induced by a transient wave group on a beach. In *Proceedings of the Royal Society of London A: Mathematical, Physical and Engineering Sciences*, vol. 467, (pp. 1215–1242). The Royal Society. 26

Lin, C.-Y., & Huang, C.-J. (2004). Decomposition of incident and reflected higher harmonic waves using four wave gauges. *Coastal engineering*, *51*(5-6), 395–406. 57

List, J. H. (1992). A model for the generation of two-dimensional surf beat. *Journal of Geophysical Research: Oceans*, *97*(C4), 5623–5635. 2, 16, 17, 79, 100, 121, 140, 141

Liu, P. C., & Babanin, A. V. (2004). Using wavelet spectrum analysis to resolve breaking events in the wind wave time series. In *Annales Geophysicae*, vol. 22, (pp. 3335–3345). 23

Longuet-Higgins, M. S., & Stewart, R. (1960). Changes in the form of short gravity waves on long waves and tidal currents. *Journal of Fluid Mechanics*, *8*(4), 565–583. 109, 169

Longuet-Higgins, M. S., & Stewart, R. (1962). Radiation stress and mass transport in gravity waves, with application to 'surf beats'. *Journal of Fluid Mechanics*, *13*(4), 481–504. 2, 12, 13, 16, 18, 72, 100, 112, 120, 121, 122

Longuet-Higgins, M. S., & Stewart, R. (1964). Radiation stresses in water waves; a physical discussion, with applications. In *Deep Sea Research and Oceanographic Abstracts*, vol. 11, (pp. 529–562). Elsevier. 12, 100

Madsen, P. A., Sørensen, O., & Schäffer, H. (1997). Surf zone dynamics simulated by a boussinesq type model. part ii: Surf beat and swash oscillations for wave groups and irregular waves. *Coastal Engineering*, *32*(4), 289–319. 14

Masselink, G. (1995). Group bound long waves as a source of infragravity energy in the surf zone. *Continental Shelf Research*, *15*(13), 1525–1547. 16

Miche, M. (1951). Le pouvoir réfléchissant des ouvrages maritimes exposés à l'action de la houle. *Annales de Ponts et Chaussées, 121 (285-319)*. 28

Moura, T., & Baldock, T. (2017). Remote sensing of the correlation between breakpoint oscillations and infragravity waves in the surf and swash zone. *Journal of Geophysical Research: Oceans*, *122*(4), 3106–3122. xiv, 2, 27, 123

Moura, T., & Baldock, T. (2018). New evidence of breakpoint forced long waves: Laboratory, numerical and field observations. *Journal of Geophysical Research: Oceans*. 14, 15, 63, 120, 140

Munk, W. (1949). Surf beats. *EOS, Transactions American Geophysical Union*, *30*(6), 849–854. 2

Norheim, C., Herbers, T., & Elgar, S. (1998). Nonlinear evolution of surface wave spectra on a beach. *Journal of physical oceanography*, *28*(7), 1534–1551. 95

Padilla, E. M., & Alsina, J. M. (2017). Transfer and dissipation of energy during wave group propagation on a gentle beach slope. *Journal of Geophysical Research: Oceans*, *122*(8), 6773–6794. 71, 99

Padilla, E. M., & Alsina, J. M. (2018). Long Wave Generation Induced by Differences in the Wave-Group Structure. *Journal of Geophysical Research: Oceans*, *123*(12), 8921–8940. 119

Phillips, O. (1960). On the dynamics of unsteady gravity waves of finite amplitude part 1. the elementary interactions. *Journal of Fluid Mechanics*, *9*(2), 193–217. 15, 72, 120

Raubenheimer, B., Guza, R., Elgar, S., & Kobayashi, N. (1995). Swash on a gently sloping beach. *Journal of Geophysical Research: Oceans*, *100*(C5), 8751–8760. 122

Rocha, M., Michallet, H., & Silva, P. A. (2017). Improving the parameterization of wave nonlinearities–the importance of wave steepness, spectral bandwidth and beach slope. *Coastal Engineering*, *121*, 77–89. 95

Ruessink, B. (1998b). Bound and free infragravity waves in the nearshore zone under breaking and nonbreaking conditions. *Journal of Geophysical Research: Oceans*, *103*(C6), 12795–12805. 2

Ruessink, B., Kleinhans, M., & den Beukel, P. (1998a). Observations of swash under highly dissipative conditions. *Journal of Geophysical Research: Oceans*, *103*(C2), 3111–3118. 2, 25, 27, 28, 102, 120, 122, 143

Ruessink, B., Van den Berg, T., & Van Rijn, L. (2009). Modeling sediment transport beneath skewed asymmetric waves above a plane bed. *Journal of Geophysical Research: Oceans*, *114*(C11). 73

Ruessink, B., Walstra, D., & Southgate, H. (2003). Calibration and verification of a parametric wave model on barred beaches. *Coastal Engineering*, *48*(3), 139–149. 25

Ruggiero, P., Holman, R. A., & Beach, R. (2004). Wave run-up on a high-energy dissipative beach. *Journal of Geophysical Research: Oceans*, *109*(C6). 2, 28, 120, 122, 143

Schäffer, H. A. (1993). Infragravity waves induced by short-wave groups. *Journal of Fluid Mechanics*, *247*, 551–588. 14, 17, 122, 141

Schäffer, H. A. (1996). Second-order wavemaker theory for irregular waves. *Ocean Engineering*, *23*(1), 47–88. 44

Schäffer, H. A., & Jonsson, I. G. (1991). Theory versus experiments in two-dimensional surf beats. In *Coastal Engineering 1990*, (pp. 1131–1143). 17

Sénéchal, N., Bonneton, P., & Dupuis, H. (2001a). Field observations of irregular wave transformation in the surf zone. In *Coastal Dynamics' 01*, (pp. 62–71). 27, 117

Sénéchal, N., Coco, G., Bryan, K. R., & Holman, R. A. (2011). Wave runup during extreme storm conditions. *Journal of Geophysical Research: Oceans*, *116*(C7). 27, 28, 79, 102, 120, 122, 143

Sénéchal, N., Dupuis, H., Bonneton, P., Howa, H., & Pedreros, R. (2001b). Observation of irregular wave transformation in the surf zone over a gently sloping sandy beach on the french atlantic coastline. *Oceanologica Acta*, *24*(6), 545–556. 27

Spinneken, J. (2010). Wave generation and absorption using force-feedback control, phd thesis. *Imperial College London*. 44, 45

Spinneken, J., Swan, C., et al. (2011). Theoretical transfer function for force-controlled wave machines. *International Journal of Offshore and Polar Engineering*, *21*(03). 45

Stockdon, H. F., Holman, R. A., Howd, P. A., & Sallenger Jr, A. H. (2006). Empirical parameterization of setup, swash, and runup. *Coastal engineering*, *53*(7), 573–588. 28

Stokes, G. G. (1847). On the theory of oscillatory waves. *Trans. Cambridge Philos. Soc.*, *8*, 441–455. 12, 85

Svendsen, I. A. (1984). Wave heights and set-up in a surf zone. *Coastal engineering*, *8*(4), 303–329. 24

Svendsen, I. A. (2006). *Introduction to nearshore hydrodynamics*, vol. 24. World Scientific. 10, 24

Symonds, G., Huntley, D. A., & Bowen, A. J. (1982). Two-dimensional surf beat: Long wave generation by a time-varying breakpoint. *Journal of Geophysical Research: Oceans*, *87*(C1), 492–498. 2, 14, 15, 18, 101, 119, 120, 123, 143

Thomson, J., Elgar, S., Raubenheimer, B., Herbers, T., & Guza, R. (2006). Tidal modulation of infragravity waves via nonlinear energy losses in the surfzone. *Geophysical Research Letters*, *33*(5). 26, 117

Thornton, E. B., & Guza, R. (1982). Energy saturation and phase speeds measured on a natural beach. *Journal of Geophysical Research: Oceans*, *87*(C12), 9499–9508. 80

Tissier, M., Bonneton, P., Michallet, H., & Ruessink, B. (2015). Infragravity-wave modulation of short-wave celerity in the surf zone. *Journal of Geophysical Research: Oceans*, *120*(10), 6799–6814. 27, 79, 117

Tucker, M. (1950). Surf beats: sea waves of 1 to 5 min. period. In *Proc. R. Soc. Lond. A*, vol. 202, (pp. 565–573). The Royal Society. 2

Van Dongeren, A., Bakkenes, H. J., & Janssen, T. (2003). Generation of long waves by short wave groups. In *Coastal Engineering 2002: Solving Coastal Conundrums*, (pp. 1093–1105). World Scientific. 17, 121, 141

Van Dongeren, A., Battjes, J., Janssen, T., Van Noorloos, J., Steenhauer, K., Steenbergen, G., & Reniers, A. (2007). Shoaling and shoreline dissipation of low-frequency waves. *Journal of Geophysical Research: Oceans*, *112*(C2). 2, 4, 16, 17, 18, 26, 27, 28, 46, 51, 57, 58, 100, 101, 102, 112, 113, 114, 116, 117, 118, 120, 121, 122, 129, 140, 143

Van Dongeren, A. R., & Svendsen, I. A. (1997). Quasi 3-d modeling of nearshore hydrodynamics. Tech. rep., Delaware University. Newark Center for Applied Coastal Research. 100

Veeramony, J., & Svendsen, I. (1997). Wave groups in the surf-zone: Model & experiments. In *Coastal Engineering 1996*, (pp. 151–164). 77

Weggel, J. R. (1973). Maximum breaker height for design. In *Coastal Engineering 1972*, (pp. 419–432). 24

Zhang, J., Chen, L., Ye, M., & Randall, R. E. (1996). Hybrid wave model for unidirectional irregular waves – part i. theory and numerical scheme. *Applied Ocean Research*, *18*(2-3), 77–92. 169

Appendices

A

Second-order solution for the water surface elevation

The Water surface elevation for the interaction between two wave components ($f_1 > f_2$) in uniform intermediate water-depth h was derived up to the second order by Longuet-Higgins & Stewart (1960) using a conventional perturbation approach. The presented formulation follows the notation given in Zhang et al. (1996):

$$\eta^{(II)} = \eta_{f_1} + \eta_{f_2} + \eta_{2f_1} + \eta_{2f_2} + \eta_{f_1+f_2} + \eta_{f_1-f_2}, \tag{A.1}$$

where

$$\begin{aligned}
\eta_{f_1} &= a_1 \cos(\theta_1), && \text{(A.2)}\\
\eta_{f_2} &= a_2 \cos(\theta_2), && \text{(A.3)}\\
\eta_{2f_1} &= (1/4)\, a_1^2\, k_1\, \alpha_1\, (3\alpha_1^2 - 1) \cos(2\theta_1), && \text{(A.4)}\\
\eta_{2f_2} &= (1/4)\, a_2^2\, k_2\, \alpha_2\, (3\alpha_2^2 - 1) \cos(2\theta_2), && \text{(A.5)}\\
\eta_{f_1+f_2} &= B_{(+)} \cos(\theta_1 + \theta_2), && \text{(A.6)}\\
\eta_{f_1-f_2} &= B_{(-)} \cos(\theta_1 - \theta_2), && \text{(A.7)}
\end{aligned}$$

and

$$B_{(-)} = \frac{a_1 a_2\, k_1}{2\alpha_1}\left(\alpha_2\lambda_{2,1}^2 - \alpha_1\right)\frac{\alpha_1\lambda_{2,1}^2(\alpha_2^2-1) + 2\alpha_1\alpha_2\lambda_{2,1}(\alpha_1-\alpha_2) - \alpha_2(\alpha_1^2-1)}{(\alpha_1-\alpha_2\lambda_{2,1})^2 - (1-\lambda_{2,1})^2}, \tag{A.8}$$

$$B_{(+)} = -\frac{a_1 a_2\, k_1}{2\alpha_1}\left(\alpha_2\lambda_{2,1}^2 + \alpha_1\right)\frac{\alpha_1\lambda_{2,1}^2(\alpha_2^2-1) + 2\alpha_1\alpha_2\lambda_{2,1}(\alpha_1+\alpha_2) + \alpha_2(\alpha_1^2-1)}{(\alpha_1-\alpha_2\lambda_{2,1})^2 - (1+\lambda_{2,1})^2}. \tag{A.9}$$

with $\lambda_{i,j} = f_i/f_j$, $\alpha_i = \coth(k_i\, h)$ and $\theta_i = 2\pi f_i t - k_i\, x + \phi_i$. The amplitudes of the primary wave components are a_i.

B

Wave tracking using cross-correlation functions

Assuming a water surface elevation η formed of a wave train whose frequency is f, the wave tracking of a certain crest consists in determining the time instant $\tau(x_n)$ when the target wave is at x_n. This wave tracking is done over time since the temporal resolution is usually the highest. For instance, *IBIMS-ICL* data set has 3 data points per meter approximately during the shoaling region, whereas 100 data points are available per second ($f_s = 100$Hz). Therefore, a better wave tracking is performed when τ is a function of x_n.

If the target wave is the averaged wave crest forming the wave train, the use of cross-correlation functions is necessary to perform a global tracking of the wave train. The estimation of $\tau(x_n)$ is recursively computed as follows:

1. Define an initial estimation of $\Delta\tau$, which is the time necessary for the wave train to travel from x_{n-1} to x_n. This estimation is based on a theoretical approximation of the target wave celerity. For instance, if the wave train freely propagates, a celerity c based on the Dispersion Equation at the frequency f is a valid approximation. Then, the initial estimation of $\Delta\tau$ is

$$\Delta\tau^{(I)} = \frac{x_n - x_{n-1}}{c}. \tag{B.1}$$

2. Define the domain $\Omega = \Big[\Delta\tau^{(I)} - 1/(2\,f), \Delta\tau^{(I)} + 1/(2\,f)\Big]$.

3. Compute the cross-correlation function at x_n, being defined as

$$R_{V,Y}(\varepsilon) = \frac{E[V \cdot Y]}{\sigma_V \, \sigma_Y}, \tag{B.2}$$

where, $V = \eta(t, x_n)$ and $Y = \eta(t + \varepsilon, x_{n-1})$, $E[\ \cdot\ ]$ denotes the expected value and σ represents the standard deviation. ε is a time-shift variable defined within the domain Ω. The usual cross-correlation function $R_{V,Y}$ returns a value between -1 and 1, where 1 means a perfect match.

4. Compute a proper estimation of $\Delta\tau$ as $\Delta\tau^{(II)} = \varepsilon$ when $R_{V,Y}(\varepsilon)$ is maximum.

5. Finally, assuming $\tau(x_{n-1})$ known from the previous iteration, then

$$\tau(x_n) = \tau(x_{n-1}) + \Delta\tau^{(II)}. \tag{B.3}$$

Steps 1 to 5 are recursively repeated along the spatial domain until τ is computed in every location x_n. Note that this method implies $\tau(x_1) = 0$ (at the first measuring location).

This procedure allows obtaining the real propagation celerity c of any signal measured at consecutive wave gauge locations as

$$c(x_n) = \frac{x_n - x_{n-1}}{\tau(x_n) - \tau(x_{n-1})}. \tag{B.4}$$

The application of this procedure involving steps 1-5 to various combination of signals implies a different notation of the correlation function depending of the pair of signals used. For instance, $R_{ILW,ILW}$ denotes the correlation function performed between pairs of ILWs, although different features may be also correlated as Janssen et al. (2003) did. The high spatial resolution of the measurement allows a representation of the cross-correlation functions in a quasi-continuous distribution in space.